工學博士學位論文

‘Top-down’ and ‘Bottom-up’ Fabrication of Graphene Quantum Dots and Their Optoelectronic Applications

하향식/상향식 접근방법을 통한 그래핀 양자점의 제조 및 광전자 응용

2014年 8月

서울大學校 大學院

化學生物工學部

李 恩 雨

‘Top-down’ and ‘Bottom-up’ Fabrication of Graphene Quantum Dots and Their Optoelectronic Applications

하향식/상향식 접근방법을 통한 그래핀 양자점의 제조 및 광전자 응용

指導敎授: 張 正 植

이 論文을 工學博士 學位論文으로 提出함

2014年 5月

서울大學校 大學院

化學生物工學部

李 恩 雨

李 恩 雨의 工學博士 學位論文을 認准함

2014年 5月

委 員 長 _____ (인)

副委員長 _____ (인)

委 員 _____ (인)

委 員 _____ (인)

委 員 _____ (인)

‘Top-down’ and ‘Bottom-up’ Fabrication of Graphene Quantum Dots and Their Optoelectronic Applications

by

Eunwoo Lee

Submitted to the Graduate School of Seoul National University

in Partial Fulfillment of the Requirements

for the Degree of Doctor of Philosophy

August, 2014

Thesis Adviser: Jyongsik Jang

ABSTRACT

Graphene quantum dot (GQD), typically composed of graphene sheets with lateral dimensions less than 100 nm in single-, double- and few- (3 to <10) layers, has emerged tremendous research interest. Due to the pronounced quantum confinement and edge effects, GQDs assume numerous novel chemical/physical properties. Besides GQD also show low cytotoxicity, excellent solubility, chemical inertness, stable photoluminescence, better surface grafting, thus making them promising in optoelectonic devices, sensors, bioimaging, *etc*. Up to date, various synthetic methods for preparing GQD have been developed. However, most previous synthetic methods suffer from the precise control of the size, shape, fluorescence wavelength, and heteroatom doping. Consequently, it is still challenging to produce graphene with tailored morphology and diameters for various applications.

This dissertation describes the two different ways in the synthetic methodology of graphene will be presented in the viewpoint of top-down approach and bottom-up approach. As a ‘top-down approach’, the GQDs with well-defined and low size distribution fabricated using a simple oxidation of

carbon nanomaterials and size-selective precipitation. Interestingly, the diameter and luminescence wavelength of graphene quantum dots can be controlled by selectively designing the morphology of starting materials and optimizing the oxidation condition. As a 'bottom-up approach', heteroatoms-doped GQDs are formed using simple carbonization approach of organic precursor with two different doping sources. Under the catalytic reaction conditions of H_2SO_4, citric acid can be transformed to GQD due to the dehydration forming a graphitic hexagonal matrix. This novel strategy does not require a high carbonization temperature and pressure, and the simple strategy offers great possibility for fabricating heteroatom(S or N)-doped GQDs with precise control of carbonization degree, a gram-scale production, and high-PLQY (*ca.* 61%). Most, importantly, these novel approaches can be used as an alternative tool for fabrication of various carbon-based nanomaterials with rational nanostructure design and may offer an opportunity for the further investigation of industrial applications, and might be expanded to allow the applications of GQDs in a wide range of areas (*e.g.*, electronic/optoelectronic devices, fluorescent probe, bioimaging system, energy conversion systems).

KEYWORDS: Carbon nanomaterials; Graphene quantum dot; Synthetic methodology; Top-down; Bottom-up; DSSC; fluorescence sensor.

STUDENT NUMBER: 2009–23955

List of Abbreviations

AFM : atomic force microscope

B-GQD : boronate-modified graphene quantum dot

CN : carbon nanomaterials

CNF : carbon nanofiber

CV : cyclic voltammetery

d : particle diameter

DAPI : 4'-6-Diamidino-2-phenylindole

DFT : density functional theory

DLS : dynamic light scattering spectroscopy

DPA :dipicolinic acid

DSSC : dye-sensitized solar cell

EDC : ethylene dichloride

EDTA : ethylenediamine tetraacetic acid

FA : folic acid

FE-SEM : field emission scanning electron microscopy

FF : fill factor

F-GQD : folic acid-modified graphene quantum dot

FLQY : fluorescence quantum yield

FRET : fluorescence resonance energy transfer

FT-IR : fourier transform infrared

G : gravitational acceleration

GNR : graphene nanoribbon

GO : graphene oxide

GQD : graphene quantum dot

GS : graphene sheet

H-CNF : herringbone-typed carbon nanofiber

HEPES : 4-(2-Hydroxyethyl)piperazine-1-ethanesulfonic acid

H-GQD : H_2O_2-treated boronate-modified GQD

HR-TEM : high-resolution transmission electron microscope

IPCE : incident photon-to-current efficiency

Isc : short-circuit current

J-V : current–voltage

K_{obs} : rate constant

LOD : limit of detection

MCF-7 : a type of breast cancer cell which has overexpressed folate receptor

MWCNT : multiwalled carbon nanotube

NHS : N-Hydroxysuccinimide

OPV : organic photovoltaic

PBS : phosphate buffer saline

PCE : power conversion efficiency

P-CNF : platelet-typed carbon nanofiber

PEG : polyethylene glycol

PET : photoinduced electron transfer

P-GQD : pristine graphene quantum dot

PL : photoluminescence

PMA : phorbol-12-myristate-13-acetate

QY : quantum yield

ROS : reactive oxygen species

SK-BR-3 : a type of breast cancer cell which absent folate receptor

TBA : tetrabutylammonium

UV-vis : ultraviolet-visible

V_g : sedimentation velocity

Voc : open-circuit voltage

XPS : X-ray photoelectron spectroscopy

η : viscosity of liquid

ρ_1 : liquid density

ρ_p : particle density

List of Figures

hydroxylated carbon nanoparticles gives rise to the fluorescent carbon nanoparticles. Oxidative cleavage of the expanded graphite produces graphene nanoribbons.

Figure 4. Synthesis of graphene quantum dots *via* bottom-up approach.

Figure 5. Fluorescent images of human breast cancer cell T47D after incubation with green GQDs for 4 h. (a) Phase contrast picture of T47D cells. (b) Individual nucleus stained blue with DAPI. (c) Agglomerated green GQDs surrounding each nucleus. (d) The overlay high contrast image of nucleolus stained with blue DAPI and GQDs (green) staining

Figure 6. (1) Relationship between MB concentration and reaction time for different catalysts: rutile TiO_2/GQDs, $CaLn_2O_4$, antatse TiO_2/GQDs, GQDs, rutile TiO_2 NPs, and anatase TiO_2 NPs. (b) Schematic of photocatalytic process for rutile TiO_2/GQD and anatase TiO_2/GQD under visible light irradiation.

Figure 7. (a) Schematic and (b) energy band diagrams of the ITO/ PEDOT:PSS/P3HT:GQDs/Al device. (c) *J–V* characteristic curves

(black line), NH_2-GQDs (red line), and Eu-GQDs (blue line). (b) Curve fit of the C 1s peak of GQD. (c) Curve fit of the C 1s peak of NH_2-GQD. (d) Curve fit of the C 1s peak of Eu-GQD.

Figure 47. (a) Representative fluorescence spectra of 3-nm Eu-GQDs (black line) and 10-nm Eu-GQDs (red line) excited at 350 nm (red line). (b) Time-dependent fluorescence intensity plot of 3-nm Eu-GQDs (black line) and 10-nm Eu-GQDs (red line) following exposure to DPA (250 nM; fluorescence detected at 616 nm).

Figure 48. (a) Fluorescence spectra of 3-nm Eu-GQDs for various concentrations of DPA. (b) Fluorescence intensity of 3-nm Eu-GQDs at 616 nm as a function of the DPA concentration. The adjusted coefficient of determination was $R^2 = 0.996$ for the 3-nm Eu-GQDs. (inset: photo of 3-nm Eu-GQD and 3-nm Eu-GQD in the presence of 1 μM DPA under 364 nm UV irradiation)

Figure 49. (a) Fluorescence spectra of 10-nm Eu-GQDs for various concentrations of DPA. (b) Fluorescence intensity of 10-nm Eu-GQDs at 616 nm as a function of the DPA concentration. The

Figure 60. (a) Live cell differential interference images of the cells and (b) their relative fluorescence intensity. Both cells were treated with 10 μg mL^{-1} of B-GQD for 24 h, and 5 μg mL^{-1} PMA was additionally inserted for intracellular H_2O_2 generation (scale bar: 90 μm).

Figure 61. Viability of MCF-7 cells incubated with F-GQD (solid squares) and B-GQD (open circles) for 24 h. ROS production by MCF-7 cells after being incubated with F-GQD (shaded bars) and B-GQD (open bars). H_2O_2 (0.02%) was used as a positive control.

List of Tables

Table of Contents

1. INTRODUCTION

1.1. Background

1.1.1. Graphene quantum dots

Carbon, one of the most abundant elements on the earth, brings us star materials over and over again.[1, 2] Graphitic forms include 0D fullerene, 1D CNT and 3D graphite, and the 2D case comes to the graphene, a single layer of carbon atoms formed in honeycomb lattice.[3] Recently, graphene, a novel one-atom-thick two-dimensional graphitic carbon system, has attracted enormous attention because of its unique physical properties and with numerous promising applications in nanotechnology ever since discocered in 2004 by Geim and Novoselov *et al*.[4-6] As graphene is a zeo-bandgap material, the possibility for the observation of its application in electronic and opto-electronic application has been limited.[7] Accordingly, techniques to engineer the bandgap in graphene have attracted significant attention for applications in graphene-based opto-electronics.[8, 9] Up to date, diverse strategies for the formation of a bandgap in graphene structures have been developed using quantum confinement and edge effects such as graphene nanoribbons (GNRs) and graphene quantum dots (GQDs) (Figure 1).[2, 10] Among graphene nanostructures, GQDs, typically composed of graphene sheets with lateral dimensions less than 100 nm in single-, double- and few- (3

to <10) layers, have recently emerged as a potential candidate for fluorescent probes in bioimaging and semiconductor materials in electronic devices due to their numerous novel chemical/physical properties.[11] Besides GQD also show low cytotoxicity, excellent solubility, chemical inertness, stable photoluminescence, better surface grafting, thus making them promising in optoelectonic devices, sensors, bioimaging, *etc*.[12-17] Typically, GQDs contain carboxylic acid moieties at the edge, which is similar to graphene, thus imparting them with excellent water solubility and suitability for subsequent functionalization with various organic, polymeric, inorganic or biological species.[18, 19] Interestingly, GQDs also possess fascinating upconversion photoluminescence (PL) properties, making them a valuable platform for photoelectrochemical cells.[20, 21] As a consequence of their simple structure, as well as health concerns and biological hazards of semiconductor based QDs, GQDs are at the center of significant research efforts to develop low-toxicity, eco-friendly alternatives that have the desirable performance characteristics of QDs.[22, 23]

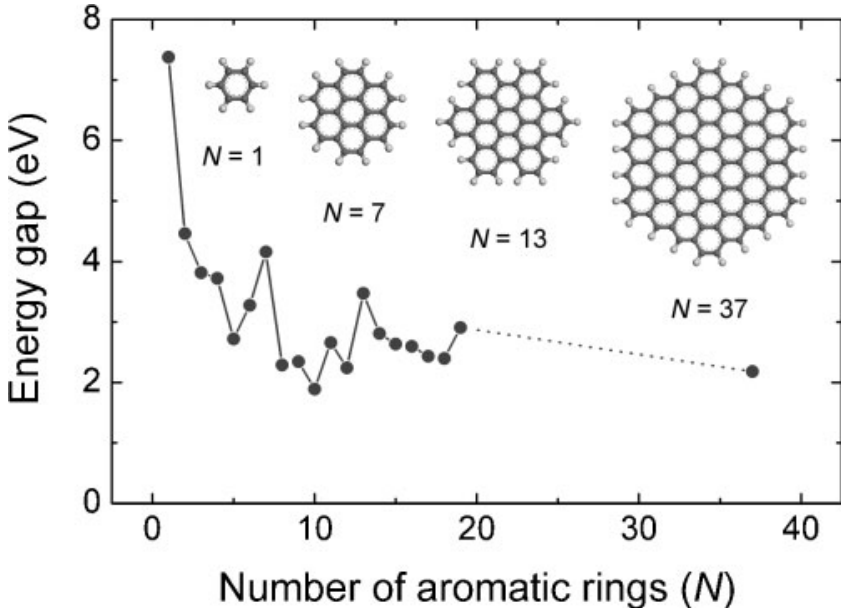

Figure 1. Energy gap of $\pi - \pi^*$ transitions calculated based on DFT as a function of the number of fused aromatic rings (N). The inset shows the structures of the graphene molecules used for calculation. Reprinted with permission from Ref. 14. Copyright 2010 Right Managed by Wiley-VCH Verlag GmbH & Co. KGaA.

1.1.2. Synthesis of graphene quantum dots

Up till now, tremendous efforts have been made to develop synthetic methods for GQDs, which can be classified into two main groups: top-down and bottom-up methods.[18, 19] The top-down methods include electron beam lithography, acidic exfoliation, electrochemical oxidation, microwave-assisted hydrothermal synthesis, and so on.[10, 13] In addition, GQDs can also be prepared through bottom-up routes, including the solution chemistry, cyclodehydrogenation of polyphenylene precursors, carbonizing some special organic precursorsor, the fragmentation of suitable precursors, for example, the C60.[11, 15, 16, 24-26] The top-down routes for the preparation of GQDs have the advantages of abundant raw materials, large scale production and simple operation.[27] Moreover, the GQDs synthesized *via* top-down methods usually contain oxygen-containing functional groups at the edge, thus facilitating their solubility, functionalization and passivation.[28] However, this method also suffers from some disadvantages, such as the requirement of special equipment, low yield, the damage on the aromatic carbon framework, and the non-selective “top-down” chemical cutting process, which does not allow precise control over the morphology and the size distribution of the products.[29] Conversely, the bottom-up methods offers us exciting opportunities to control the GQDs with well-defined molecular size, shape, and thus properties.[30] Nevertheless, these methods always involve complex synthetic procedures, and

the special organic precursors may be difficult to obtain.[31] More importantly, the poor solubility and strong tendency of aggregation of the GQDs limits their practical applications.[32] Besides, these GQDs obtained *via* the solution chemistry are usually smaller than 5 nm, which is below the processable scale of state-of-the-art lithography technology (10 nm).[33] In the past few years, increasing efforts have been paid to the advanced synthesis of GQDs, and the deficiencies have gradually overcome *via* the elaborate designs.[34]

1.1.2.1. Acidic oxidation

The acidic oxidation method has emerged to be one of the most promising techniques for the large-scale production of single and multiple layer graphene quantum dots.[35, 36] Li *et al.* suggested that a well-controlled oxidation induced cut of graphene could lead to more smooth edges compared to heat or sonic treatment.[37] Thus the oxidation of GO in a strong acid solution is a widely adopted method, usually followed by neutralization of the excess acid and a dialysis process.[38] Peng and co-workers reported the synthesis of GQDs in large scale with acidic exfoliation and etching of pitch carbon nanofibers (CNF) (Figure 2).[39] The carbon nanofibers were dispersed into a mixture of concentrated H_2SO_4 and HNO_3, sonicated for two hours and stirred for 24 hours at three different temperatures (80 °C, 100 °C and 120 °C).

Accordingly, three kinds of GQDs with the emission color of blue, green, and yellow were obtained, their corresponding diameters distributed between the range of 1–4 nm, 4–8 nm, and 7–11 nm, respectively. The heights of the GQDs are between 0.4 and 2 nm, corresponding to 1–3 graphene layers. A clear blue-shift from 330 to 270 nm with increasing the temperature was observed in the UV-visible absorption spectra, revealing that the reaction temperature could tune the size of the as-prepared GQDs and affect their absorption properties.[40]

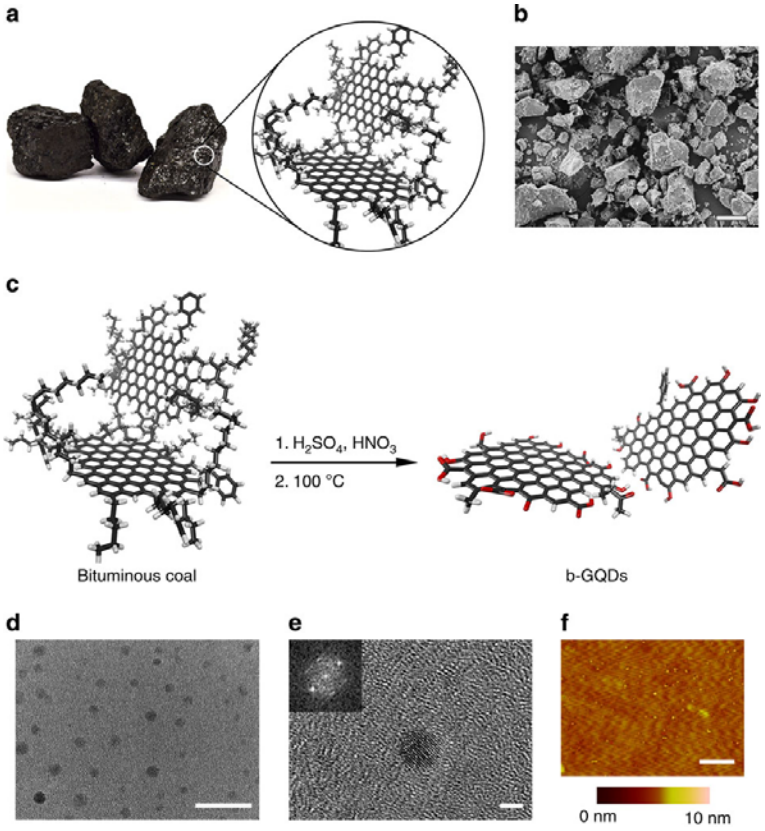

Figure 2. (a) Macroscale image and simplified illustrative nanostructure of coal. (b) SEM image of ground bituminous coal with sizes ranging from 1 to hundreds of microns in diameter. Scale bar, 50 mm. (c) Schematic illustration of the synthesis of GQDs. Oxygenated sites are shown in red. (d) TEM image of GQDs showing a regular size and shape distribution. Scale bar, 20 nm. (e) HRTEM image of representative GQDs from d; the inset is the 2D FFT image that shows the crystalline hexagonal structure of these quantum dots. Scale bar, 2 nm. (f) AFM image of GQDs showing height of 1.5–3 nm. Scale bar, 100 nm. Reprinted with permission from Ref. 35. Copyright 2013 Right Managed by Nature Publishing Group.

1.1.2.2. Hydrothermal and solvothermal method

The hydrothermal method is a facile synthetic route for the preparation of GQDs.[41, 42] It usually required the usage of strong alkali (such as NaOH and ammonia) as scissors to cut the carbon based precursors into colloid GQDs.[43] In 2010, Pan *et al*. firstly reported the hydrothermal synthesis of GQDs using micrometer-sized GO sheets as the starting material.[44] Briefly, the preparation of GQDs involved the thermal reduction of monolayer GO sheets (200–300 °C for 2 h) into chemically derived graphene sheets (GSs), the oxidization of the GSs in concentrated H_2SO_4 and HNO_3 solution for 15–20 h under mild ultrasonication, and the hydrothermal deoxidation of the oxidized GSs (200 °C for 10 h) under weakly alkaline conditions (pH 8). Their diameters are ainly distributed in the range of 5–13 nm (9.6 nm average diameter), and the topographic heights are mostly between 1 and 2 nm (1–3 graphene layers). Here, due to the low temperature for thermal de-oxidization of GO sheets and the weakly alkaline condition for the hydrothermal cutting reaction, the resultant GQDs were less ordered.[45] Later in 2011, Pan *et al.* improved this hydrothermal approach to prepare well-crystallized GQDs using high-temperature (600 °C) thermally reduced GO sheets as the precursor by a fine chemical cutting route under strongly alkaline hydrothermal conditions (pH > 12).[46] The well-crystallized GQDs exhibited strong green fluorescence

with lateral size ranging from 1.5 to 5 nm (3 nm average diameter) and a narrow height distribution from 1.5 to 1.9 nm, indicating that the GQDs typically consist of 2–3 graphene layers.

1.1.2.3. Microwave- and sonication-assisted method

A microwave-assisted technique has been widely applied to materials synthesis for it combines both the advantages of hydrothermal and microwave techniques.[47] As a convenient and rapid heating source, microwave assisted exfoliation and reduction of GO has been reported.[48] Reduced graphite oxide materials could be readily obtained in the scale of minutes and the yield of graphene prepared by this method was very high, which suggested that microwave irradiation could shorten the reaction time and improve the product yield. Recently, Li *et al*. developed a facile microwave-assisted approach for the preparation of stabilizer-free two-color GQDs from GO nanosheets under acid conditions.[49] Briefly, initiated by the acid oxidation of epoxy groups, it was prone to form a mixed line on the carbon lattice composed of fewer epoxy groups and more carbonyl groups, making the graphitic domains fragile and readily attacked. The greenish yellow-luminescent GQDs showed an average diameter of 4.5 nm, and were mostly single layered or bilayered. Followed by a single step of moderately reducing greenish yellow-luminescent GQDs with $NaBH_4$, the blue-luminescent GQDs were obtained with almost the same

dimension and height. The PL QYs of greenish yellow-luminescent- and blue-luminescent-GQDs were as high as 11.7% and 22.9%, respectively. It was also verified that reduction occurred simultaneously with the cleaving of GO, thus microwave irradiation integrated the cleaving and reduction steps into facile one step and finally simplified the synthetic process and shortened the reaction time.

1.1.2.4. Electrochemical method

Typically, carbon based materials such as graphite and MWCNTs have been widely used as the working electrode for the electrochemical preparation of CDs, as well as fluorescent graphene nanoribbons (Figure 3).[50] These methods adopted high redox potential, ranging from ±1.5 V to ±3 V, which was high enough to either oxidize the C–C bonds or oxidize water to generate hydroxyl and oxygen radicals playing the role of an electrochemical "scissors" in its oxidative cleavage reaction.[15] Besides, the potential cycling can drive the supporting electrolyte (BF_4^- or TBA^+ ions) to intercalate into the carbon anode, thus bring about the depolarization and expansion of the carbon anode. Both the interplay of anodic oxidation and anion intercalation lead to the exfoliation of the carbon anode and the production of CDs *via* defect-mediated fragmentation processes. This electrochemical strategy has further been

extended to the production of GQDs.[51] The electrochemical preparation of GQDs was firstly performed by Li *et al.* in 0.1 M phosphate buffer solution (PBS, pH 6.86) with a filtration-formed graphene film as the working electrode upon the application of cyclic voltammetry (CV) scan within the potential region of ±3 V.[52] The collected GQDs were monodisperse with a uniform diameter of ca. 3–5 nm, the topographic heights were between 1 and 2 nm, indicating the architecture of 1–3 graphene layers. The GQDs present a green luminescence and can be retained stably in water for several months without any changes.

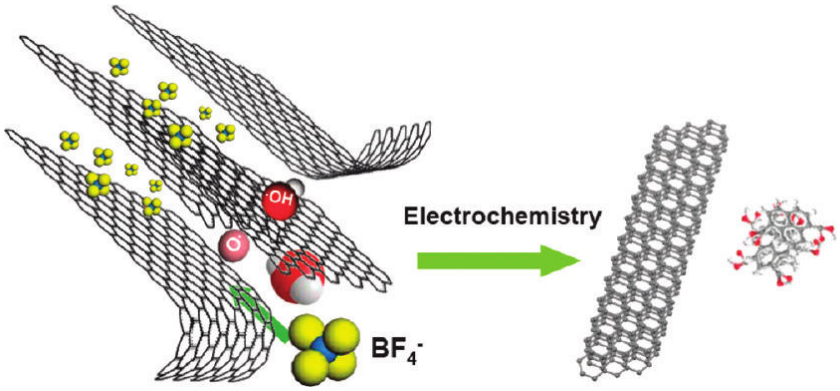

Figure 3. Illustration of the exfoliation process showing the attack of the graphite edge planes by hydroxyl and oxygen radicals, which facilitate the intercalation of BF_4 anion. The dissolution of hydroxylated carbon nanoparticles gives rise to the fluorescent carbon nanoparticles. Oxidative cleavage of the expanded graphite produces graphene nanoribbons. Reprinted with permission from Ref. 50. Copyright 2009 Right Managed by American Chemical Society.

1.1.2.5. Bottom-up approach

Compared with the top-down routes, the reports concerning the bottom-up routes are relatively scarce. Li's group has made great effort to synthesize GQDs *via* stepwise solution chemistry based on oxidative condensation reactions.[53] The obtained large colloidal GQDs have a uniform and tunable size, containing conjugated carbon atoms respectively. The stabilization of the resultant GQDs was achieved by multiple 2',4',6'-triakyl phenyl groups covalently attached to the edges of the graphene moieties. (Figure 4) The crowdeness on the edges of the GQDs twists the substituted phenyl groups from the plane of the core, leading to alkyl chains closing the latter in all three dimensions. This results in reduced face-to-face interaction between the graphenes, thus effectively increasing their solubility. Some organic precursors have also shown great potential for the preparation of GQDs *via* pyrolysis or carbonization under certain conditions. Tang *et al.* firstly reported a facile microwave-assisted hydrothermal method for the production of GQDs with glucose as the starting material and also the sole reagent.[53] First the glucose molecules were dehydrated to form the nucleus of GQDs that is composed of C═C. Then the growth of GQD occurred at the spherical surface (edge growth), with increasing heating time. The source molecules reach the surface of the GQD and generate new C═C by dehydration. Owing to the high pressure induced by the hydrothermal condition, the freshly formed C═C is orderly

arranged and assists the growth of crystalline GQDs. The diameter of the GQDs can be increased by increasing microwave heating time. The size of the GQDs can be tuned from 1.65 to 21 nm by simply prolonging the heating time from 1 to 9 min. at the same time. They also claimed that most of the carbohydrates which contain C, H, and O in the ratio of ~1 : 2 : 1 may be used as the carbon source to prepare GQDs.

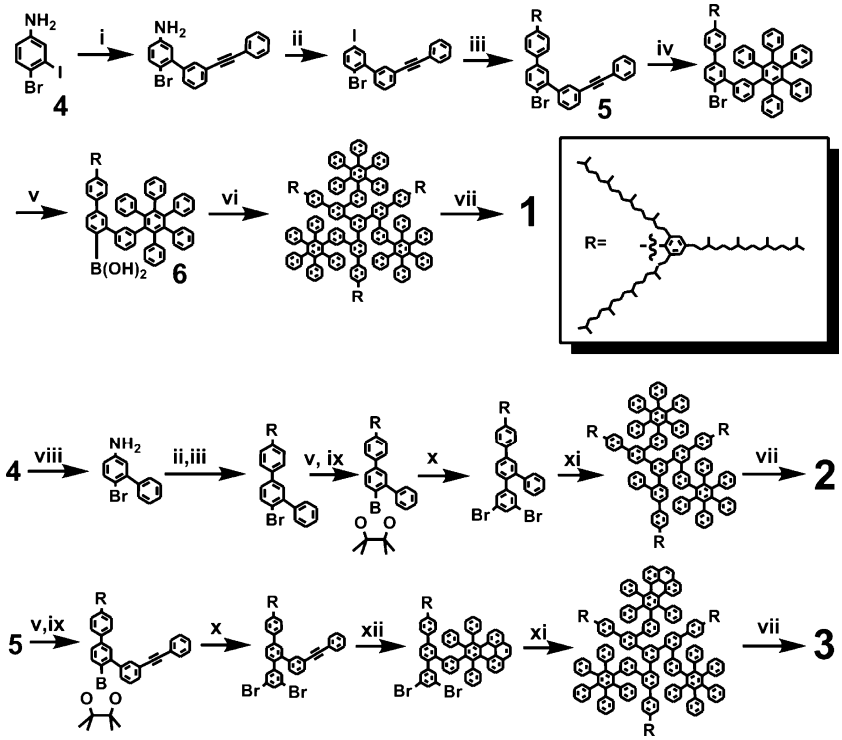

Figure 4. Synthesis of graphene quantum dots *via* bottom-up approach. Reprinted with permission from Ref. 53. Copyright 2010 Right Managed by American Chemical Society.

1.1.3. Application fields

With its superior properties, such as fluorescence, physiological stability, pH sensitivity, up-conversion PL property, fine biocompatibility and low toxicity, GQD has offered substantial application perspectives.[25, 54, 55] Meanwhile, rapid development in synthesizing GQD with controllable sizes, tailorable chemical structures, as well as strong PL, further speeds up their applications.[19] Until now much effort has been centered on biological and other applications

1.1.3.1. Bioimaging

Optical properties are the key for GQDs to be put into practical use.[56, 57] The bright PL and established low cytotoxicity render GQDs applicable in biological applications such as bioimaging.[18] Peng *et al*. selected the green luminescent GQDs to incubate with human breast cancer cell lines T47D with the nucleus stained with DAPI (blue color).[58] Figure 5 showed the images of T47D cells treated with green GQDs for 4 h incubation time, which clearly visualized the phase contrast image of T47D cells with nucleus stained with blue DAPI, agglomerated high contrast fluorescent image of green GQDs around each nucleus and overlay image of cell with phase contrast, DAPI and green GQDs.[59] These obtained images indicated that GQDs can be used in high contrast bioimaging.[60] The excitation-dependent PL behavior of the GQDs can give rise to numerous visible results.[61]

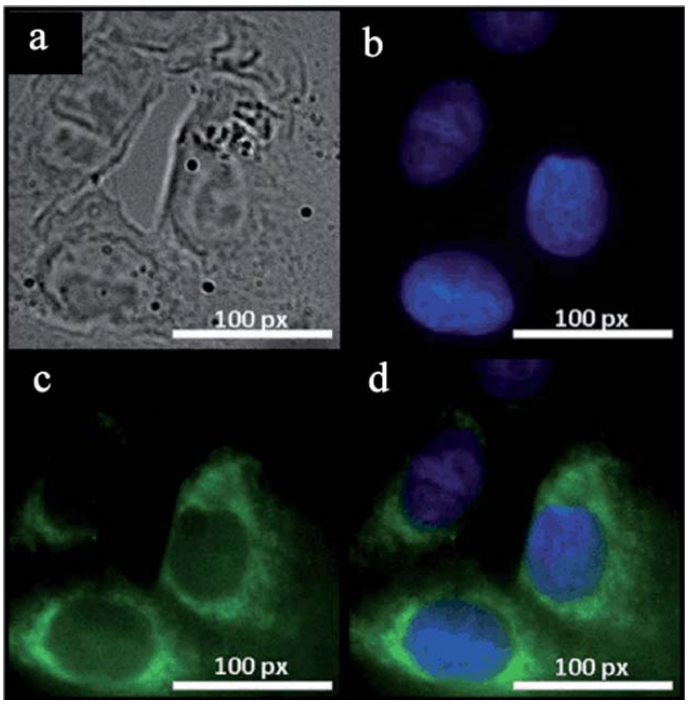

Figure 5. Fluorescent images of human breast cancer cell T47D after incubation with green GQDs for 4 h. (a) Phase contrast picture of T47D cells. (b) Individual nucleus stained blue with DAPI. (c) Agglomerated green GQDs surrounding each nucleus. (d) The overlay high contrast image of nucleolus stained with blue DAPI and GQDs (green) staining. Reprinted with permission from Ref. 58. Copyright 2012 Right Managed by American Chemical Society.

1.1.3.2. Photoluminescence sensors

Based on the PL of GQDs, various sensors have been fabricated recently with either signal-off or signal-on processes.[62] Wang *et al.* firstly reported that GQDs could be used for Fe^{3+} detection on the basis of the selective fluorescence quenching effect to Fe^{3+}.[63, 64] Taking into account the special coordinate interaction between Fe^{3+} ions and phenolic hydroxyl group which was responsible for the PL of GQDs, the photoluminescence of GQDs could be greatly affected by Fe^{3+} ions.[65] The fluorescence change GQDs with and without addition of 80 ppm Fe^{3+} ions shows that the fluorescence of GQDs in the presence of Fe^{3+} ions was almost completely quenched, while other metal ions (Zn^{2+}, Cd^{2+}, Ca^{2+}, Mg^{2+}, Pb^{2+}, Fe^{2+}, Cu^{2+}, $Ru^{3+}$and Fe^{3+}) at the same concentration had much weaker influence on the fluorescence of GQDs. In the range of 0.8–8 ppm of Fe^{3+} ions, fluorescent quenching value was detectable and presented an almost linear relationship. The detection limit of Fe^{3+} ions for 0.12 mg mL^{-1} GQDs dispersion was calculated to be around 1 ppm.

1.1.3.3. Catalyst for the oxygen reduction reaction

Zhuo *et al.* designed photocatalysts (rutile TiO_2/GQD and anatase TiO_2/GQD complex systems) to harness the visible spectrum of sunlight, based on the upconversion luminescence properties of GQDs.[66, 67] Their photocatalytic ability was determined by degradation of methylene blue (MB)

under Xe lamp irradiation (with 420 nm cutoff filter). The photodegradation efficiency is up to 97% in 60 min with the rutile TiO_2/GQD complex and 31% with anatase TiO_2/GQD complex acting as photocatalysts (Figure 6). Under visible light ($\lambda > 420$ nm) irradiation, the upconverted PL peak of GQDs was located at *ca*. 407 nm (3.05 eV). This energy was larger than the band gap of rutile TiO_2 3.0 eV (414 nm), yet smaller than that of anatase TiO_2 3.2 eV (388 nm). Hence the photocatalytic ability of rutile TiO_2/GQD was much superior to that of the anatase TiO_2/GQD complex. Contrast experiments were carried out using only pure rutile TiO_2 (50 mg), pure anatase TiO_2 (50 mg), pure GQDs (5 mL) and $CaIn_2O_4$ as photocatalysts. The result indicated that the excellent photocatalytic activities of TiO_2/GQD should be attributed to the interaction between GQDs and TiO_2.[68]

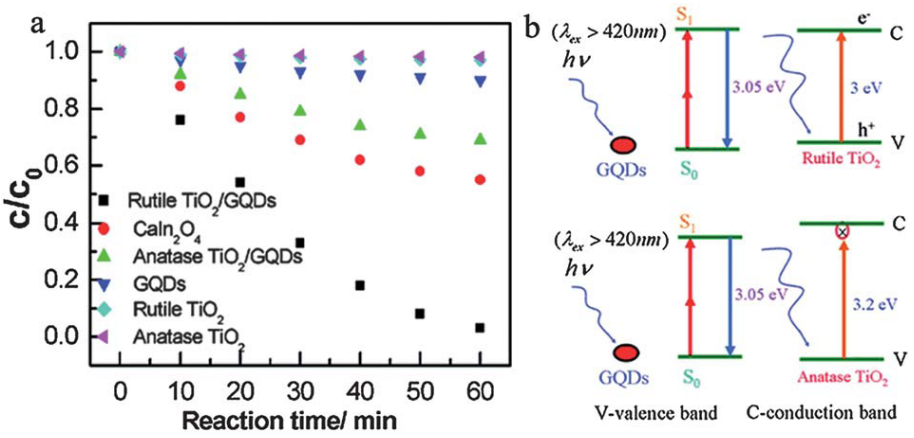

Figure 6. (1) Relationship between MB concentration and reaction time for different catalysts: rutile TiO_2/GQDs, $CaLn_2O_4$, antatse TiO_2/GQDs, GQDs, rutile TiO_2 NPs, and anatase TiO_2 NPs. (b) Schematic of photocatalytic process for rutile TiO_2/GQD and anatase TiO_2/GQD under visible light irradiation. Reprinted with permission from Ref. 66. Copyright 2012 Right Managed by American Chemical Society.

1.1.3.4. Organic photovoltaic devices

Organic photovoltaic (OPV) devices have attracted increasing attention since the report of two-layer organic photovoltaic cell by Tang.[69, 70] Usually, the OPV cells are those with bulk heterojunction (BHJ) architecture based on soluble poly(3-hexylthiophene) (P3HT) and poly(3-octylthiophene) (P3OT) as the donor and PCBM as the acceptor.[71] Recently, graphene was applied as the acceptor and could also replace the common ITO as the transparent electrode due to its remarkable electronic and mechanical properties.[71] However, graphene sheets have extremely poor solubility and have a strong tendency to aggregate into graphite.[72] The properties of large solubility and tunable band gap make GQDs very attractive for photovoltaic applications.[73]

Li *et al.* applied GQDs as novel electron acceptor in a P3HTbased solar cell.[52] As shown schematically in Figure 7, polymer photovoltaic cells with the structure of ITO/PEDOT:PSS/P3HT:GQDs/Al were fabricated, where ITO, PEDOT, PSS and P3HT stranded for indium tin oxide, poly(3,4-ethylenedioxythiophene), poly(styrenesulfonate) and poly(3-hexylthiophene), respectively. Figure 7b gives the energy level diagram for the GQD-based photovoltaic cells where the LUMO level of GQDs is estimated to be in the range of 4.2–4.4 eV by electrochemical methods. Compared with the P3HT device, the performance of GQD-based devices, in terms of such quantities as I_{sc}, V_{oc}, *FF* and *PCE*, was enhanced overall due to the contribution of GQDs in

this device (Figure 7c). In the P3HT:GQDs composite device, the GQDs provides a large surface area for the formation of p–n interfaces and carrier transporting pathways. Although without device optimization in this primary study, a power conversion efficiency of 1.28% was achieved.

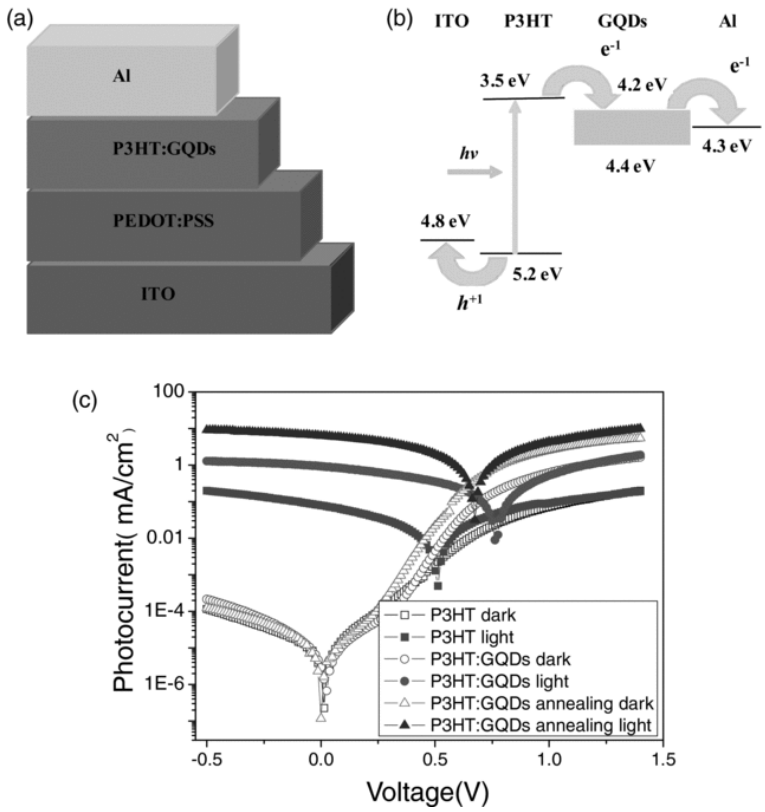

Figure 7. Schematic (a) and energy band (b) diagrams of the ITO/PEDOT: PSS/P3HT:GQDs/Al device. (c) *J–V* characteristic curves for the ITO/ PEDOT:PSS/P3HT/Al, ITO/PEDOT:PSS/P3HT:GQDs/Al and ITO/ PEDOT:PSS/P3HT:GQDs/Al devices after annealing at 140 °C for 10 min. Reprinted with permission from Ref. 52. Copyright 2010 Right Managed by Wiley-VCH Verlag GmbH & Co. KGaA.

1.2. Objectives and Outline of the Study

1.2.1. Objectives

In the preceding section, the importance of graphene quantum dots was introduced from the viewpoint of academic research and practical applications. The aim of this dissertation is to present two different synthetic methodologies to fabricate graphene quantum dots in the viewpoint of 'top-down' and 'bottom-up' approach. Furthermore, the formation mechanism of the graphene quantum dots is systematically investigated, and their application fields are also explored, including FRET-based photovoltaic devices, fluorescent sensor, and bioimaging.

1.2.2. Outline

This dissertation involves the following subtopics:

I. 'Top-down' Approach for Fabricating Uniform Graphene Quantum Dots with Sizes
   1. Chemical oxidation of various carbon nanomaterials
   2. Separation of graphene quantum dots *via* size-selective precipitation approach

II. 'Bottom-up' Approach for Fabricating Graphene Quantum Dots based on Carbonization and Heteroatom Doping

1. Carbonization of citric acid
2. Controllable S, N-doping of graphene quantum dot

III. Applications

1. FRET-based dye-sensitized solar cells for near-infrared light harvesting
2. Graphene quantum dot-based fluorescent sensor for rapid and ultrasensitive detection of an anthrax biomarker
3. Photoinduced electron transfer based sensor probes for intracellular hydrogen peroxide

A detailed outline of the study is as follows:

1. As a ‘top-down approach’, the GQDs with well-defined and low size distribution are successfully fabricated using a simple oxidation of carbon nanomaterials and size-selective precipitation. To control the size and luminesecence wavelength of graphene quantum dots, different types of CNs and various oxidation conditions are studied. Interestingly, the diameter and luminescence wavelength of graphene quantum dots can be controlled by selectively designing the morphology of starting materials and optimizing the oxidation condition. In addition, a size-selective precipitation method for GQDs is also propsed in order to separate highly monodispersed GQDs from additives or unreacted residual materials. The

GQDs can be formed without any additional time-consuming dialysis process and are highly dispersed in different solvents with high content of GQDs.

2. As a ‘bottom-up approach’, heteroatoms-doped GQDs are formed using simple carbonization approach of organic precursor with two different doping sources. Under the catalytic reaction conditions of H_2SO_4, citric acid can be transformed to GQD due to the dehydration forming a graphitic hexagonal matrix. Sulfuric acid served to S atom dopants as well as catalyst of dyhydration reaction of citric acid. Then, DMF was added when S-doped GQD was formed. DMF served as a quenching solvent for the growth retardation to GO and source of nitrogen. This novel strategy does not require a high carbonization temperature and pressure, and the simple strategy offers great possibility for fabricating heteroatom(S or N)-doped GQDs with precise control of carbonization degree, a gram-scale production, and high-PLQY (*ca.* 61%).
3. The high FLQY-GQDs could be used as light-harvesting antennae in FRET-based photovoltaic devices. This novel and simple approach involves simultaneously utilize the wide solar spectrum, thereby resulting in high conversion efficiency over a wide wavelength range. In addition, major parameters that affect the FRET interaction between donor and

acceptor have been investigated including the fluorescent emission spectrum of GQD and the content of deposited GQDs into the TiO_2 matrix. Interestingly, the Upconversion properties of GQD were determined and the response mechanism of the upconversion GQD-layer-modified working electrode in dye-sensitized solar cells (DSSCs) was investigated.

4. As a fluoresence sensor for detecting of *B. anthracis* spores, a simple and novel approach based on the hybridization of GQDs into a europium (Eu)-macromolecule complex have been proposed. This novel approach involves anchoring Eu onto GQDs of two different diameters, which provides a change in the fluorescence intensity that varies with the concentration of *B. anthracis*. Most importantly, the Eu-modified GQDs reported here exhibit an excellent limit of detection (LOD) of 10 pM towards *B. anthracis*; this concentration is six orders of magnitude smaller than the infectious dose of the spores (60 μM). We also demonstrate excellent specificity towards the *B. anthracis* spores *via* measurements of sensitivity in aqueous solutions containing numerous aromatic ligands.
5. As a selective H_2O_2 probe, a boronate and folic acid dual-modified fluorescent GQD was successfully fabricated. Well-defined GQDs were fabricated and then further surface modified with boronate and folic acid for detecting of H_2O_2 and targeting of cancer cell, respectively.

Interestingly, the fluorescence intensity changed and an emission peak shifted when BPAN nanoparticles selectively interacted with H_2O_2, relative to other ROS. The BPAN nanoparticles undergo photoinduced electron transfer (PET) between a Schiff base moiety and boronate, which enhances the fluorescence and makes the nanoparticles suitable for selective molecular recognition. In addition, we demonstrate the use of these nanoparticles as a detector of endogenous H_2O_2 produced in living cells.

2. EXPERIMENTAL DETAILS

2.1. 'Top-down' Approach for Fabricating Uniform Graphene Quantum Dots of Various Size

2.1.1. Chemical oxidation of various types of carbon materials

0.3 g of carbon nanomaterials (CNs), such as graphene oxide (GO), herringbone-typed carbon nanofiber (H-CNF), and platelet-typed carbon nanofiber (P-CNF), were added into a mixture of concentrated H_2SO_4 (60 mL) and HNO_3 (20 mL). The solution was sonicated for two hours until the solution was homogenious and then transferred into a three-neck round flask of 250 mL. The CN-contained acidic solution was oxidized under excessive acidic conditions for 24 hours at different temperatures ranging from 80 to 120 °C to synthesize GQDs. The mixture was cooled and diluted with deionized (DI) water (800 mL). Then, the pH of the GQD solution was adjusted to 8 using Na_2CO_3.

2.1.2. Separation of graphene quantum dots *via* size-selective precipitation approach

In order to isolate the graphene quantum dots, the size-selective precipitation has been carried out from the reaction mixture. At first, the crude solution of GQDs has been concentrated to approximately one fifth of the

initial volume. After that, a nonsolvent (ethanol) has been added to the concentrated solution in volume ratio of 2:1. Then, the Na_2SO_4 salts and large sized graphenes started to precipitate. From the resulting turbid solution, the precipitate and the supernatant were separated by centrifugation at 12,000 RPM for 1hr. To the first supernatant obtained from this procedure, ethanol was added into the GQD aqueous solution in volume ratio of 2:1 and a centrifugation was performed with 12,000 RPM for 1 hr, producing another fraction of supernatants and precipitates. This process was repeated several times in order to obtain fractions of GQDs with a uniform size. The obtained supernatant of GQD solution was strongly fluorescent with a uniform size. The obtained supernatant of GQD solution was strongly fluorescent with a uniform size.

2.2. 'Bottom-up' Approach for Fabricating Graphene Quantum Dots based on Carbonization and Heteroatom Doping

2.2.1. Carbonization of citric acid

In a typical procedure of GQDs preparation, 2 g of citric acid (CA) was put into a beaker and heated to 200 °C using heating mantle. About 5 min later, the CA was liquated. Subsequently, the color of the liquid was changed from colorless or pale yellow, and then orange in 30 min, implying the formation of

GQDs. If the haeating was kept on, the orange liquid would finally turn to black solid in about 2 h, suggesting the formation of GO. The obtained orange liquid for preparing GQDs was added drop by drop into 100 mL of 10 $mgmL^{-1}$ NaOH solution, under vigorous stirring. After neutralized to pH 7.0 with NaOH, the aqueous solution of GQDs was obtained. The black solid was dissolved with 50 mL of 10 mg mL^{-1} NaOH solution, and further neutralized with the same concentration of NaOH, resulting the aqueous solution of GQD.

2.2.2. Controllable S, N-doping of graphene quantum dot.

For the S-doped GQD, 2 g citric acid and 0.56 mL H_2SO_4 with a molar ratio 1: 1 were put into a round-shaped flask and stirred to form a clear solution. Then the solution was heated to 100 °C in a heating mentle and kept for additional 10 minutes. Subsequently, the color of liquid was changed to pink and then getting darker, indicating the formation of graphene oxide. For the following N-doping, 10 mL DMF (dimethyl formamide) was added to the clear pink S-doped GQD solution. Then the temperature was increased to 200 °C and kept for additional 30 minutes. Finally, as-synthesized S, N-doped GQD was collected by adding ethanol into the solution and further neutralized with NaOH, resulting the aqueous solution of GOD.

2.3. Applications

2.3.1. FRET-based dye-sensitized solar cells for near-infrared light harvesting

For use as light-harvesting antennae in FRET-based photovoltaic devices, the GQD was passivated by polyethylene glycol (PEG) for high fluorescent quantum yield. PEG molecules were anchored onto the surface of GQD *via* hydrothermal route at 200 °C for 2 h. Then, the PEG-passivated GQDs were deposited onto the top of a TiO_2 working electrode of DSSCs *via* spin coating. For the preparation of GQD-layer modified photoanode, TiO_2 mesoporous film was prepared by screen-printing of P25 based TiO_2 paste on FTO-type TCO glass and sintered at 450 °C in air for 30 min. The PEG-passivated GQD solution was spin-coated on top of the as-prepared nanoporous TiO_2 layer at 500 rpm for 20 sec from a solution with a concentration of approx. 0.5 mg/ml. The as-prepared TiO_2/GQDs films were treated with a 40 mM titanium tetrachloride ($TiCl_4$) solution and heated at 450 °C in air for 30 min before use. The GQD-deposited TiO_2 thin film was immersed in the dye solution (0.5 mM D719 dye in acetonitrile and t-butanol (volume ratio of 1 : 1)) for 36 h at 25 °C. For the preparation of Pt-counter electrode, a drop of 5 mM H_2PtCl_6 ethanol solution was spread out onto the FTO glasses, and thermal treated at 400 °C for 15 min under air. The working electrodes were assembled with Pt-FTO

electrodes into sandwich- type cells using thermal adhesive films (Surlyn: 60 μm, Dupont). A drop of electrolyte (Iodolyte AN-50, Solaronix), consisting of 50 mM triiodide, 0.1 M LiI, and 0.5 M 1,2-dimethyl-3-propylimidazolium iodide in acetonitrile, was injected into the cell.

2.3.2. Graphene quantum dot-based fluoresent sensor for rapid and ultrasensitive detection of an anthrax biomarker

For the preparation of Eu-modified GQD, GQD (0.1 g) in 5 mL of distilled water were reacted with ethylene diamine (EDA) (0.1 mL) for 2 h and centrifuged. Next, the product was reacted with ethylenediamine teraacetic acid dianhydride (EDTAD) (0.1 M; 1 mL) for 2 h. Subsequently, the product was redispersed in aqueous solution of $EuCl_3$ (0.1 M; 1 mL) by sonication and stirred for 3h. The product (Eu-GQD) was centrifuged and washed with distilled water. The DPA detection of Eu-GQDs was measured by fluorescence spectra analysis with a JASCO FP-6500 spectrofluorometer. The fluorescence intensity changes were observed with increasing the concentration of DPA, and the fluorescence intensity changes of the Eu-GQD were monitored at 616 nm (λ_{ex} = 270 nm) in the presence of DPA (0- 1 μM).

2.3.3. Photoinduced electron transfer based sensor probes for intracellular hydrogen peroxide

To graft boronate on the surface of GQD, 5 mg amount of 1-ethyl-3-(3-dimethylaminopropyl) carbodiimide and 5 mg amount of N-hydroxysuccinimide were added in an aqueous solution of GQD (1 mg/mL) at 20 °C for 3 h. Then, the product was treated with folic acid solution (8 mM; 1.5 mL) for 6 h to synthesize the F-GQD. Subsequently, the product was reacted with 2-aminopyrimidine-5-boronic acid pinacol ester (15 mM; 1.5 mL) for 6 h. (B-GQD) The quantum yield of BGQD was calculated by a comparison method of the fluorescence emission with the standard reference, 7-amino-4-methylcoumarin (AMC; Aldrich). AMC has been widely used as a blue-emitting dye due to their high quantum yield ($\Phi = 0.88$).

For the H_2O_2 and ROS detection in the presence of various metabolites, the fluorescence intensity changes of BGQD were monitored at 360 nm (λ_{ex} = 490 nm). A 0.1 M HEPES buffer solution and 1 cm × 1 cm quartz cuvettes were used in all experiments. The concentration of the BGQD was fixed at 10 μg mL^{-1}. H_2O_2 and OCl^- were obtained from 35% hydrogen peroxide (Aldrich) and 5% sodium hypochlorite solution (Hanawa Chemical Pure, Osaka, Japan), respectively. ·OH and ·OtBu were acquired by reaction of 1 Mm Fe^{2+} with 100 μM H_2O_2 or 100 μM TBHP, respectively. In order to confirm interference

effect of metabolites, 10 μg mL^{-1} BGQD and 1 mM metabolites were mixed, and they were reacted with H_2O_2. Ca^{2+}, L-glutamine, and L-ascorbic acid were selected as representative ion, amino acid, and vitamin, respectively.

The rate of conversion from BGQD to oxidized BGQD was calculated under pseudo-first order conditions with excess H_2O_2. A BGQD solution (10 μg m L^{-1}, 3.0 mL) was added to H_2O_2 to final concentrations of 20, 40, 60, 80, and 100 μM. The change in absorbance at 360 nm was monitored over 0.5-5 min. The slope of the linear fit of $\ln[(A-A_{\text{oxidized BGQD}})/(A_0-A_{\text{oxidized BGQD}})]$ *vs* time gives observed rate constant k_{obs} (where A_0 and $A_{\text{oxidized BGQD}}$ are the initial absorbance of BGQD and the absorbance of a 10 μg mL^{-1} oxidized BGQD, respectively). The rate constant k (M^{-1} s^{-1}) was determined from the slope of the line of K_{obs} *vs* $[H_2O_2]$.

For the Cell culture, human breast cancer MCF-7 cells (FR+) and human breast cancer SK-BR-3 cells (FR-) were purchased from American Type Culture Collection (Manassas, VA, USA). Both cells were cultured in RPMI-1640 medium with 10% fetal bovine serum and 1% penicillin-streptomycin solution. They were maintained in a 75T flask at 37 °C in humidified 5% CO_2 atmosphere and passaged at 70-80% confluence.

For the titration assay, 3×10^3 MCF-7 and SK-BR-3 cells per well were seeded in black, opaque, 96-well plates and inserted with the BGQD (2.5~15

μg mL^{-1}) for 24 h. Then, PMA (1~10 μg mL^{-1}) was added to the cells for 30 min at 37 °C. Fluorescence intensity was detected by $Victor^3$ multilabel readers (Perkin-Elmer, Boston, MA, USA) at an excitation wavelength of 565 nm and an emission wavelength of 460 nm due to restriction of the fluorescence lamp of the instrument.

For the Observation of TGQD and BGQD treated cells. MCF-7 and SK-BR-3 cells were spread at a density of 3000 cells per well, in 8-well Lab-Tek II chambered coverglass (Nunc, Thermo Fisher Scientific, USA) and treated with 10 μg mL^{-1} of TGQD and BGQD. After 24 h, the supernatant was removed and the cells were washed twice with 0.1 M phosphate buffered solution (PBS). Then, the cells were treated with 5 μM phorbol-12-myristate-13-acetate (PMA, Sigma) solution for 10 min at 37 °C. The cells were analyzed with a Delta Vision RT imaging system (Applied Precision, Issaquah, WA, USA) under 5% CO_2 at 37 °C. To obtain images, a Cascade II electron multiplying charge-coupled device camera was used. The excitation and emission filter were used as Rd-TR-PE and DAPI, respectively, to restriction of the fluorescence lamp of the instruments.

For the Viability test, **t**he cell viability was measured using Cell-Titer glow luminescent cell viability assay (Promega, Madison, WI, USA). This assay is a homogeneous method of estimating the number of viable cells based on the

ATP content. MCF-7 cells were seeded in white opaque 96-well plates at a density of 1.5×10^4 cells mL^{-1} for 24 h, and BGQD or TGQD were inserted for another 24 h. Then, cell medium was removed and following steps were carried out as manufacturer's instructions. The luminescence was detected by Victor^3 Multilabel Readers (Perkin Elmer, Boston, MA, USA) at 595 nm. The viability was calculated by dividing the ATP content of BGQD or TGQD treated cells by that of untreated cells (negative control).

For the ROS production, the intracellular ROS was measured by 2',7'-dichlorodihydrofluorescein diacetate (H_2DCF-DA; Invitrogen, Grand Island, NY, USA) staining. MCF-7 cells were seeded in black opaque 96-well plates at a concentration of 1.5×10^4 cells mL^{-1} and treated with BGQD or TGQD for another 24 h. They were washed with 0.1 M Hank's Buffered Salt Solution twice and treated with 10 μM H_2DCF-DA for 30 min at 37 ^oC. Fluorescence intensity was detected by Victor Multilabel Readers (Perkine Elmer, Boston, MA, USA) at an excitation wavelength of 485 nm and an emission wavelength of 535 nm.

3. RESULTS AND DISCUSSION

3.1. 'Top-down' Approach for Fabricating Uniform Graphene Quantum Dots with Sizes.

The overall synthetic procedure for GQDs is shown in Figure 8. Under our experimental conditions, the GQDs are synthesized by excessive chemical oxidation and size-selective precipitation approach of micrometer-sized pitch based carbon nanomaterials (CN) such as graphene oxide (GO), platelet-typed carbon nanofiber (P-CNF), herringbone-typed carbon nanofiber (H-CNF).[21] The small domain structure of sp^2 carbon atoms, such as those in carbon nanofibers has advantages of easy extraction and facile size control of the synthesized GQDs.[39] The CN were oxidized under excessive acidic conditions for 24 h and exfoliated to nanometer-sized graphene oxides.[74] The oxidation process was carried out at temperatures ranging from 80 to 120°C to synthesize GQDs. Then, the pH of the solution was adjusted to 8 with Na_2CO_3. Then, size-selective precipitation was used to isolate the GQDs from the reaction mixture. Ethanol, a non-solvent, was added to the concentrated solution until the Na_2SO_4 salts started to precipitate. Excess Na^+ and SO_4^{2-} ions were present in the GQD solution due to the neutralization reaction between H_2SO_4 and Na_2CO_3; the excess ions combined to form Na_2SO_4 salts in a non-solvent system. From the resulting turbid solution, the precipitate and the

supernatant were perfectly separated by centrifugation. Consequently, uniform nanometer-sized GQDs were separated from Na_2SO_4 salts and larger GQDs under various sedimentation velocity conditions.

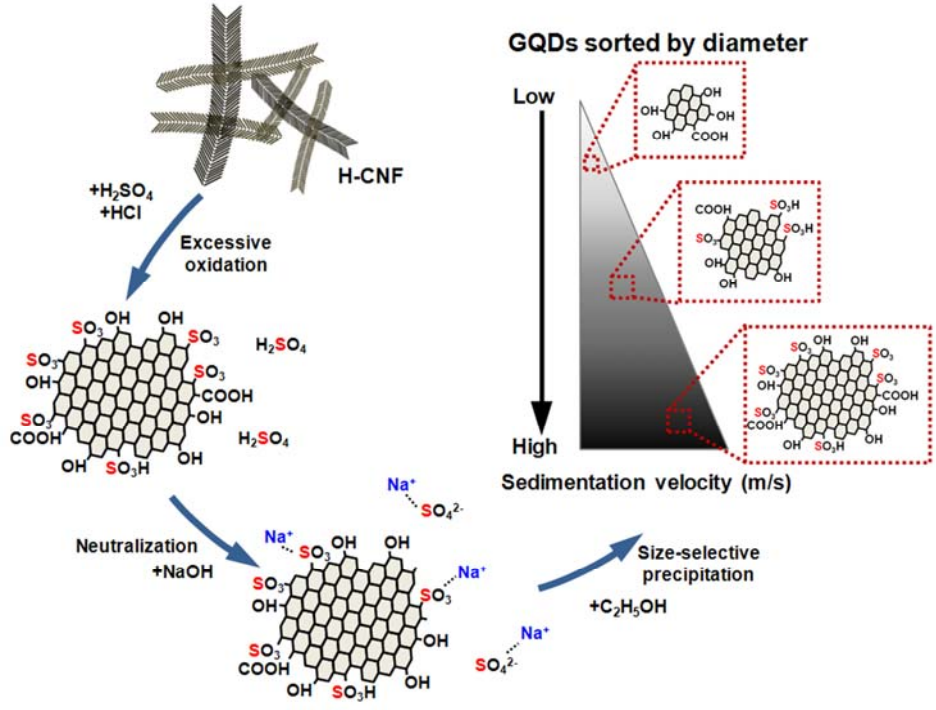

Figure 8. Formation mechanism for the graphene quantum dots (GQDs) *via* chemical oxidation and size-selective precipitation procedures.

3.1.1. Chemical oxidation of various types of carbon materials.

Figure 9 show transmission electron microscopy (TEM) images of pristine CNs and as-synthesized GQD by chemical oxidation for 24h. During the oxidation process, the CNs are exfoliated and cut to the nanometer-sized GQDs. The GQD originated from H-CNF indicates narrow size-distribution and small diameters (3 nm ± 10 nm) compared to that of P-CNF (5 nm ± 14 nm) and GO (17 nm ± 25 nm).[75] This is attributed to the smaller structural units (ca. 50 nm) of the H-CNF, facilitating oxidization and cut for the nanometer sized GQDs.[76] Moreover, the GQD originated form H-CNF shows the excellent dispersity in the aqueous solution.

Figure 10 shows the UV-vis absorption spectra of three types of GQD fabricated from different CNs. It shows a development of new absorption band at 300 nm, which are silimar to the graphene quantum dots prepared by a hydrothermal graphene oxide reduction method.[44] In contrast, the pristine CNs exhibits a broad UV-vis absoprtion below 600 nm, suggesting that those sp^2 clusters containined in GO and CNF is not uniform in size.[77] As the oxidization time increases, the overall absorption of GQDs increases with relative decrease of the band at 300 nm. The origin of the peak is related to π electron transition in oxygen-containing GQD. The absorption peak at 300 nm corresoponds to $n \rightarrow \pi^*$ transition of C=O bond.[78] In addition, Figure 11

also demonstrates the PL spectra of as-prepared GQDs orginated from different CNs. The fluorescence intensity increases in the order of GO < P-CNF < H-CNF. This result is in accordance with the monodisperse GQD of H-CNF in nanometer size range. Taking these results into account, it is concluded that small and uniform structural unit of H-CNF gives monodisperse size distribution and high fluorescent intensity of GQD.

Raman spectroscopy was also used to characterize the GQDs, as shown in Figure 12. The G peak shows blue shift *ca*. 2 nm compared with the original CF. The D peak of GQDs can be found at 2700 cm^{-1}. The relative intensity of the "disorder" D band to the crystalline G-band (I_D/I_G) for the GQDs is 0.91, indicating the increase of defect compared to that of pristine H-CNF (1.18).[1]

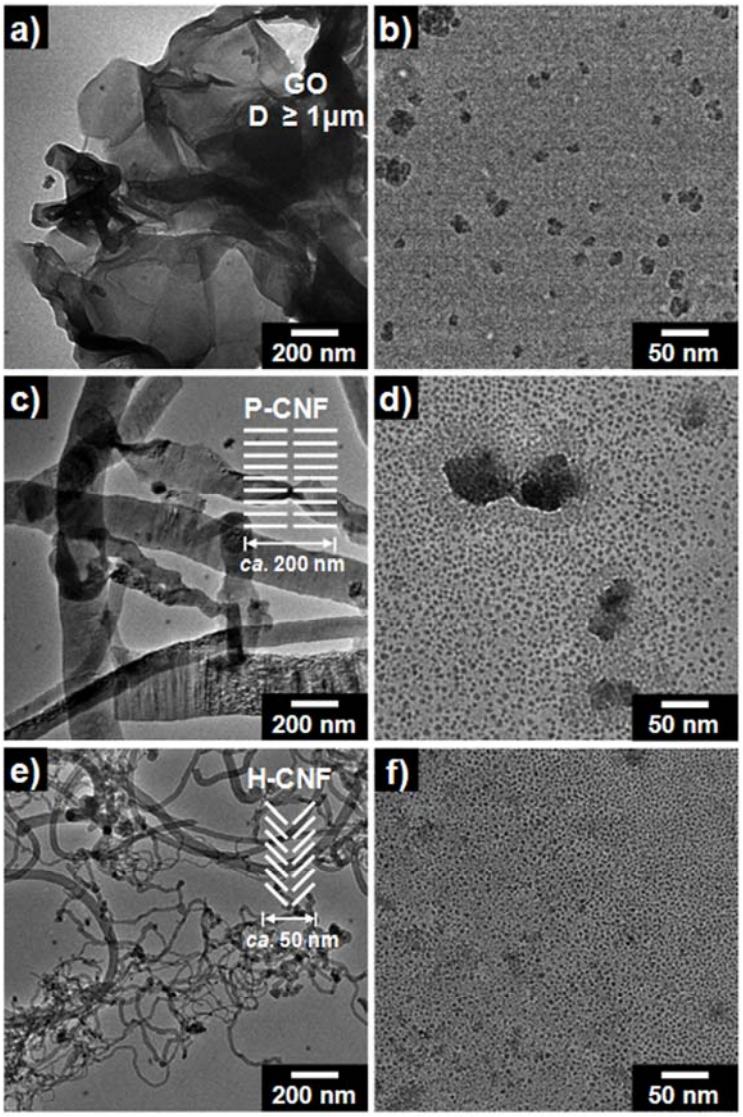

Figure 9. TEM images of (a) pristine GO, (b) 24 h-oxidized GO, (c) pristine P-CNF, (d) 24h-oxidized P-CNF, (e) pristine H-CNF, and (f) 24h-oxidized H-CNF.

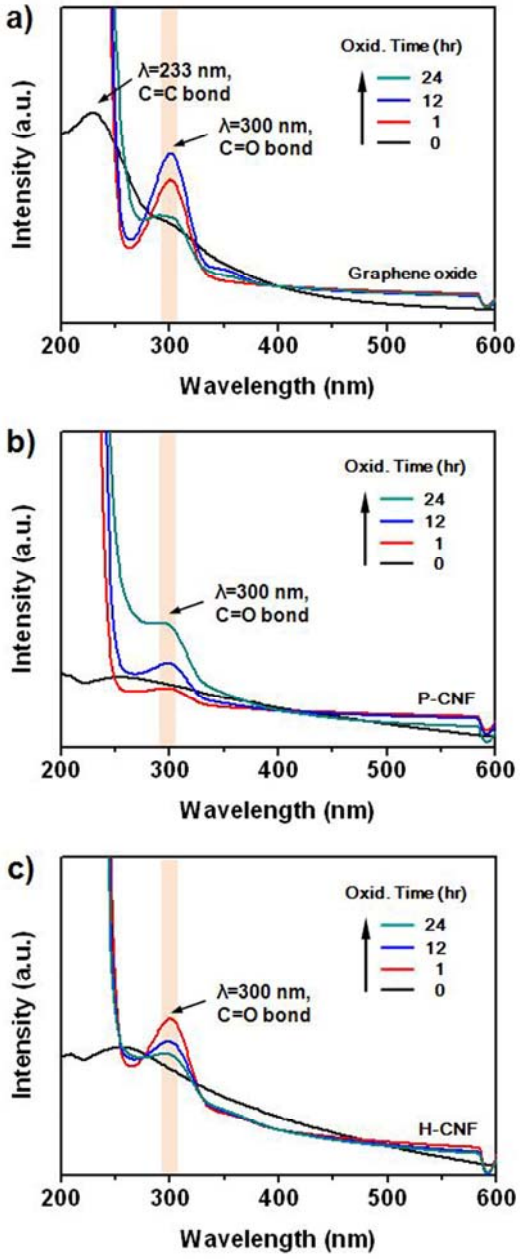

Figure 10. The UV-vis absorption spectra of GQDs fabricated by (a) graphene oxide(GO), (b) Platelet typed-carbon nanofiber(P-CNF), and (c) Herringbone typed-carbon nanofiber(H-CNF).

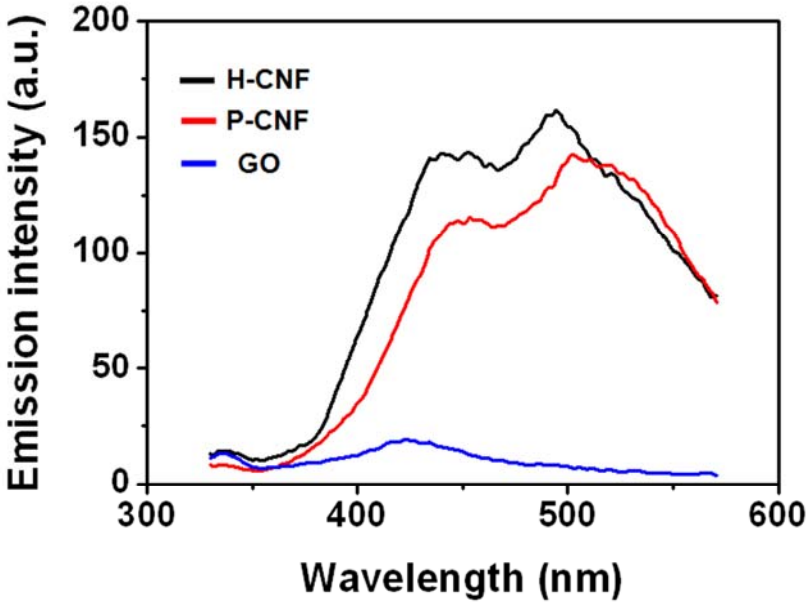

Figure 11. The PL spectra of as-prepared GQDs orginated from graphene oxide(GO, blue line), platelet typed-carbon nanofiber(P-CNF, red line), and herringbone typed-carbon nanofiber(H-CNF, black line).

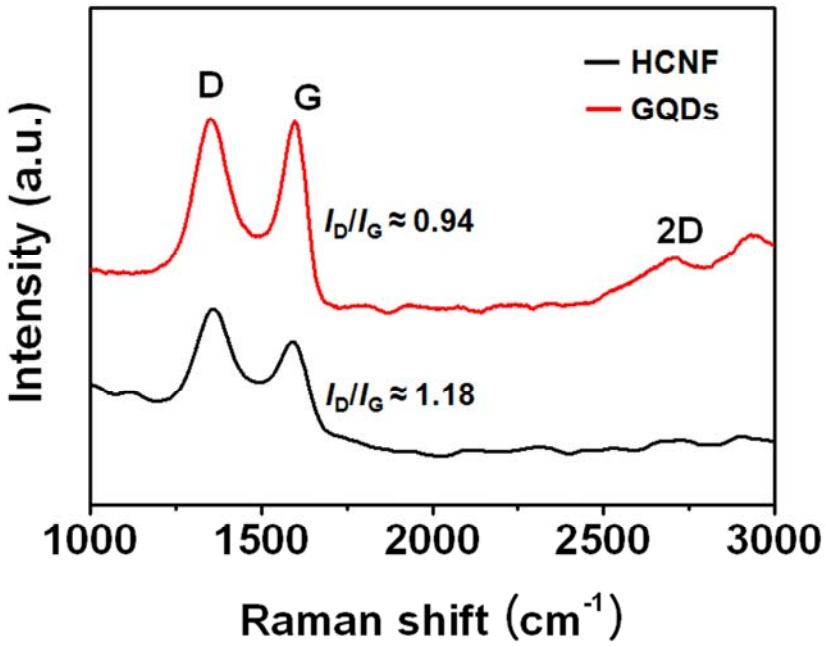

Figure 12. Raman spectra of pristine H-CNF and the as-prepared GQD.

To control the oxidation condition of H-CNF, the molar ratio of hydrochloric acid and sulfuric acid was varied from 1:3 to 3:1 in Figure 13. In the case of GQDs with higher ratio of H_2SO_4, fluorescene intensity increases compraed to that of higher ratio of HCl, indicating high fluorescence quantum yield of ca. 2%.

In addition, the oxidation temperature of H-CNF was varied from 80 to 140 °C and UV-vis absorption and PL spectra was analyzed (Figure 14). The as-prepared GQDs show two clear absoption bands at 300 and 350 nm in Figure 14a. The orgin of these peak is related to π electron transition in oxygen-containing GQDs. The absorption peak at 300 nm is due to n → π* transition of C=O bond, and the absoprtion at 350 nm corresponds to n → π* transition of the C–S bond. When the oxidation temperature increases from 80 to 140 °C, the 300 nm peak of C=O bond gradually decreased with the increase of 350 nm peak of C–S bond, indicating the enhancement of S doping levels of GQDs due to the sulfuric acid. The result reveals that the reaction temperature can affect the absorption properties of as-sythesized GQDs and that high temperature leads to GQDs absorption at longer wavelenths.

Figure 14b shows the PL spectra of GQDs with different oxidation temperatures from 60 to 120 °C, which were excited at 350 nm. The as-prepared GQDs show two emission bands at 469 nm and 530 nm. In the case of

GQD with low oxidation temeperature, the PL results revealed that high intensity at the 530 nm band and low intensity at 469 nm band. However, as the oxidation temperature increase, the peak at 530 nm gradually decreased and the peak at 469 nm increased, resulting the 120 °C-oxidized GQD has narrow PL band. The result reveals that the temperature can change the distribution of emission wavelength of as-synthesized GQDs. Different emission color may originate from GQDs of different size, shape and defects. Further characterization (typical TEM images and size distribution for GQDs) supports the conclusion that different-sized GQDs yield different emission colors.

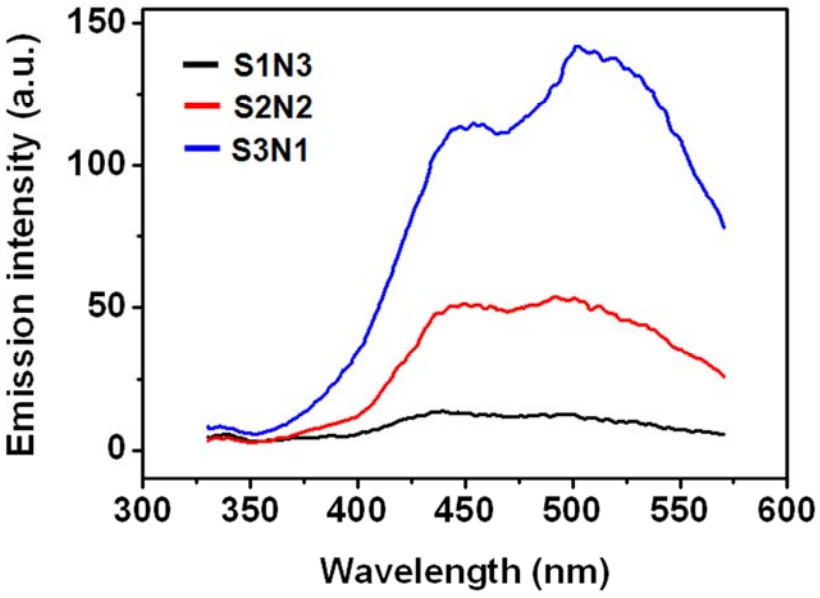

Figure 13. The PL spectra of GQDs fabricated by different oxidation conditions(volume ratio of H_2SO_4: HNO_3); 3:1 (blue line), 2:2 (red line), 1:3 (black line). H-CNF was used as carbon sources.

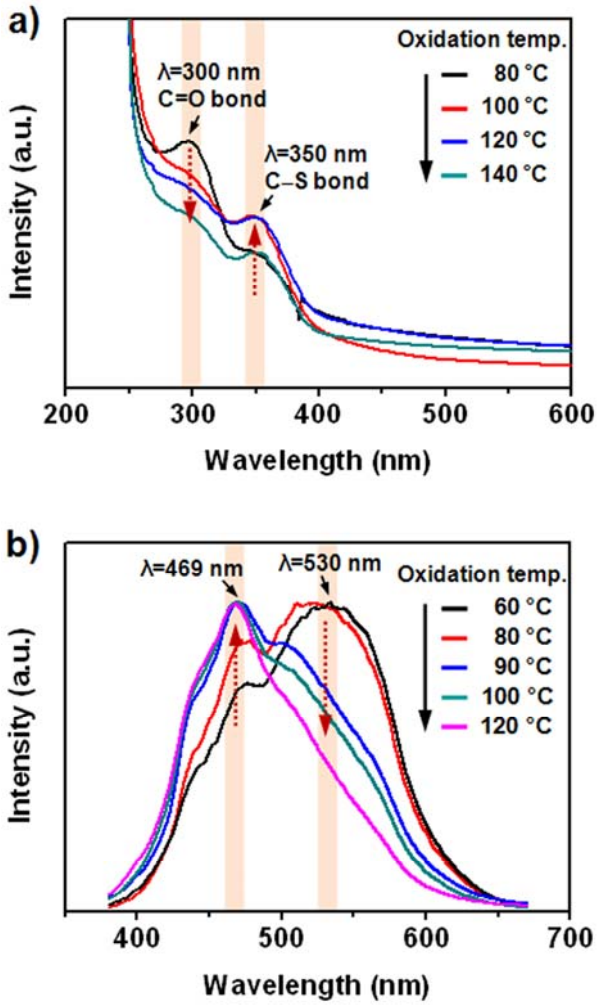

Figure 14. (a) The UV-vis absorption spectra of the as-prepared GQDs with different oxidation temperatures; 80, 100, 120, and 140 °C. (b) PL spectra of GQDs with different oxidation temperatures (60, 80, 90, 100, and 120 °C), which were excited at 350 nm. H-CNF was used as carbon sources.

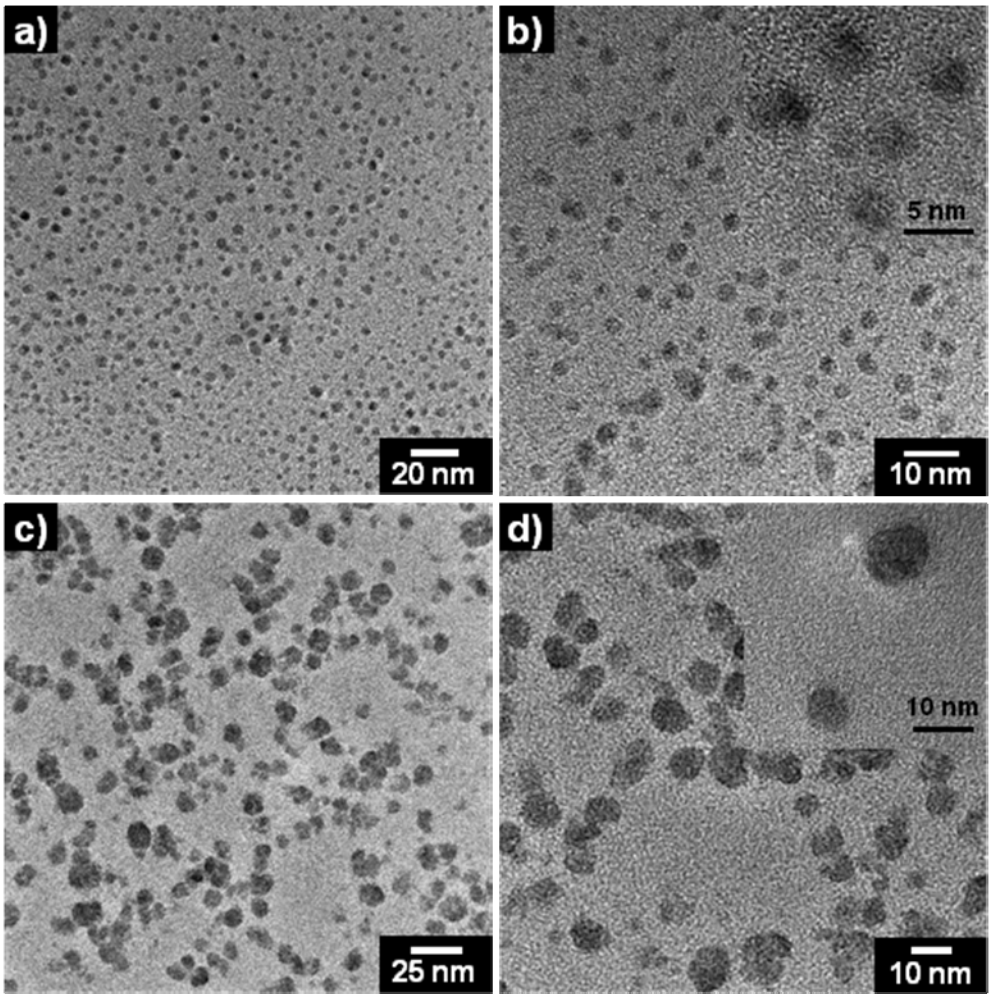

Figure 15. TEM images of GQDs prepared *via* excessive oxidation and size-selective precipitation. (a–b) 3-nm-diameter GQDs and (c–d) 10-nm-diameter GQDs. (insets: corresponding HR-TEM images of GQDs).

Figure 15 indicates TEM analysis of GQDs prepared by different oxidation temperature (80 and 120 °C). The 80 °C-oxidized GQD has *ca.* 3 nm of average diameter. And the 120 °C-oxidized GQD has *ca.* 10 nm of average diameter. From the above results, it could be concluded that the different oxidation temperature yields different-sized GQDs with different emission colors.

Under our experimental condition, the zeta potential measurements show a linear increase in the zeta potential with respect to increasing oxidation levels. In Figure 16, the zeta potential values of 80°C-, 100°C- and 120°C-oxidized GQDs were found to be -17.3, -23.2, and -27.8 mV, respectively. The negative zeta potential values are due to the presence of electronegative functional groups formed at the graphite lattice during the oxidation process.[1] With the successive increase in the oxidation temperature, a greater number of electronegative functional groups are formed in GQD resulting in the increase of the zeta potential at higher oxidation levels. Accordingly, the results for the high oxygenated functional groups with higher zeta potential in an aqueous medium is more likely due to the dissociation of a greater number of acidic groups at the surface thereby resulting in a higher zeta potential.

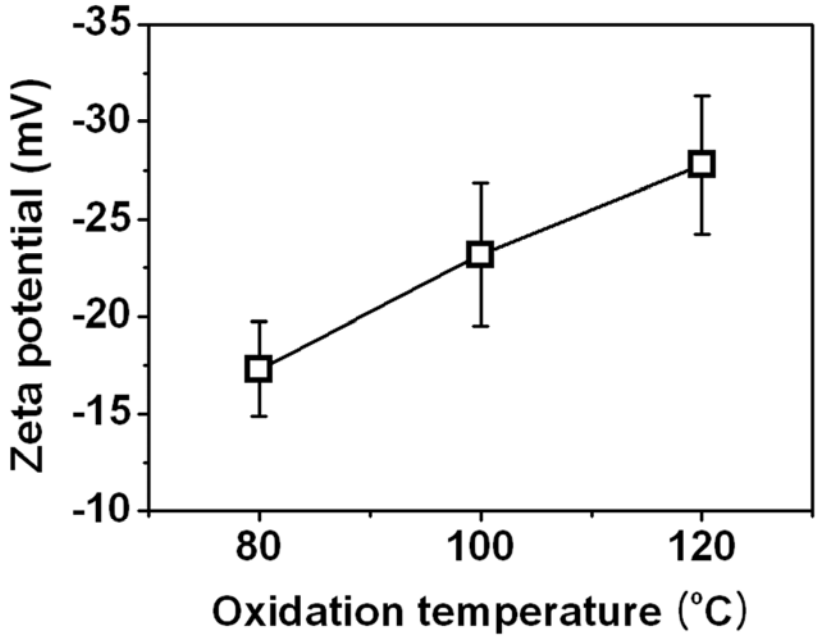

Figure 16. Plot of zeta potential *vs.* GQD samples with different oxidation levels. Smoluchowski approximation was used for the conversion equation of zeta-potential.

3.1.2. Separation of graphene quantum dots *via* size-selective precipitation approach.

The size-selective precipitation approach was used to isolate the GQDs from the reaction mixture in Figure 17. Ethanol, a non-solvent, was added to the concentrated solution until the Na_2SO_4 salts started to precipitate. Excess Na^+ and SO_4^{2-} ions were present in the GQD solution due to the neutralization reaction between H_2SO_4 and Na_2CO_3; the excess ions combined to form Na_2SO_4 salts in a non-solvent system. From the resulting turbid solution, the white crystalline precipitate and the yellowish transparent supernatant were perfectly separated by high speed centrifugation in Figure 17b. Consequently, uniform nanometer-sized GQDs were separated from Na_2SO_4 salts and larger GQDs under various sedimentation velocity conditions.

Figure 18 shows FT-IR spectra of precipitate and supernatant after sedimentation process. The FT-IR spectrum of the precipitate shows characteristic SO_4 asymmetric bending at 640 cm^{-1}, SO_4 symetric stretching at 1100 cm^{-1}, and O–H stretching peak at 3449 cm^{-1}, indicating the major products are Na_2SO_4. The FT-IR spectrum of supernatant presents characteristic C–O stretching at 1100 cm^{-1}, C=C aromatic stretching at 1591 cm^{-1}, C=O stretching at 1785 cm^{-1}, C–H stretching at 2882 cm^{-1}, indicating the presence of GQDs.

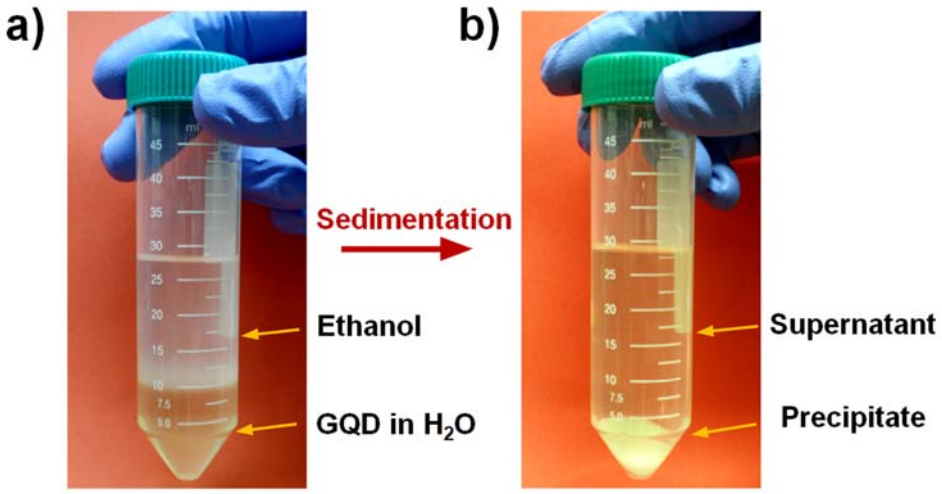

Figure 17. Digital photograph of GQD solutions (a) before and (b) after separation process.

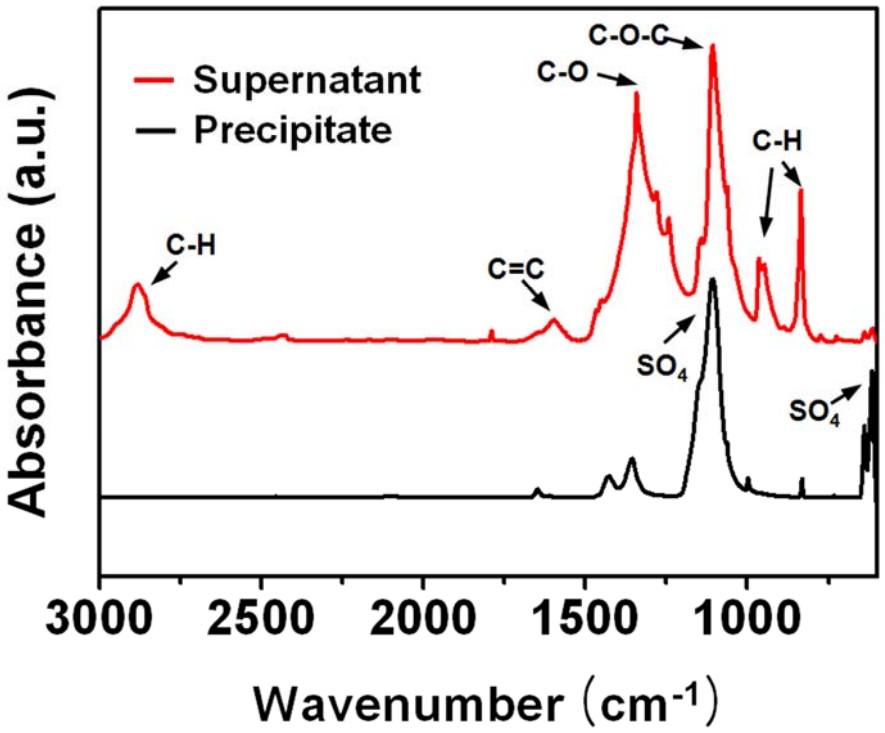

Figure 18. FT-IR spectra of supernatant and precipitate after size-selective precipitation process.

Figure 19 show transmission electron microscopy (TEM) images of pristine HCNFs and GQDs at each size-selective precipitation step. The pristine HCNFs had diameters of *ca*. 50–100 nm (Figure 19a). After excessive oxidation and PEG anchoring steps, the as-synthesized GQDs had diameters of *ca*. 5–40 nm with a broad size distribution (Figure 19b). After each separation step, the supernatant and precipitate showed significant differences in morphology and in the size of the GQDs (Figure 19c-d). The size distributions measured using TEM were *ca*. 5–40 nm and *ca*. 5–15 nm for the precipitates and supernatant, respectively. Namely, the supernatant after separation process have a uniform morphology and a narrow size distribution compared with that of precipitate.

We also investigated the size distribution of GQDs before and after the size-selective precipitation process using dynamic light scattering (DLS) analysis in Figure 20. Under our experimental condition, the GQDs before separation showed broad distribution in the range of 6 nm to 3 μm. However, GQDs after separation process showed narrow distribution with 12 nm peak. This result is corresponding to the results from TEM measurement in Figure 19. Figure 21 shows the PL spectra of 80 °C-oxidized GQD and 120 °C-oxidized GQD before and after size-selective precipitation process. After the separation process, both of the emission peaks of 80 °C- and 120 °C-oxidized GQDs were

blue-shifted about 15 nm and the emission spectral width was narrowed. This is attributed to the uniformity of size and shape of the GQDs after the size-selective precipitation step.

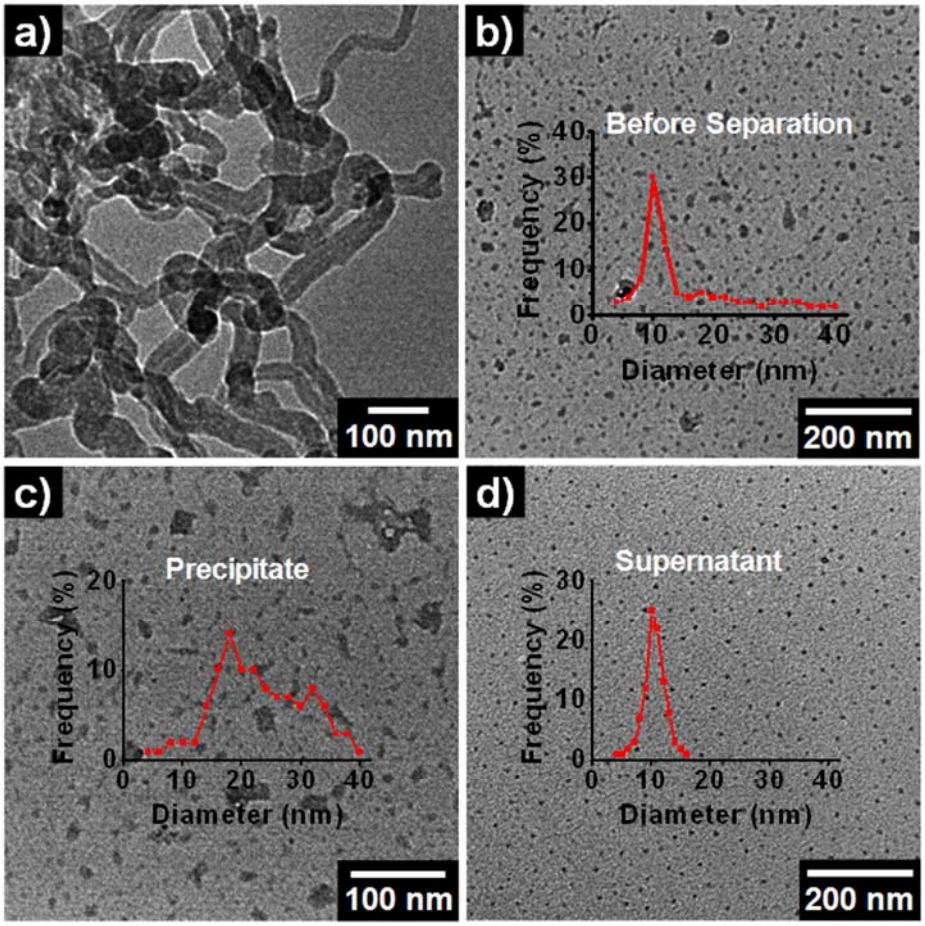

Figure 19. TEM images for (a) pristine HCNFs, (b) as-synthesized GQDs before size-selective precipitation step, (c) precipitate and (d) supernatant after size-selective precipitation step (inset indicates the corresponding size-distribution analysis of GQD).

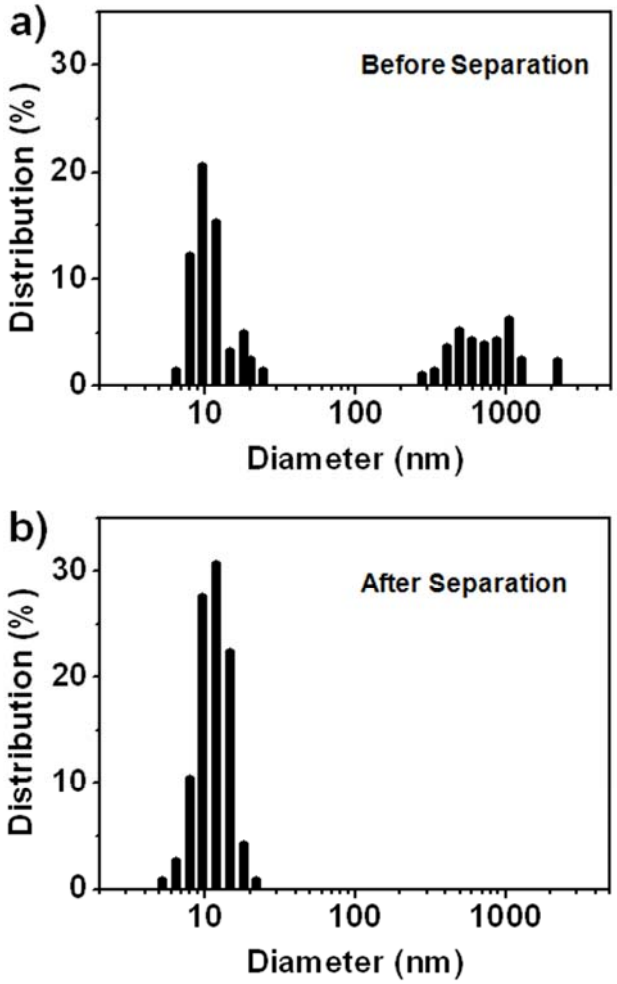

Figure 20. Size distribution of (a) GQDs (80 °C) before separation and (b) GQDs (80 °C) after separation process measured by Dynamic light scattering spectroscopy(DLS).

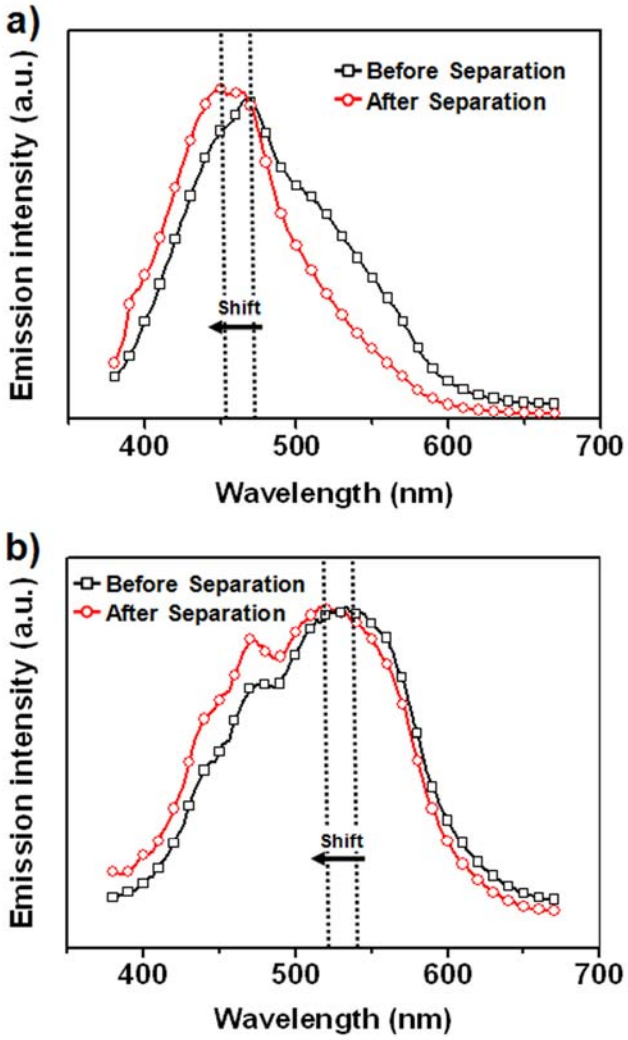

Figure 21. PL spectra of GQDs before and after the size-selective precipitation; (a) 120 °C-oxidized GQD and (b) 80 °C -oxidized GQD.

Discrete nanomaterials dispersed in a fluid exhibit a divergent sedimentation trend as a function of size, morphology, structure, and other properties.[79] Thus, the predominant dispersion stability of smaller GQDs is attributable to the sedimentation velocity, which is an important factor in particle precipitation.[80] Stoke's law, a formula for determining the rate of sedimentation, indicates that a particle moving through a viscous liquid attains a constant velocity or sedimentation rate.[81] The equation for Stoke's law of sedimentation is as follows:

$$V_g = d^2(\rho_p - \rho_1)/18\eta \times G \quad (1)$$

Where V_g is the sedimentation velocity, d is the particle diameter, ρ_p is the particle density, ρ_1 is the liquid density, η is the viscosity of liquid, and G is the gravitational acceleration. Under our conditions, the sedimentation velocity (V_g) was 1.64×10^{-11} and 1.15×10^{-9} $m \cdot s^{-1}$ for 10- and 50-nm GQDs, respectively (Table 1). It is noteworthy that the V_g value of 10-nm GQDs was *ca.* 70 times slower than that of 50-nm GQDs. It was also expected that the slower settling velocity of smaller GQD sheets and the limited formation of Na_2SO_4 salts on smaller GQD sheets would have a synergistic effect and enhance the anti-sedimentation properties.

Table 1. Physical parameters and sedimentation velocity of GQDs.

	3-nm GQD	**50-nm GQD**
Diameter [a]	*ca*. 3 nm	*ca*. 50 nm
Density [b]	1.15 g/cm^3	2.37 g/cm^3
Fluid density [c]	0.789 g/cm^3	0.789 g/cm^3
Fluid viscosity [c]	0.0012 Pa·s	0.0012 Pa·s
Sedimentation velocity [d]	1.64 x 10^{-11} m/s	1.15 x 10^{-9} m/s

[a] The average diameter of GQDs was determined by TEM (50 GQDs counted). [b] The density of GQDs was obtained using density hydrometer at a standard temperature of 20 ºC. [c] Ethanol was used as a dispersing medium. [d] Stoke's settling equation was used for calculation of sedimentation velocity. GQD Reynolds number less than 0.2.

3.2. 'Bottom-up' Approach for Fabricating Graphene Quantum Dots based on Carbonization and Heteroatom Doping.

The S, N-doped GQD was prepared through a facile carbonization approach of citric acid under the sulfuric acid (H_2SO_4) and dimethylformamide (DMF) condition (Figure 22). Under the catalytic reaction conditions of H_2SO_4, citric acid undergoes dehydration forming a graphitic hexagonal matrix.[82] During the carbonization of citric acid, H_2SO_4 plays two roles for the preparation of S-doped GQD. One is to catalyze the dehydration of citric acid under acidic conditions.[56] The other is to provide S-doping sources, resulting sulfonic acid and sulfonyl group on the surface of GQD. The benzene ring of GQD reacts slowly with sulfuric acid to give benzenesulfonic acid *via* electrophilic aromatic substitution reaction (S-doped GQD). Then, DMF was added to the reactant when the color of the liquid was changed from colorless to orange in 20 min, implying the formation of S-doped GQD.[83] Since DMF could be decomposed to dimethylamine and carbon monoxide at temperature higher than its boiling point, DMF served as a quenching solvent for the growth retardation to graphene oxide and source of nitrogen. [57] Then the decomposed dimethylamine was doped into the GQD *via* peptide bonding with carboxylic acid group on the surface of GQD.

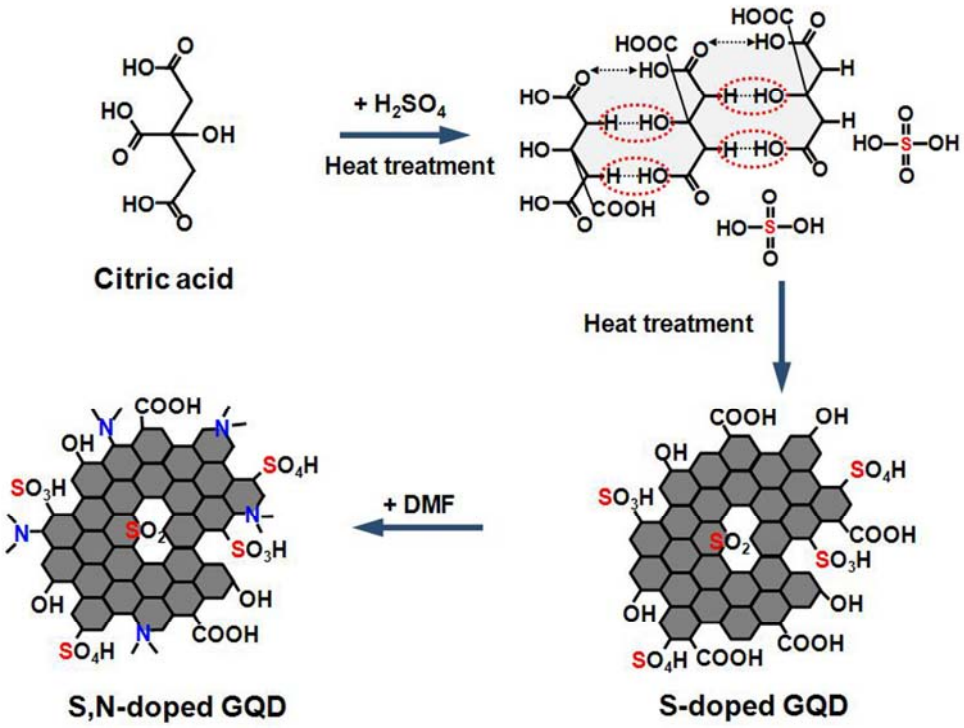

Figure 22. Schematic diagram for the fabrication procedure of S, N-doped GQD.

3.2.1. Carbonization of citric acid

The formation of GQDs was confirmed by TEM analysis (Figure 23). The TEM observation revealed that the diameter of GQDs increased with the increase of carbonization time, and finally over 100 nm-sized graphene oxide discs were developed at the 40 min of carbonization. [77]

3.2.2. Controllable S, N-doping of graphene quantum dot

Figure 24 shows the high-resolution TEM images of GQD, S-doped GQD, and S, N-doped GQD. The as-prepared GQDs are well dispersed in narrow size distributions with mean diameters of 10.2 ± 0.4 nm (GQD), 10.8 ± 0.4 nm (S-doped GQD) and 12.3 ± 0.5 nm (S, N-doped GQD), respectively. After doping with S, N atoms, the average diameter of GQD increased to 12.3 nm. A representative HR-TEM images display a lattice spacing distances of 0.25 nm, which are similar to those of graphite (1120) facets (Figure 24).[84] The above results suggest that the GQD might be composed of nanocrystalline cores of graphitic sp^2 carbon atom.[85]

In addition, the formation of GQD, S-doped GQD, and S, N-doped GQD was confirmed using both Fourier-transform infrared (FT-IR) spectroscopy and Raman spectroscopy. In Figure 25, the FT-IR spectrum of the GQDs shows characteristic C–H deformation peaks at 861 cm^{-1}, C–O–C stretching peaks

1215 cm^{-1}, C=C aromatic stretching peaks at 1578 cm^{-1}, C=O stretching at 1700 cm^{-1}, C–H stretching at 2930 cm^{-1}, indicating the successful synthesis of GQDs. Following S-doping with H_2SO_4, the peaks related to sulfur appear, including the C–S stretching at 616 cm^{-1}, S=O stretching at 1042 cm^{-1}. The S, N-doped GQD exhibits new peaks related to amine bond; N–H deformation at 861 cm^{-1}, C–N stretching of tertiary amine at 1090 cm^{-1}, C–H stretching of N–CH_3 at 2809 cm^{-1}, and N–H stretching at 3053 cm^{-1}.

Raman spectroscopy was used to confirm the quality of the S-doped GQD and S, N doped-GQD. Two major features, a D band and G band, were observed at around 1385 and 1575 cm^{-1}, respectively (Figure 26).[86] The relative intensity of the "disorder" D-band and the crystalline G-band (I_D/I_G) for the S, N doped-GQD increased to 0.54 compared to that of S-doped GQD (0.75), indicating the increased defect which is derived from N dopants.[87]

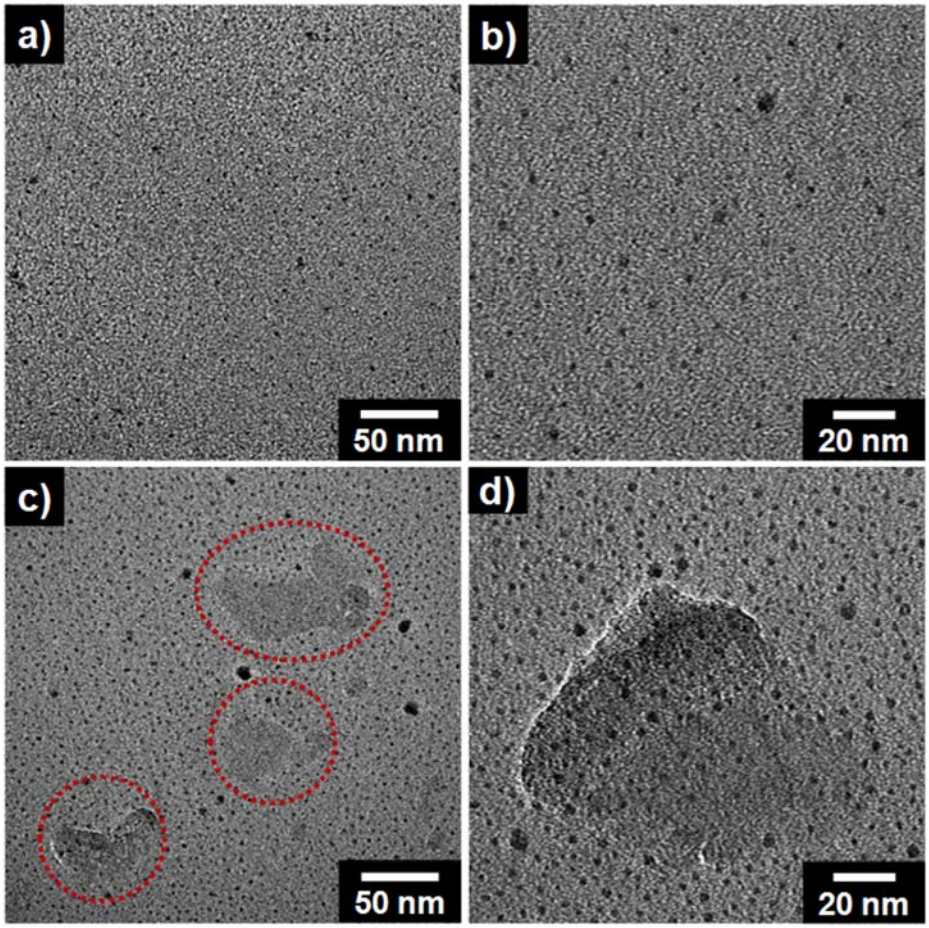

Figure 23. The low-and high-magnification of TEM images of GQD at (a-b) 20 min, and (c-d) 40 min of carbonization time of citric acid. The dotted red circles indicate the as-synthesized graphene oxide, which diameters are about 50 nm.

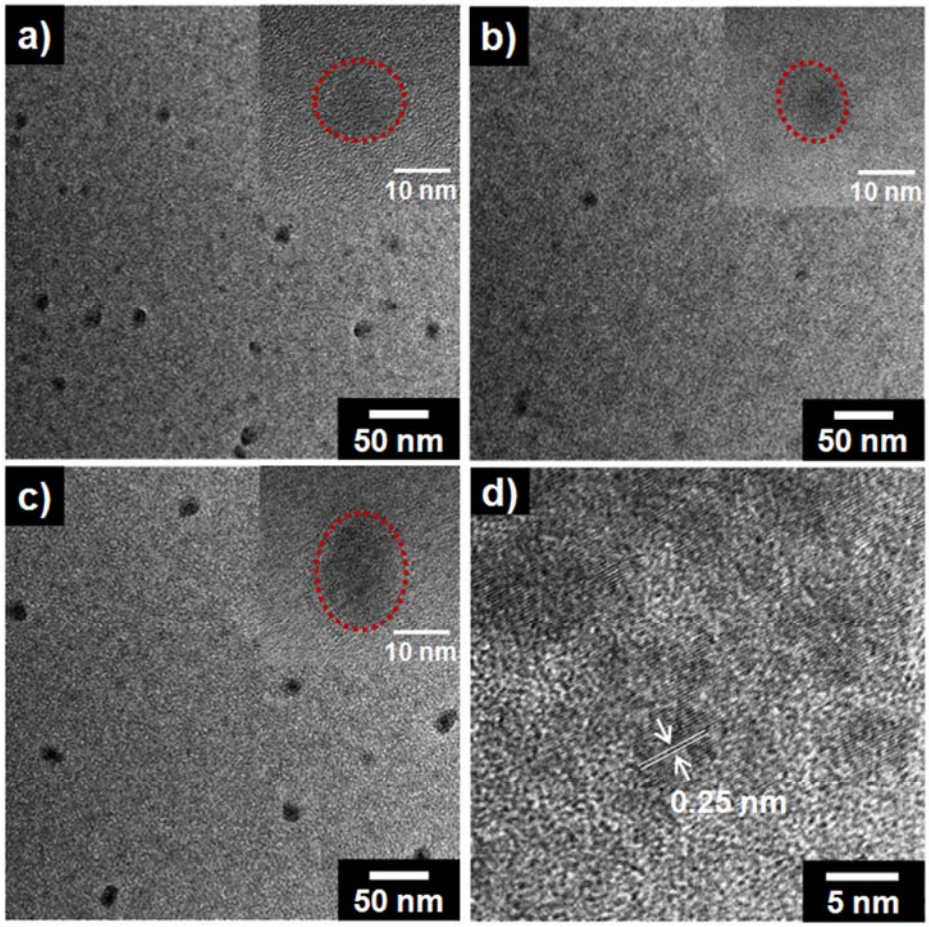

Figure 24. HR-TEM images of (a) pristine GQD, (b) S-doped GQD, and (c) S, N-doped GQD. The inset indicates magnified HR-TEM image of each GQD. (d) The S, N-doped GQDs with lattice parameters of 0.25 nm.

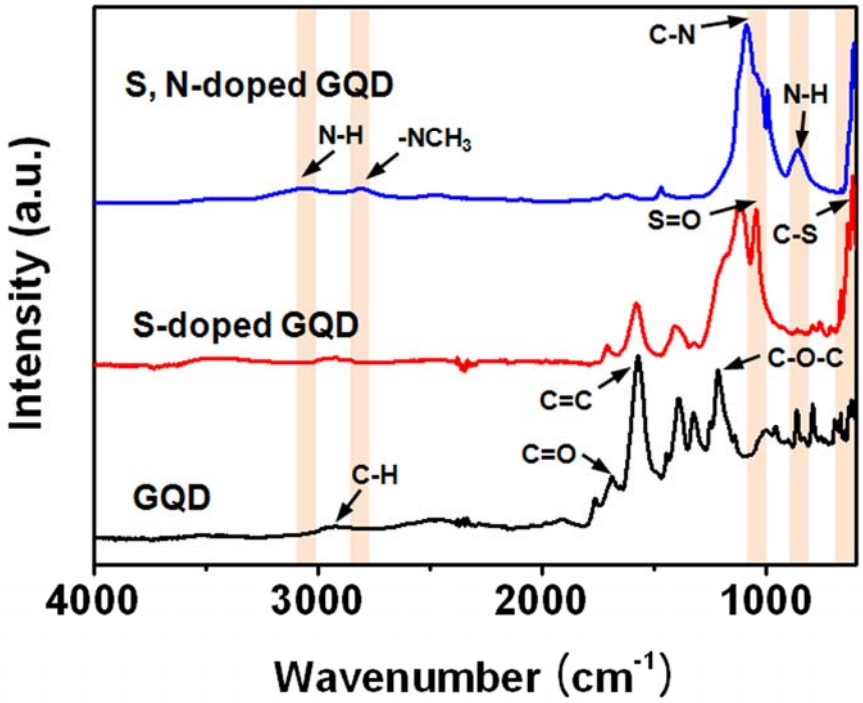

Figure 25. FT-IR spectra of GQD, S-doped GQD, and S, N-doped GQD.

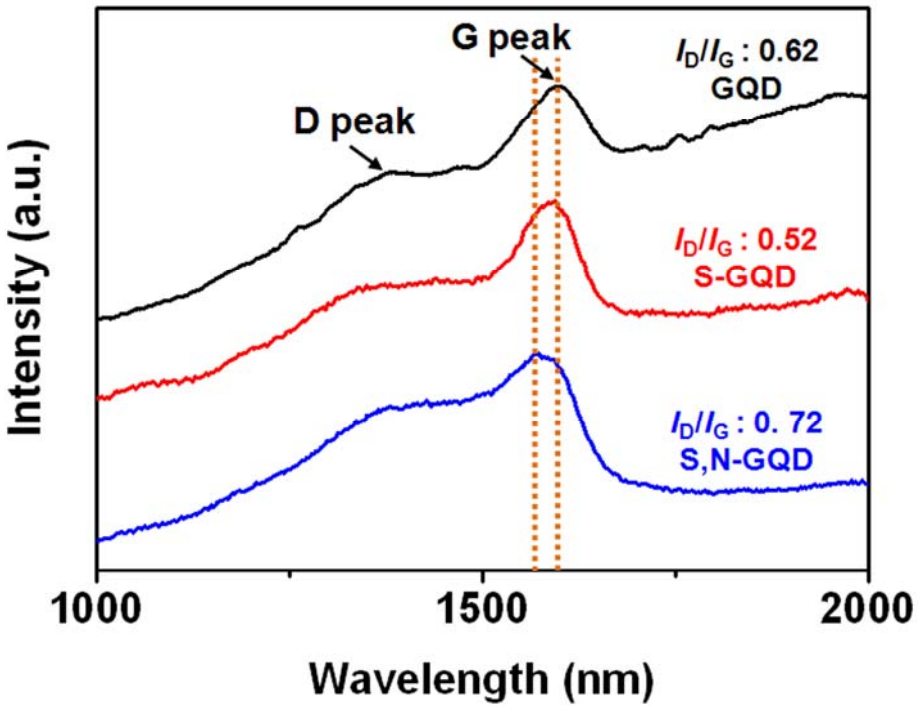

Figure 26. Raman spectra of pristine GQD (black), S-doped GQD (red), and S, N-doped GQD (blue).

Figure 27 shows X-ray photoelectron spectroscopy (XPS) characterization of GQDs, including pristine GQD, S-doped GQD, and S, N-doped GQD. The atomic concentrations of C, and O in the pristine GQD were determined to be 47.2% (C), and 52.8% (O), respectively. In the S-doped GQD, the atomic concentrations were 41.8% (C), 50.0% (O), and 8.2% (S), which indicates that the new peak in S 2p region appeared and peak in C 1s significantly decreased. In addition, the atomic concentrations of S, N-doped GQD were calculated to be 42.7% (C), 47.1% (O), 4.9% (S), and 5.3% (N). The new peak in N 1s (5.3%) region appeared and C1s region was enlarged which is attributed to the formation of dimethylamino group. In Figure 27b-d, the deconvoluted C1s, S2p, N1s XPS spectra of S, N-doped GQD are presented. In the C1s region, the main peak at 284.6 eV corresponds to the graphite like sp2 carbon, indicating most of the carbon atoms are arranged in honeycomb lattice. In addition, the peak intensity of C-O or C-N or C-S bonding (peak II, 286.0 eV) significantly increased compared to that of pristine GQD, and S-doped GQD, which suggest the formation of C-N bonding. The high-resolution XPS spectra of S2p shows main two peaks at 168.4 and 169.6 eV and minor two peaks at 163.6, and 164.7 eV, which represents large portion of sulfone (168.4 eV) and sulfate (169.6 eV) group (Figure 27c). These results indicate that sulfuric acid was doped into the GQD to yield benzenesulfonic acid *via* electrophilic aromatic substitution

reaction with the benzene ring on the surface of GQD. The high-resolution XPS spectra of N1s from S, N-doped GQD can be deconvoluted into two peaks (Figure 27d). The peak at 399.9 eV is attributed to the N 1s of the N-C bond of amino alcohols, indicating that the decomposed dimethylamine is attached to the aromatic ring of the N-GQD. The strong peak at 401.6 eV is ascribed to the N-C bond of amide linkage, indicating that the dimethylamine was doped into the GQD by peptide bonding with the carboxylic acid group on the surface of GQD. Judging from these data, the preparation of S, N-doped GQD is successfully carried out.

To investigate the growth mechanism of GQD and doping level of S, N atoms, optical properties of GQDs were monitored during the carbonization process by recording the UV-visible absorption spectra of the sample aqueous solutions at different times in Figure 28a-c. Figure 28a shows the growth of two clear absorption bands of pristine GQD at 244 nm, and 330 nm until time reaches to 20 min and then decrease after 20 min, indicating the synthesized GQDs keep grow to graphene oxide(GO) at high carbonization degrees. The origins of these two peaks are related to π electron transition in oxygen-containing GQDs. The peak at 244 nm corresponds to $\pi \rightarrow \pi^*$ transition of the aromatic sp^2 domains. The other absorption peak at 330 nm is due to $n \rightarrow \pi^*$ transition of the C=O bond. [67]

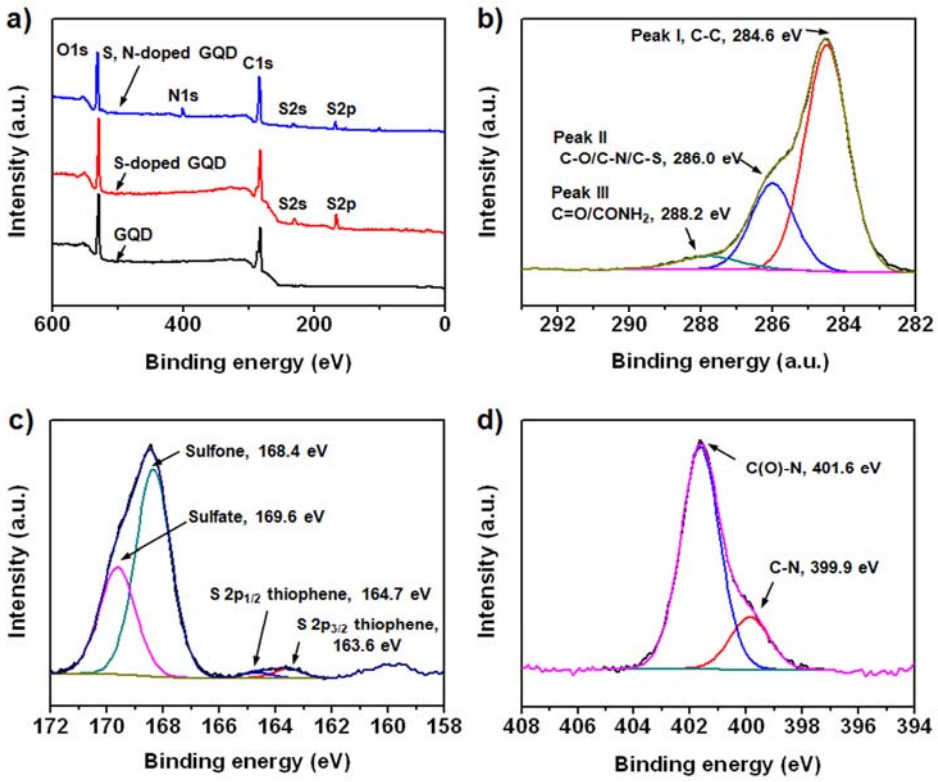

Figure 27. (a) XPS spectra of GQD, S-doped GQD, and S, N-doped GQD. The high resolution (b) C1s, (c) S2p, and (d) N1s peaks of the S, N-doped GQD.

In the case of S-doped GQD, three absorption bands appeared at 244 nm, 300 nm, and 365 nm in Figure 28b. The peak at 244 nm significantly enlarged in the condition of H_2SO_4, indicating that sulfuric acid act as acidic catalyst for facilitate aromatic sp^2 structure.[30] The peak at 300 nm is due to $n \rightarrow \pi^*$ transition of the C=O bond. The absorption band at 365 nm is related to the doping of sulfur, which alters the surface state of GQDs. The bands at 365 nm are attributed to the $\pi \rightarrow \pi^*$ of C─S. Following N-doping with the addition of DMF, the absorption bands of S, N-doped GQD appear at 300 nm, 365 nm and 527 nm in Figure 28c. The bands at 527 nm may be attributed to the $\pi \rightarrow \pi^*$, and $n \rightarrow \pi^*$ of C─N. Figure 28d shows the digital images of the color change of S, N-doped GQDs. As the reaction time increase, the color of S, N-doped GQD aqueous solution change from bright pink to dark yellow, indicates the formation of graphene oxide when high carbonization degrees.[88] The result reveals that the carbonization degree can affect the absorption properties of as-synthesized GQDs and that high carbonization degree leads to the growth of GO.[89]

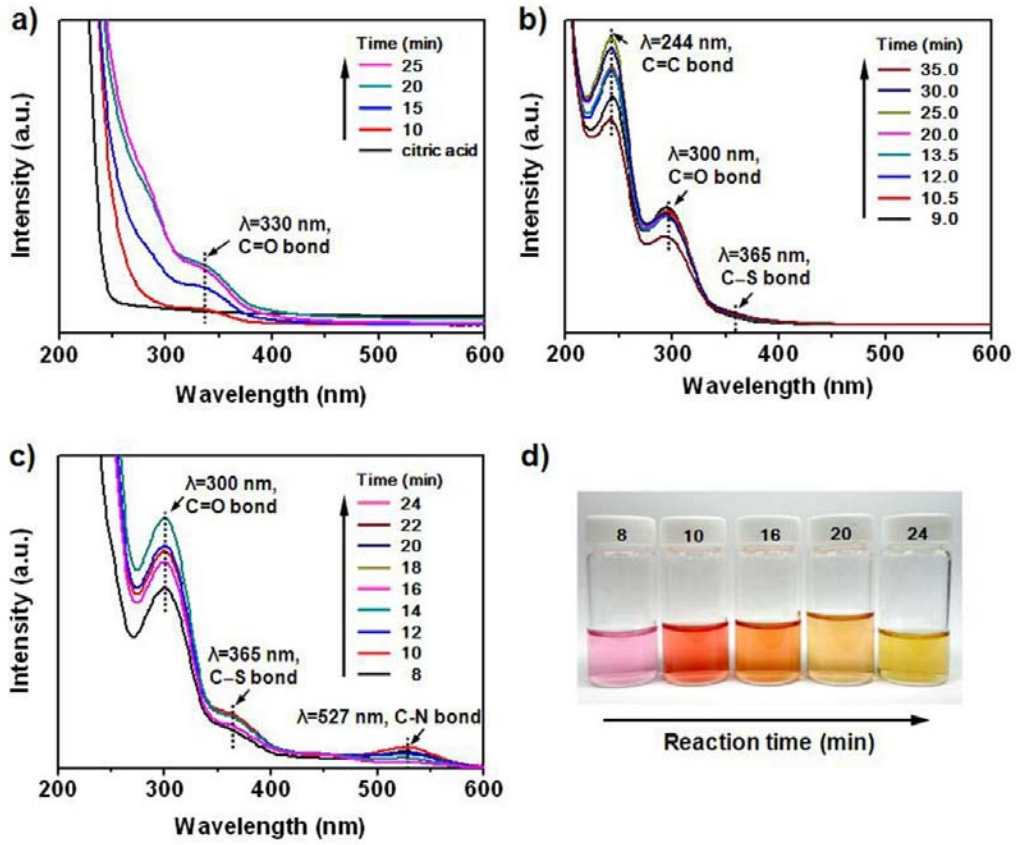

Figure 28. UV-vis absorption spectra of (a) pristine GQD, (b) S-doped GQD, and (c) S, N-doped GQD as a function of reaction time. (d) Optical images of diluted S, N-doped GQD aqueous solution.

Like most luminescent carbon nanoparticles, the S, N-doped GQD also exhibit an excitation-dependent PL behavior. When the excitation wavelength is changed from 350 nm to 450 nm, the emission maximum wavelength showed red-shift from 440 nm to 550 nm and gradual decrease of its intensity (Figure 29a). In general, the excitation-dependent PL behaviors of GQDs reflect the effect from particles of different surface states.[87] In addition, the fluorescence quantum yield (FLQY) of GQDs excited with 350 nm UV light was measured by selecting 4', 6-diamidino-2-phenylindole (DAPI) dissolved in dimethylsulfoxide as a standard in Figure 29b. The FLQY of GQD, S-doped GQD, and S, N-doped GQD were measured to 9%, 41%, and 61%, respectively (Table 2). It is notable that the FLQY of S, N-doped GQD is *ca*. 7 times higher than that of pristine GQD. In principle, the FL of the GQDs should be attributed to the radiative recombination of electrons and holes trapped on the GQDs surface. Pristine GQDs have different kinds of surface states (O-states) corresponding to a relatively wide distribution of different energy levels to generate a broad UV/Vis absorption band and broad and excitation-dependent emission spectra.[36] After doping of S, N atoms, it seems that the doped sulfur and nitrogen atoms introduce a new kind of surface state such as S-states and N-states. Therefore, electrons trapped by the new formed surface states could facilitate a high yield of radiative recombination.

From the above results, the strong FL emission of the S, N-doped GQDs mainly result from the surface-doped sulfur and nitrogen atoms.

The luminescence decay profiles of the blue GQDs are shown in Figure 30. The decay was recorded for the GQDs transitions at 350 nm excitation measured at room temperature by a timecorrelated single photon counting technique. The lifetime data of three types of GQDs were very well fitted to a double-exponential function as shown in Figure 30. The parameters generated from iterative reconvolution of the decay with the instrument response function (IRF) are listed in the inset of Figures 30, respectively. The observed lifetimes of the S, N-doped GQD are τ_1 = 2.17 ns, and τ_2 = 0.15 ns, whereas for pristine GQDs lifetime τ_1 = 0.19 ns, and τ_2 = 1.15 ns were observed. The observed lifetime of GQDs in nanosecond suggests that the synthesized S, N-doped GQDs are most suitable for optoelectronic and biological applications. Importantly, a gram-scale GQD production was readily obtained in a single carbonization reaction (Figure 31). The photograph shows *ca*. 2 g of three types of GQD; pristine GQD, S-doped GQD, and S, N-doped GQD, which is a very large quantity for a laboratory-scale production. The color of GQD changed from bright yellow to black after S, N-doping process, indicating sulfur and nitrogen atoms are incorporated into the pristine GQD.

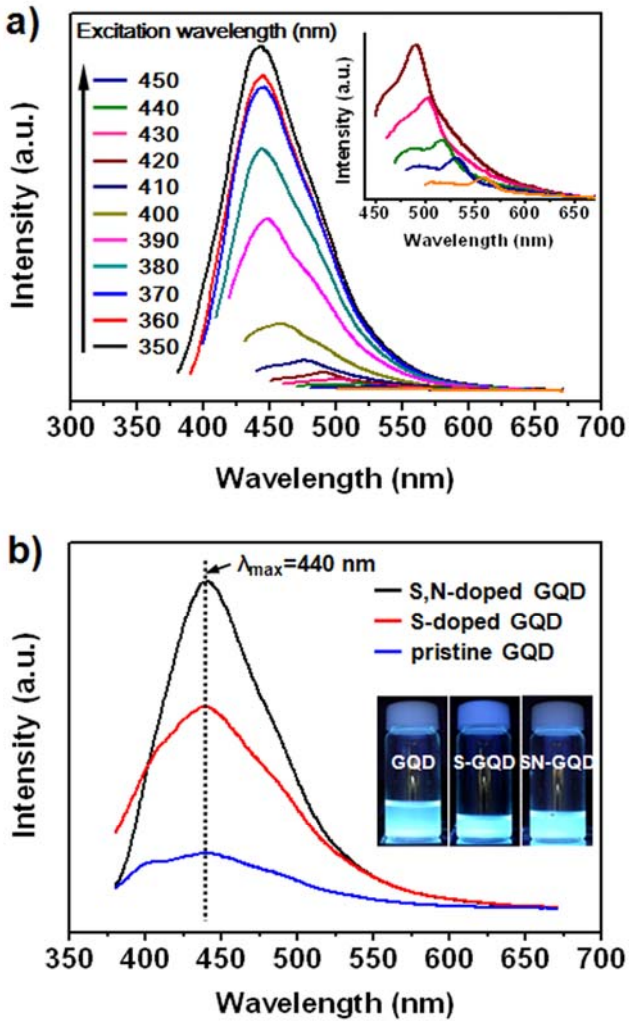

Figure 29. (a) Fluorescence spectra of S, N-doped GQD under different excitation wavelengths from 350 to 460 nm. The insets are magnified FL spectra of S, N-doped GQD under different excitation wavelengths from 420 nm to 460 m. (b) Fluorescence spectra of pristine GQD, S-doped GQD, and S, N-doped GQD under 350 nm. The insets are the optical images of GQD, S-doped GQD, and S, N-doped GQD excited under 350 nm illumination.

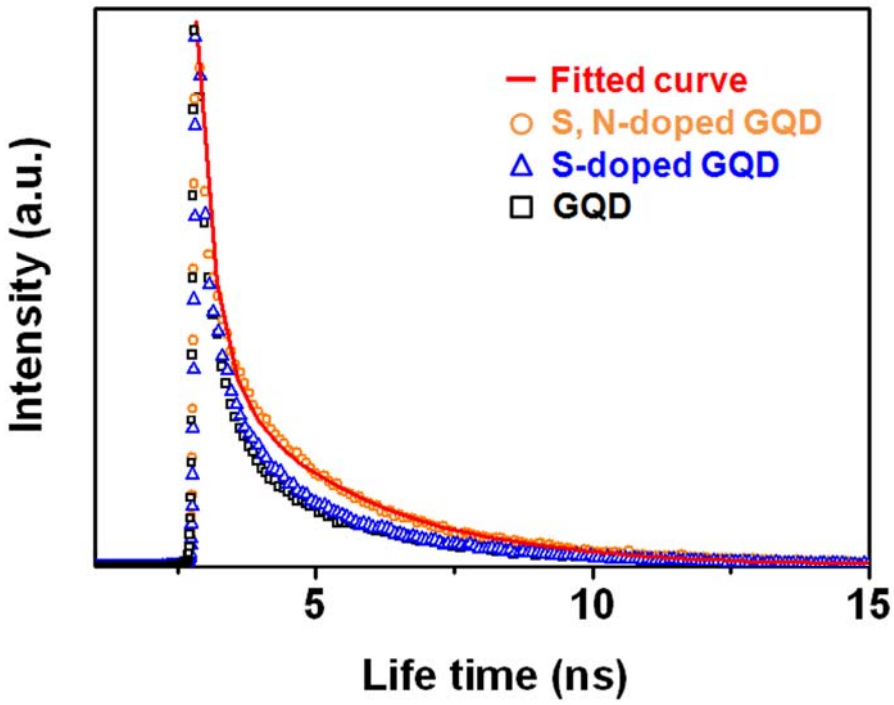

Figure 30. The transient PL measurements of pristine GQD, S-doped GQD, and S, N-doped GQD. The red line shows the lifetime curve fitted by two-exponential function.

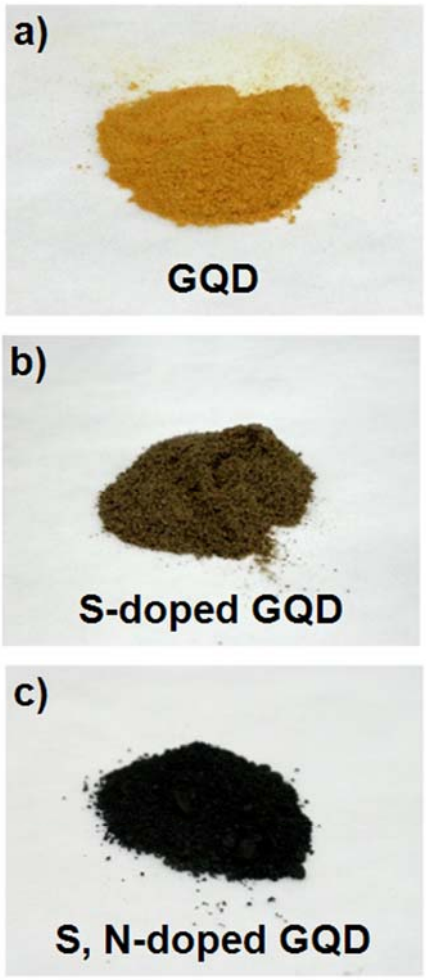

Figure 31. Digital photographs showing *ca.* 2 g of (d) pristine GQD (e) S-doped GQD, (f) S, N-doped GQD obtained in a single carbonization reaction.

Table 2. Fluorescence quantum yields of GQD, S-doped GQD, and S, N-doped GQD.

Samples	**Fluorescence quantum yield[1] (%)**
GQD	9.0
S-doped GQD	41.4
S, N-doped GQD	61.1

[1] The fluorescence quantum yield of GQDs excited with 350 nm UV light is calculated by selecting the DAPI (4',6-diamidino-2-phenylindole) as standard.

3.3. Applications

3.3.1. FRET-based dye-sensitized solar cells for near-infrared light harvesting.

The as-synthesized GQDs could be applied as fluorescent phosphors in FRET-based photovoltaic devices.[90] The overall cell structure and the arrangement of TiO_2 nanoparticles, GQDs, and dye inside the cell are shown in Figure 32a. In principle, when solar light impinges on the photoanode of DSSC, the GQDs serve as "antennae" and funnel the absorbed energy to nearby dye molecules by means of FRET, rather than being used directly as sensitizers.[91] Therefore, more electron charges can be generated and difused into the TiO_2 films through FRET.[92] Figure 32b shows the energy-level diagram describing the upconverted fluorescence emission from a GQD under infrared excitation. In general, GQDs possessed characteristic upconvesion PL properties. Upconversion refers to a nonlinear optical process characterized by the successive absorption of two or more photons followed by the emission of radiation at a shorter wavelength than the excitation wavelength.[93] The upconversion PL properities of GQDs are attributable to multiphoton active processes, similar to previous reports on carbon dots.[20] Thus, a greater amount of light can be utilized by the D719 dye *via* the upconversion fuction of the GQDs and FRET. [94, 95]

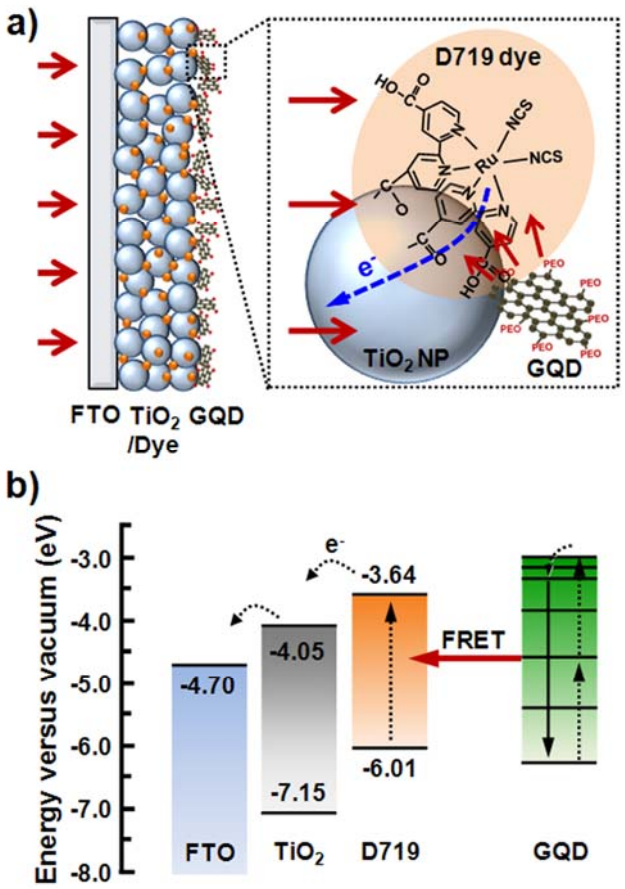

Figure 32. (a) Schematic image of GQD-layer-modified DSSC and light harvesting mechanism *via* FRET. (b) Energy level diagram of GQD-layer-modified DSSC.

To enhance the PL intensities of GQDs, the GQD was surface passivated by anchoring the surface edges of GQDs with polyethylene glycol (PEG, MW: 10,000).[96] The anchoring process was performed at 120°C for 1 h *via* a hydrothermal method. Figure 33 demonstrates that the TEM image of GQDs before and after the PEG-passivation. After PEG-passivation, the size of GQDs was increased from 5 nm to 7 nm. The dotted circles show the lattice structures of GQDs, indicating the rest of circles are PEG molecules. Namely, it was exhibited that the thickness of PEG was in the range of 1-2 nm on the surface of GQDs.

Figure 34 shows FT-IR spectra of GQDs and PEG-passivated GQDs. The FT-IR spectrum of the GQDs show characteristic C–H deformation peak at 835 cm^{-1}, C–O stretching at 1100 cm^{-1}, C=C aromatic stretching at 1637 cm^{-1}, and C=O stretching at 1785 cm^{-1}, indicating the successful synthesis of GQDs. Following surface passivation with PEG (PEG-GQD), the peaks related to C–H and C–O bond increased in intensity, including the C-H deformation at 950 cm^{-1}, C-O-C stretching at 1100 cm^{-1}, and C-H stretching at 2884 cm^{-1}.

Figure 35 demonstrates the PL spectra of pristine GQD and PEG-passivated GQD. After PEG-passivation of GQDs, the PL intensity of PEG-GQD increases *ca.* 12 times compared to the pristine GQDs, and peak maximum blue-shifted about 30 nm. This peak shift is attributable to the size

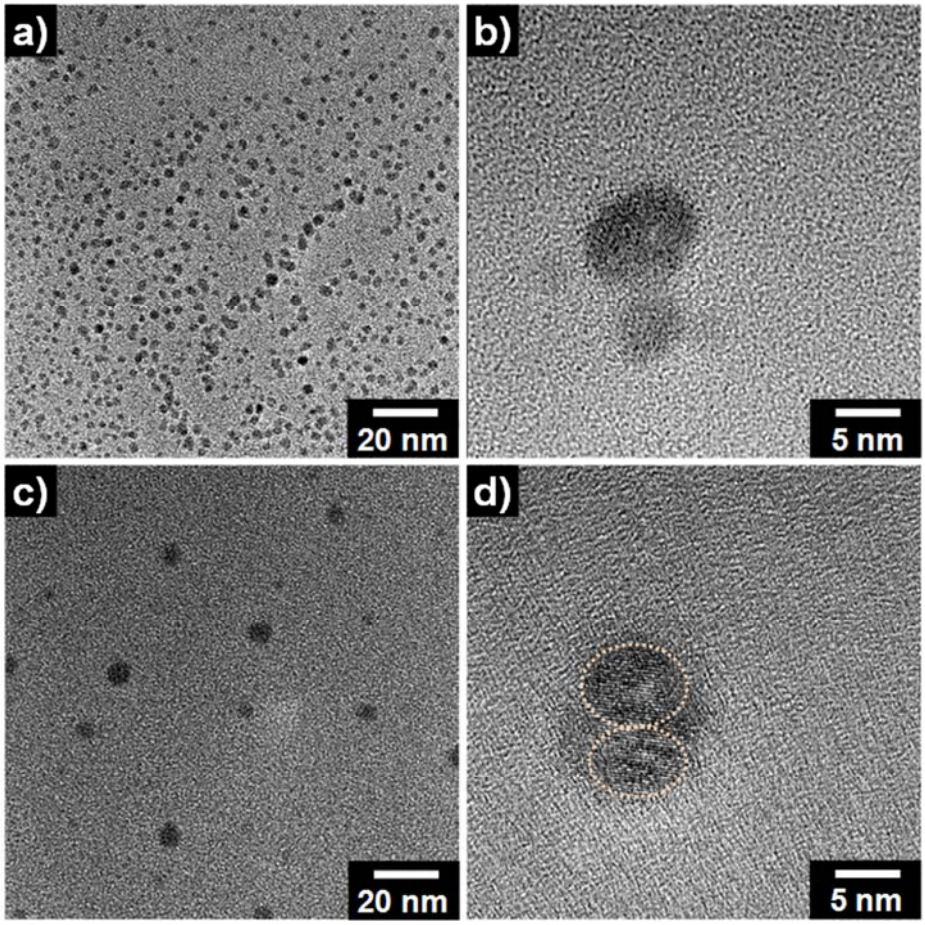

Figure 33. The low-and high-magnification of TEM images of (a-b) pristine GQD (c-d) PEG-passivated GQD.

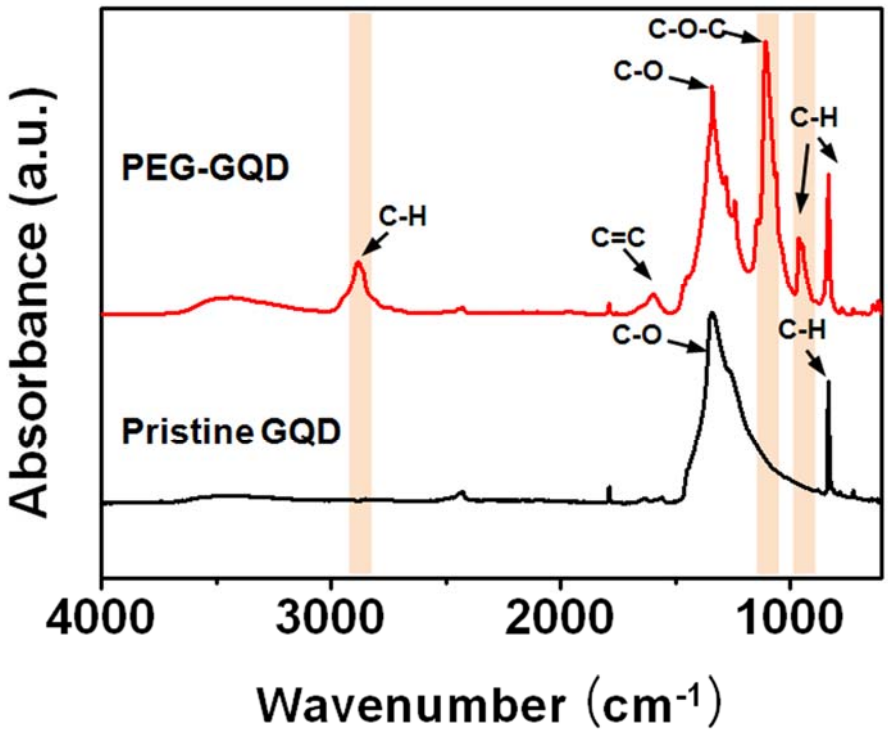

Figure 34. Fourier-transform infrared (FT-IR) spectra of pristine GQDs and PEG-passivated GQDs.

decrease of GQDs during the hydrothermal process at PEG anchoring step.

To further explore the upconversion fluorescence properties of as-synthesized GQDs, a detailed PL study was carried out using different excitation wavelength. As shown in Figure 36, when the excitation wavelength changed from 600 to 750 nm, an upconversion emission band was observed in the curve centered at *ca.* 525 nm. The upconversion PL property of GQDs is attributable to multiphoton active processes, similar to previous reports on carbon dots.[20]

Figure 37 shows the absorption spectrum of dye and the emission specra of differently sized GQDs. These GQDs showed strong emission bands at 435 nm (120 °C), and 500 nm (80 °C), respectively. These emission characteristics are well-corresponded to the PL results in Figure 21. In addition, an aquesous solution odf D719 dye had two main absorption peaks at 380 and 540 nm. In principle for efficient FRET, the emission spectrum of the donor (GQDs) must overlap with the absorption spectrum of the acceptor (dye). Therefore, 80 °C-oxidized GQDs have better spectral overlap with D719 dye than 120 °C-oxidized GQDs, indicating the more efficient FRET design between donor and acceptor.

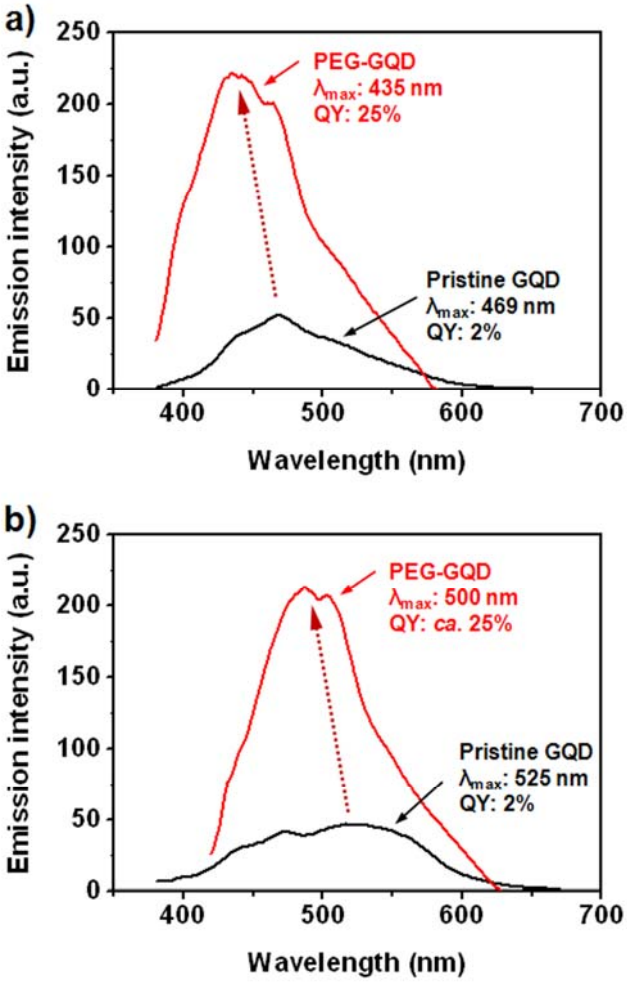

Figure 35. PL spectra of (a) 120 °C- and (b) 80 °C-oxidized GQD before and after PEG passivation. (The insets indicate the corresponding fluorescence quantum yield of GQDs)

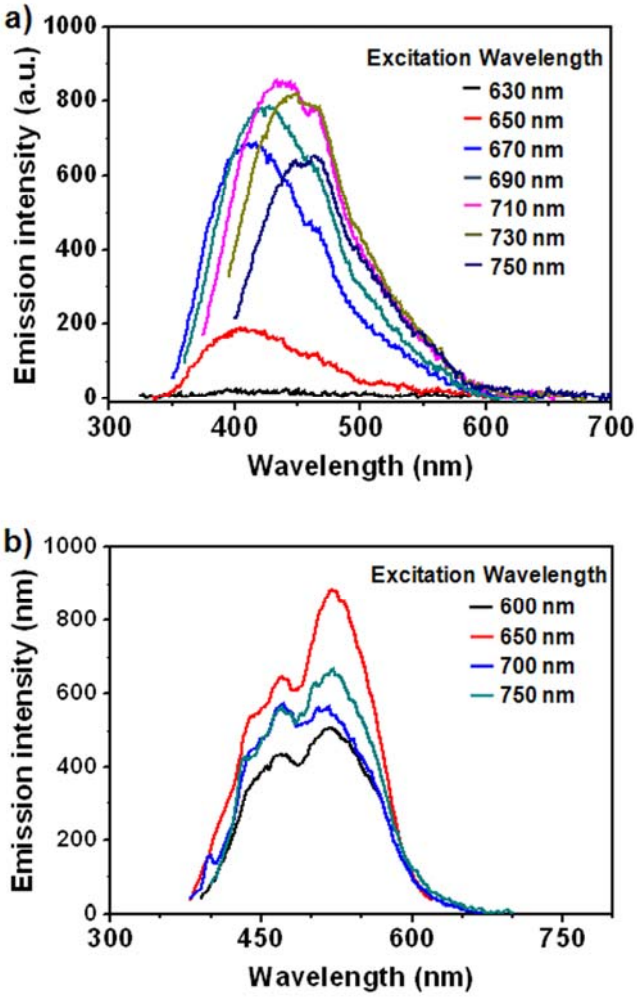

Figure 36. Upconverted PL spectra of the (a) 120 °C- and (b) 80 °C-oxidized GQDs at different excitation wavelengths from 600 nm to 750 nm.

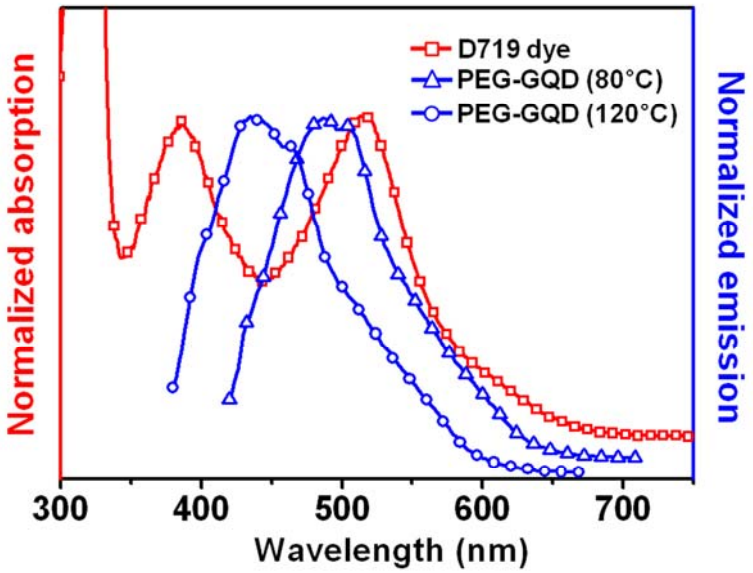

Figure 37. Absorption (left) of D719 dye and emission (right) of GQDs; 80°C-, and 120°C-oxidized GQDs. Emission spectra upon excitation at 350 nm with emission maxima normalized at their intensities.

In our initial assays, we focused on a FRET system compsed of D719 dye with differently sized GQDs. To test the energy transfer between the GQDs and the sensitizing D719 dye, the PL spectra of a mixture of GQDs and D719 dye in aqueous solution were obtained (Figure 38a-b). In the PL analysis of GQD+dye combinations, it was observed that the intensity of the emission spectrum significantly decreased after the addition of dye to the GQDs. In particular, the PL quenching was greater for 80 °C-GQDs followed compared to that of 120 °C, which meant that a larger degree of luminescence of 80 °C GQDs was absorbed into the dye in the 80 °C GQD+dye combination.[97]

Additionally, the Stern–Volmer plot of the fluorescence quenching of GQD with an emission peak at 350 nm were investigated with compared with those of other light emitting GQDs (80 °C and 120 °C) in Figure 38c.[98] Compared to the 120 °C-GQD, the 80 °C-GQD indicated a high quenching rate with the content of D719 dye. These results are corresponding to a larger degree of overlap between the donor fluorescence spectrum and the acceptor absorbance spectrum, as shown in Figure 37.[99] Thus, a greater amount of light can be utilized by the D719 dye *via* the upconversion function of the GQDs and Förster resonance energy transfer (FRET).[94, 95] On the basis of these data, energy transfer from GQD donors to D719 dye acceptors is the dominant mechanism of the fluorescence quenching. The absorption spectra for the GQD

were recorded before and after the addition of D719 dye in Figure 38d. The absorption spectrum of dye+GQDs indicated increased absorption intensity in the wavelength range from 350 to 700 nm after the addition of dye to the GQDs. In particular the absorption of dye+GQDs showed a remarkable increase around 450 nm and above 600 nm relative to the pristine dye. This signified the high utilization of the solar spectrum area that dyes alone are not able to utilize sufficiently.[100] In general, the efficiency of energy transfer by FRET is given by the equation (2),[101]

$$\varphi_{ET} = \frac{k_{ET}}{k_{ET} + \frac{1}{\tau_D} + k_w} \tag{2}$$

Where k_{ET} is the rate of energy transfer from donor to acceptor, τ_D is the excited state lifetime of the donor in the absence of the acceptor, and k_w is the effective rate of any other competing process.[98] The rate of Förster energy transfer for two dipoles separated a distance r is

$$k_{ET}(r) = \frac{1}{\tau_D}\left(\frac{R_0}{r}\right)^6 \tag{3}$$

R_0 is given by the well-known expression for the Förster radius: [90]

$$R_0^6 = \frac{9000 \ln(10) \kappa^2 \cdot \Phi_D}{128 \pi^5 N_A n^4} \left[\int_0^\infty F_D(\nu) \varepsilon_A(\nu) \nu^{-4} d\nu\right] \tag{4}$$

Where n is the refractive index, N_A is the Avogadro number, k is the dipole orientation factor, and Φ_D is the donor fluorescence quantum yield in the absence of acceptor.[92] The terms within the square brackets constitute the spectral overlap integral J of the donor fluorescence intensity (normalized to unit area) and the absorption spectrum of the acceptor. For our photoanode, we employed differently sized GQDs into the nanoporous TiO_2 film *via* a spin-coating method.

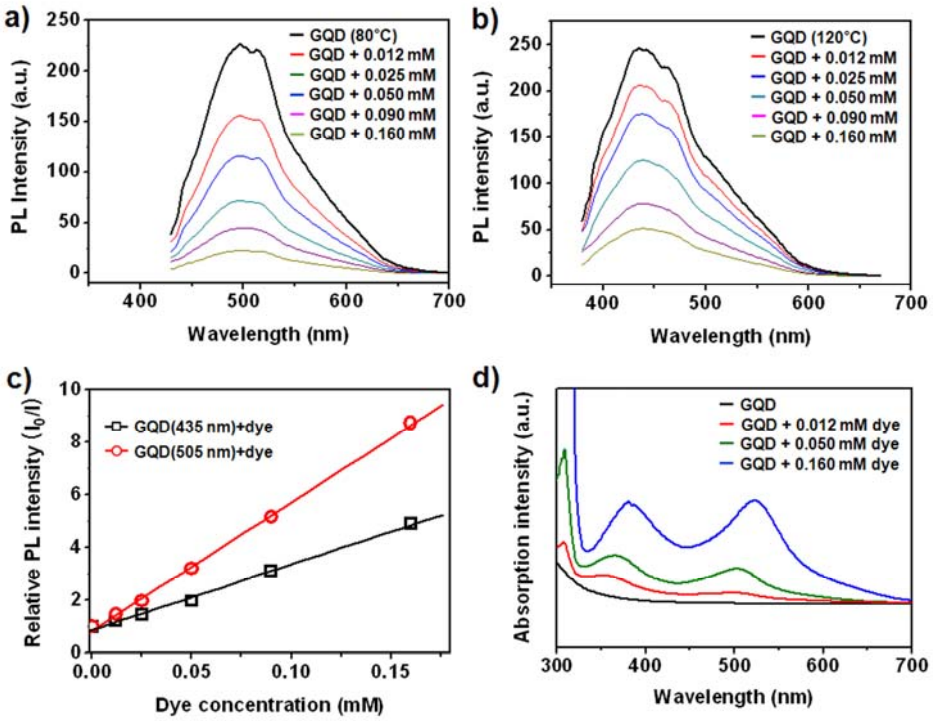

Figure 38. PL quenching of (a) GQDs (80 °C) and (b) GQDs (120 °C) as a function of the amount of dye molecules from 12 to 160 μM. (c) Stern-Volmer plot of the fluorescence quenching of GQDs (80, 120 °C) with D719 dye. (d) Absorption spectra of GQDs (80 °C) as a function of the amount of dye molecules from 12 to 160 μM.

For use as light-harvesting antennae in FRET based photovoltaic devices, GQDs were deposited onto the top of a TiO_2 working electrode of DSSCs *via* spin coating.[92, 100] The photovoltaic performance (PV) of GQD-layer-modified DSSCs is shown in Figure 39. When 2.6 mg of GQDs were incorporated into the DSSC, the power-conversion efficiency was enhanced to 7.95%, compared to 7.28% for pristine DSSC. Notably, the optimized GQD-layer-modified DSSC showed *ca.* 9.2% enhanced efficiency compared with pristine DSSC. Figure 39b shows the incident photon-to-current efficiency (IPCE) for DSSCs with and without GQDs. For the cells with GQDs, the response for wavelengths between 350 and 700 nm increased significantly compared with pristine DSSC. The IPCE changed significantly for wavelengths less than 530 nm, corresponding to the overlap region of the donor emission spectrum and the acceptor absorption spectrum. Moreover, the high-wavelength bands at 850 nm increased with the addition of GQDs, which could be attributable to the upconverted PL of GQDs (Figure 39b, inset).[102, 103] Thus, the GQD-layer-modified photoanode provided enhanced DSSC performance and offers new possibilities for realizing FRET based DSSCs for a wide range of wavelengths by incorporating GQDs.

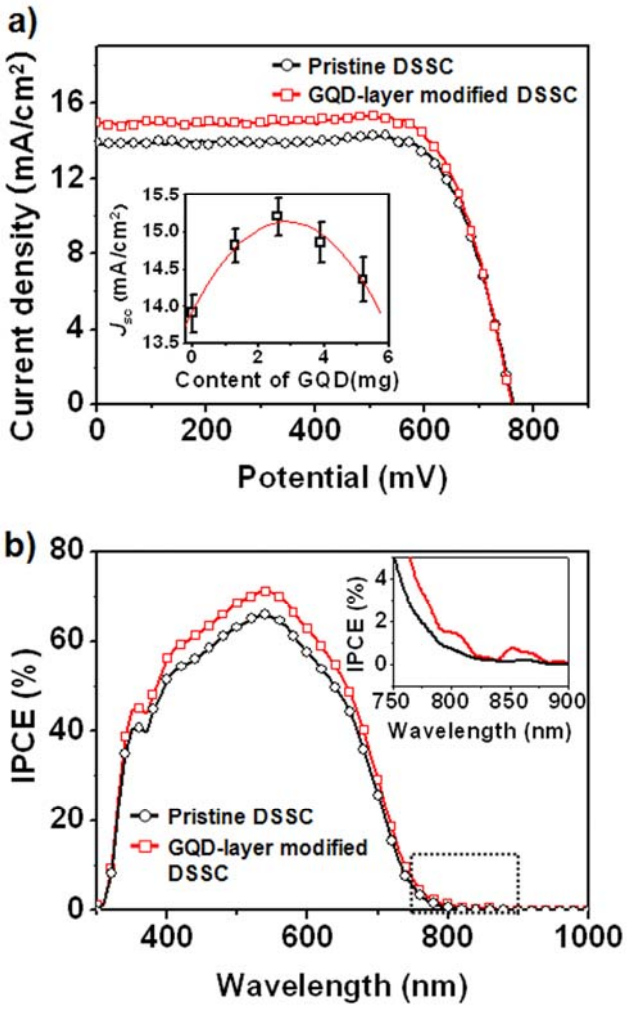

Figure 39. (a) *J-V* characteristics (under simulated AM 1.5 irradiation) of the cells with and without the use of GQDs. (inset: the photocurrent density as a function of the amount of deposited GQDs) (b) IPCE of the cells with and without the use of GQDs. (inset: high magnification spectra in IPCE).

Table 3 demonstrates the summary of photovoltaic performance of GQD-layer modified DSSCs with the content of GQDs. Although no significant trends in open-circuit voltage (V_{oc}) and fill factor (FF) were observed, the circuit density (J_{sc}) of GQD-layer modified DSSC was significantly higher than that of the pristine DSSCs. The higher J_{sc} of GQD-layer modified DSSC than the pristine DSSC is attributable to the enhanced ability of the GQD-layer modified photoanode to harvest light by means of FRET. In addition, the J_{sc} increased as the GQD content increased to 2.6 mg, and J_{sc} decreased with greater GQD content. The decrease in J_{sc} can be explained by the formation of a PEG layer on top of the TiO_2/dye layer, which inhibited contact between the electrolyte and the dye in Figure 42. Therefore, a greater amount of GQDs decreased J_{sc} significantly. When 2.6 mg of GQDs were incorporated into the DSSCs, the power-conversion efficiency was enhanced to 7.95%, compared to 7.28% for pristine DSSCs.

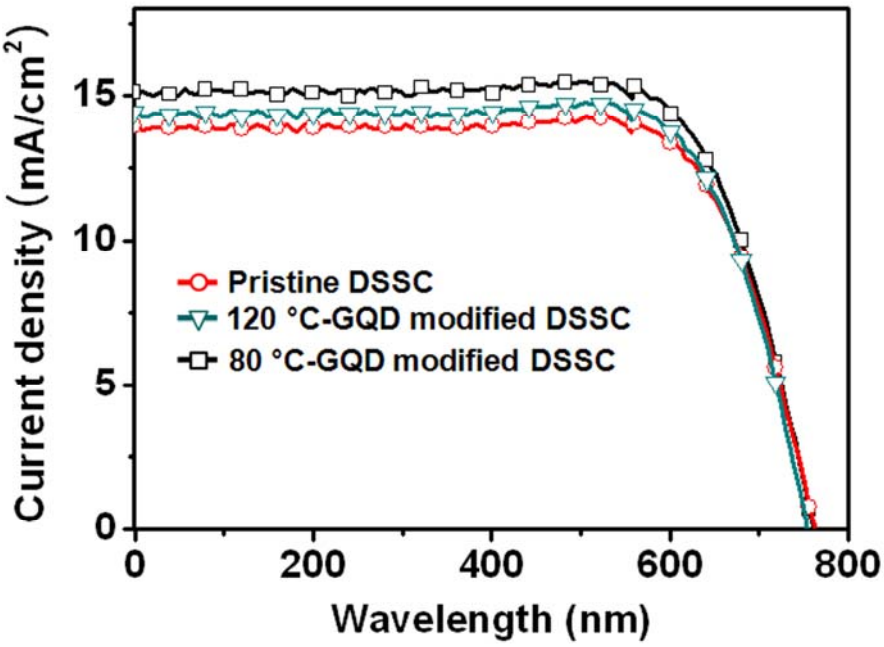

Figure 40. *J-V* curves of GQDs-modified DSSC with different types of GQDs. (80 °C, and 120 °C-oxidized GQDs)

Table 3. Summary of photovoltaic performance of TiO_2/dye/GQD cells as a function of GQD (80 °C) content from 1.3 to 5.2 mg

Sample [a]	**GQDs (mg)**	J_{sc} [b] **(mA cm^{-2})**	V_{oc} [c] **(mV)**	***FF*** [d]	η [e] **(%)**
Pristine DSSC	-	13.90	765	0.75	7.28
TiO_2/dye/GQDs cell	1.3	14.81	765	0.75	7.75
TiO_2/dye/GQDs cell	2.6	15.20	766	0.75	7.95
TiO_2/dye/GQDs cell	3.9	14.85	764	0.74	7.76
TiO_2/dye/GQDs cell	5.2	14.35	764	0.74	7.49

[a] The content of deposited GQD was varied from 0 to 5.2 mg *via* the number of spincoating . Active area of the assembled DSSC is 0.25 cm^2. [b] Short-circuit current. [c] Open-circuit voltage. [d] Fill factor. [e] Power conversion efficiency.

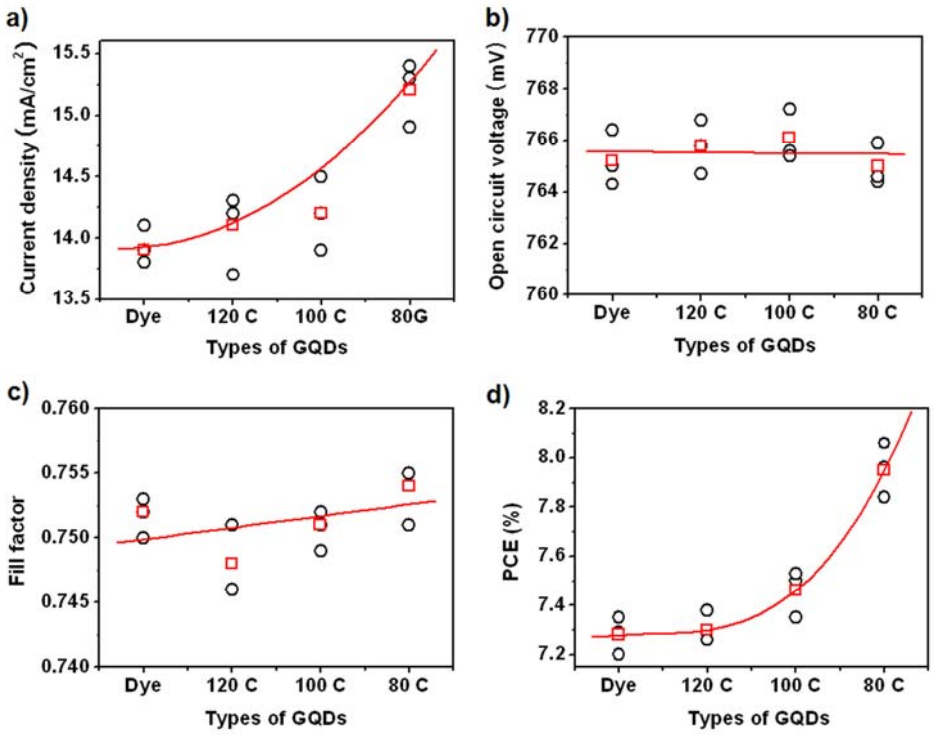

Figure 41. Photovoltaic-characteristics relationship with GQD types of GQD-layer modified DSSCs: (a) J_{sc}, (b) V_{oc}, (c) FF and (d) power conversion efficiency. The deposited amount of GQDs was fixed to 2.6 mg for GQD-modified layer.

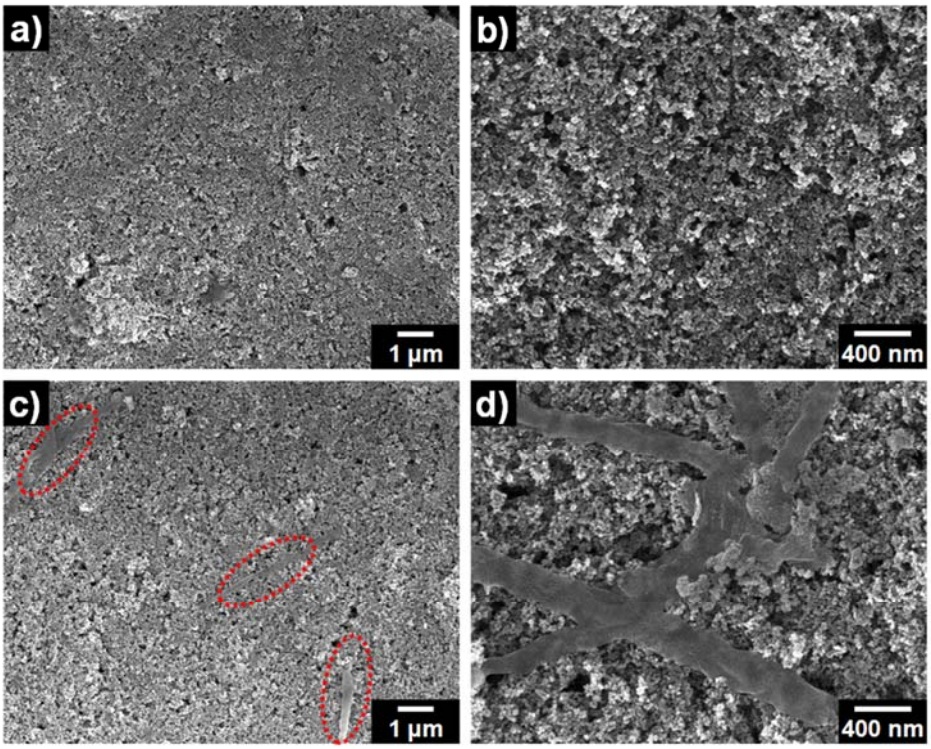

Figure 42. Top-view scanning electron microscope (SEM) images of the FTO/TiO_2/GQD electrodes; (a-b) 2.6 mg of GQDs, and (c-d) 10.0 mg of GQDs. (The red-dotted circles indicate PEG molecules)

3.3.2. Graphene quantum dot-based fluoresent Sensor for rapid and ultrasensitive detection of an anthrax biomarker.

The as-synthesized GQD was modified by hybridization with Eu^{III}-macromolecule complex and applied as dual emission fluorescent sensor for *Bacillus anthracis* spore detection. The fabrication of a Eu-based fluorescence GQD sensor and detection mechanism of dipicolinic acid (DPA) is outlined in Figure 43. Initially, pristine blue photoluminescent GQDs were fabricated *via* an excessive oxidation and size-selective precipitation approach, as described in Ref 21.[21] To graft the europium sensing moiety onto the GQDs, ethylenediamine (EDA) was covalently bonded onto the GQDs to form NH_2-GQDs. Ethylenediamine tetraacetic acid dianhydride (EDTA) was then introduced onto the GQDs, leading to a reaction between the amino groups and the anhydride groups. The resulting EDTA ligand on the GQD was then converted into a [GQD(EDTA)(Eu)–$(H_2O)_3$] complex *via* reaction with $EuCl_3$ (Eu-GQD). Upon exposure of the Eu-GQD sensor to DPA, water molecules were excluded from the Eu^{III} coordination sphere through the formation of a [GQD(EDTA)(Eu)–(DPA)] complex, which significantly minimized the non-radiative quenching of the Eu^{III} emission.[104] This resulted in an increase in the overall quantum yield of Eu^{III} and thereby a corresponding improvement in the sensitivity towards DPA. There was a clear red fluorescent enhancement of

Eu-GQDs following the addition of DPA, which was readily visible to the naked eye under a UV lamp.

Figure 44 shows transmission electron microscopy (TEM) data confirming the formation of GQDs. The average diameters of the two sets of GQDs were controlled to 3 and 10 nm by acidic oxidation temperature and the both of GQDs were monodisperse in the aqueous solution. In addition, the formation of GQD, NH_2-GQD, and Eu-GQD was confirmed using both Fourier-transform infrared (FT-IR) spectroscopy and X-ray photoelectron spectroscopy (XPS), as shown in Figure 45a–d. The FT-IR spectrum of the GQDs shows characteristic C–H deformation peaks at 835 cm^{-1}, C–O–C stretching peaks 1236 cm^{-1}, C–O stretching peaks at 1360 cm^{-1}, and C=C aromatic stretching peaks at 1591 cm^{-1}, indicating the successful synthesis of GQDs. Following amine functionalization with EDA (NH_2-GQD), the peaks related to amines increased in intensity, including the N–H bending mode at 640 nm^{-1} and C–N stretching modes at 1167 cm^{-1} and 1255 cm^{-1}. The Eu-GQDs exhibited new peaks due to carboxylic acid groups at 1312 cm^{-1} and 1584 cm^{-1}, and N–H stretching modes at 3185 cm^{-1} appeared due to formation of the [GQD(EDTA)(Eu)] complex.[105]

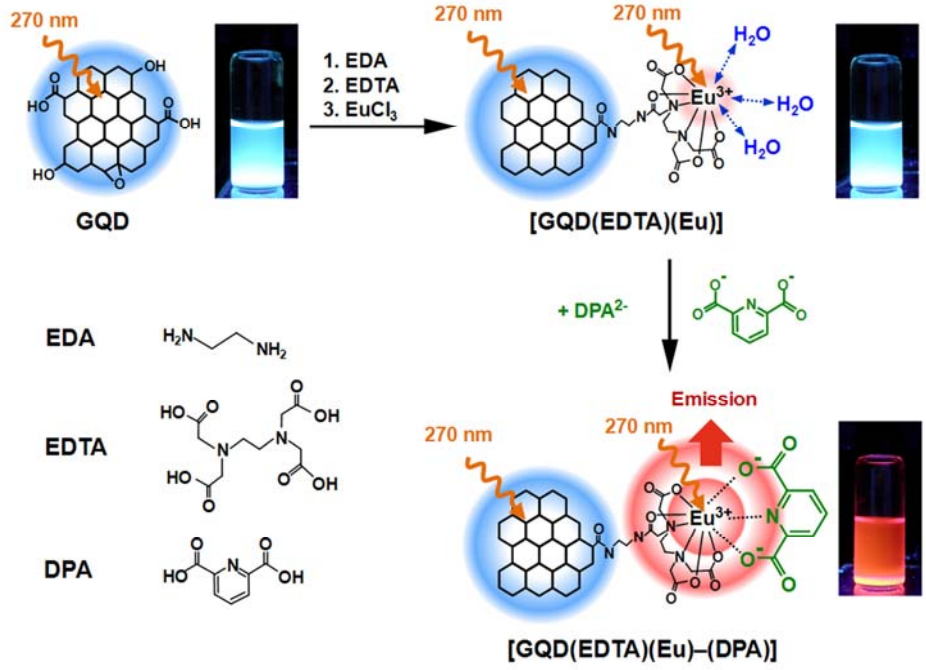

Figure 43. Schematic diagram showing the fabrication process of Europium modified GQD and their sensing mechanism with DPA. The inset shows the visual fluorescent color change of each sensor under UV irradiation.

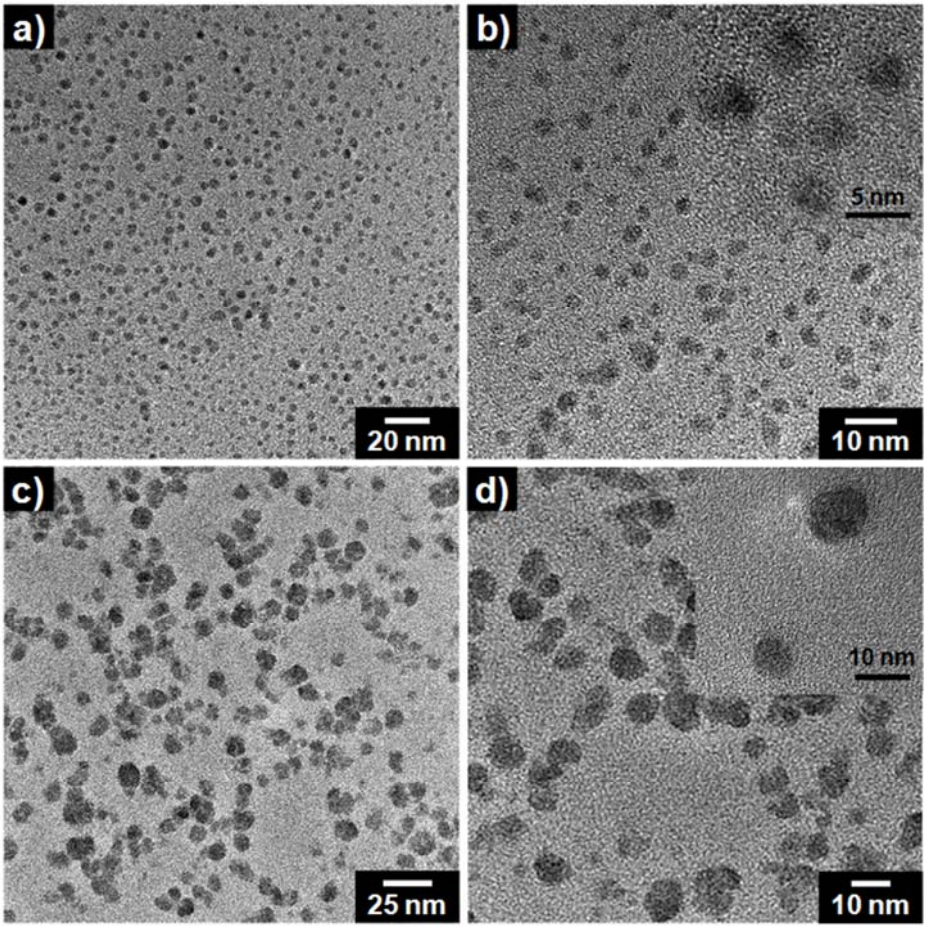

Figure 44. TEM images of GQDs prepared *via* excessive oxidation and size-selective precipitation. (a–b) 3-nm-diameter GQDs and (c–d) 10-nm-diameter GQDs. (insets: corresponding HR-TEM images of GQDs).

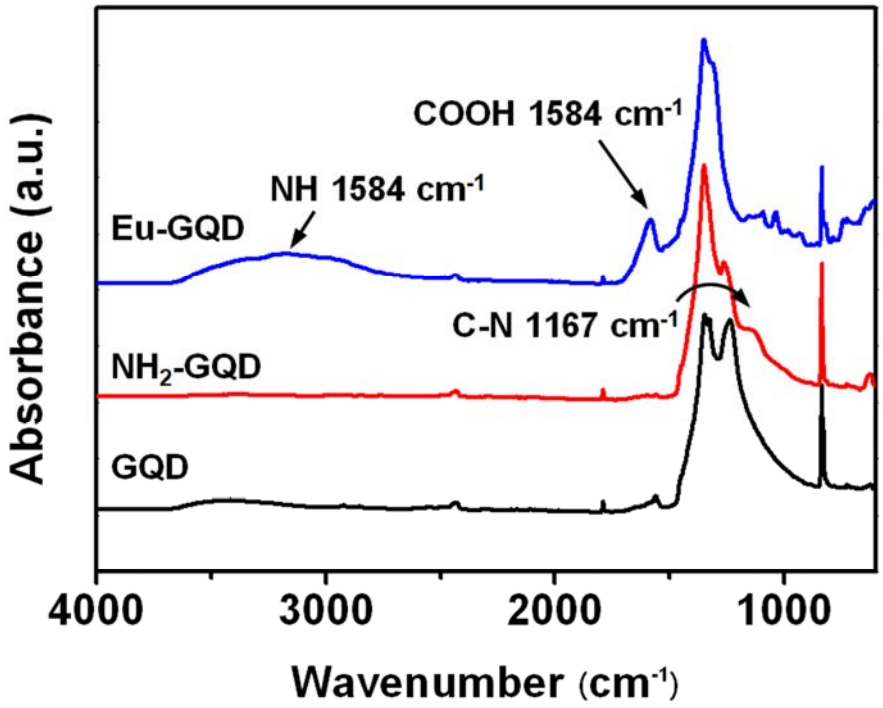

Figure 45. (a) FT-IR spectra of GQDs (black line), NH_2-GQD (red line), and Eu-GQD (blue line).

Figure 46 shows XPS characterization of GQDs, including surface-modified NH_2-GQDs and Eu-GQDs. The atomic concentrations of C, N, and O in the GQDs were determined to be 54.78%, 0.12%, and 45.10%, respectively (Table S2). In the NH_2-GQDs, the atomic concentrations were 52.08%(C), 2.64%(N), and 45.28%(O), which indicates that the N 1s region was enlarged. Additionally, the Eu 4d (4.12%) region appeared and the O (50.79%) region increased in the Eu-GQDs, which is attributed to the formation of [GQD(EDTA)(Eu)] complexes. The deconvoluted C1s XPS spectrums of GQDs, NH_2-GQDs, and Eu-GQDs are presented in Figure 46c-d. The main peaks of GQD at 284.6 eV (peak I) corresponds to the graphite-like sp^2 carbon, indicating most of the carbon atoms are arranged in honeycomb lattice. In addition, the small peaks of GQD can be attributed to C−O or C−N (peak II, 286.0 eV), −COOR or C−N (peak III, 288.2 eV), and CO_3^{2-} (peak IV, 290.2 eV), respectively. After the EDA treatment (NH_2-GQD), the intensity of peak II and III significantly increased, indicating successful amine functionalization of GQD. In the case of Eu-GQD, peak intensity of C−O or C−N bonding (peak II) significantly increased. The high-resolution XPS spectrum reveals the Eu 4d region with Eu $4d_{3/2}$ peaks: Eu^{2+} for Eu $4d_{5/2}$ (128.2 eV); Eu^{3+} for Eu $4d_{5/2}$(136.3 eV) and Eu $4d_{3/2}$(142.1 eV). The peaks are shown double-peak structure of each spin-orbit split component (j = 5/2 and 3/2), where peak and

satellite show a comparable intensity, are typical for oxygen-rich Eu(III) species. Judging from these data, the preparation of Eu-GQD is successfully carried out.

To demonstrate the operating principle of the Eu-GQD fluorescence sensors, the response of the dual-emission fluorescent probe towards DPA was measured in the presence of a 1-μM solution of DPA, and representative data are shown in Figure 47a. The 3-nm-diameter Eu-GQD probe showed three emission bands, centered at 435 nm, 593 nm, and 616 nm, which are ascribed to the emission from the blue GQD (435 nm) and red [(Eu)–(DPA)] complex (593 nm and 616 nm).[106] The two peaks in the 600-nm region are attributed to the formation of the [(Eu)–(DPA)] complex, specifically the transition of the Eu^{3+} excited states $^5D_0 \rightarrow {}^7F_J$ (J = 0, 1, and 2).[107] For the 10-nm-diameter Eu-GQDs, the emission peak red-shifted to *ca.* 540 nm; this is consistent with a decrease in the band gap of the GQDs as the size increases.[39] The attachment of DPA to the Eu ions reduced the non-radiative quenching of the Eu^{3+} emission, resulting in an increase in the quantum yield and a corresponding enhancement of the detection sensitivity for DPA.[108]

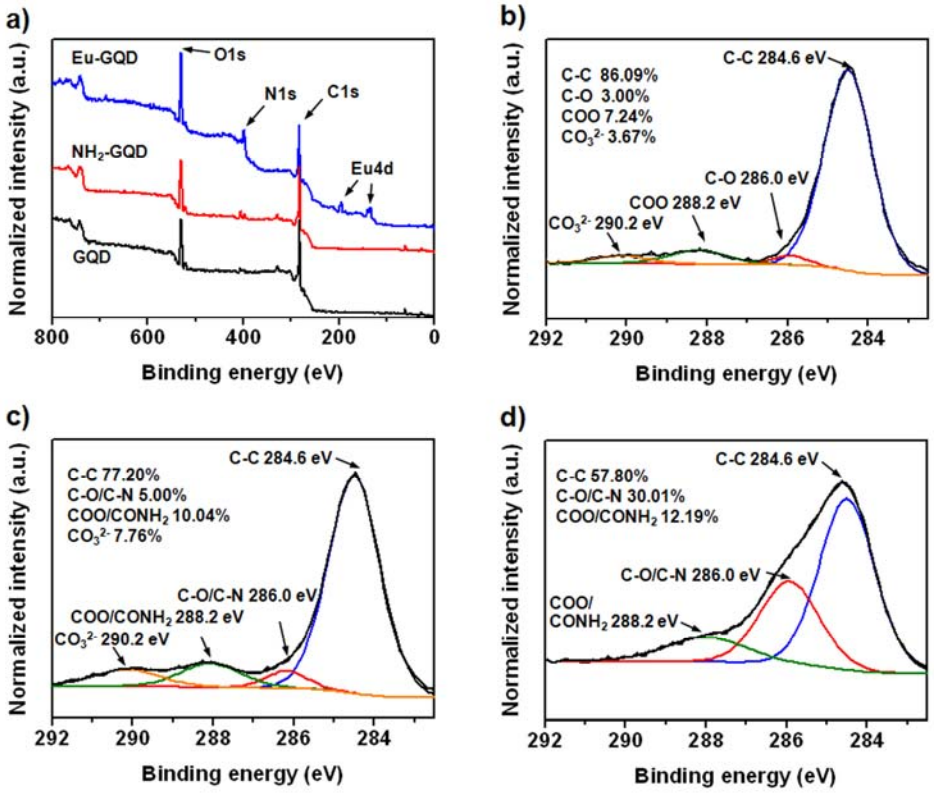

Figure 46. (a) X-ray photoemission spectroscopy (XPS) spectra of GQDs (black line), NH_2-GQDs (red line), and Eu-GQDs (blue line). (b) Curve fit of the C 1s peak of GQD. (c) Curve fit of the C 1s peak of NH_2-GQD. (d) Curve fit of the C 1s peak of Eu-GQD.

In Figure 47b, the time-dependent fluorescence response of the 3-nm- and 10-nm-diameter Eu-GQDs to a 10-μM DPA solution was monitored at 616 nm, using excitation at 270 nm.[109] Both curves indicated a rapid increase of the fluorescence intensity within 8 sec, followed by an maintain their response after 8 sec. This result revealed that the reaction was complete within 8 sec, enabling rapid detection of *B. anthracis* spores. The response time of the 3-nm-diameter Eu-GQDs was 5.2 s, which is 1.5 times faster than that of the 10-nm-diameter Eu-GQDs (7.7 s). This is attributed to the larger surface-area-to-volume ratio of the 3-nm-diameter GQDs, enhancing contact between DPA and GQDs.[110] This rapid detection of DPA has considerable advantages in practical applications.

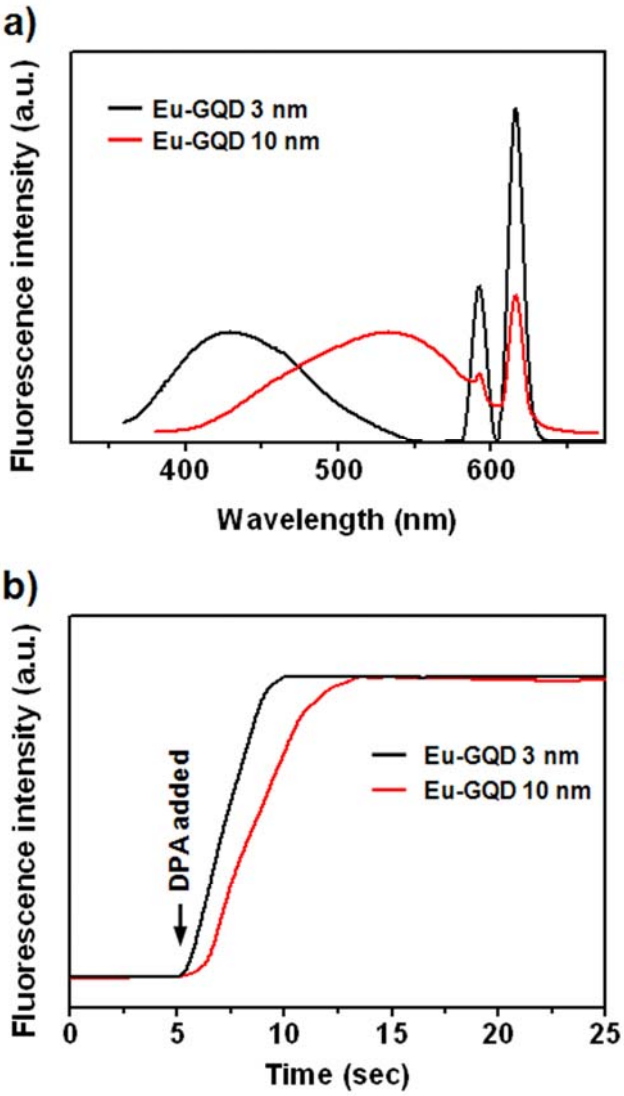

Figure 47. (a) Representative fluorescence spectra of 3-nm Eu-GQDs (black line) and 10-nm Eu-GQDs (red line) excited at 350 nm (red line). (b) Time-dependent fluorescence intensity plot of 3-nm Eu-GQDs (black line) and 10-nm Eu-GQDs (red line) following exposure to DPA (250 nM; fluorescence detected at 616 nm).

To evaluate the sensitivity of the Eu-GQDs, they were exposed to various concentrations of DPA in aqueous solution. Figure 48-49 shows the fluorescence intensities of GQDs, which increased linearly with increasing concentration of DPA. The LOD of the 3- and 10-nm-diameter Eu-GQDs was 10 pM and 50 pM, respectively. This is six orders of magnitude smaller than the infectious dose of the spores (60 μM).[111] The five-fold increase in sensitivity of the 3-nm-diameter Eu-GQDs compared with the 10-nm-diameter Eu-GQDs is attributed to the larger surface-area-to-volume ratio of the 3-nm GQDs, which led to an increased frequency of contact with the DPA, as well as the increased response of the baseline due to the overlap of emission from the GQDs and the Eu^{III} complex. This limit of detection (LOD) is 4 to 20 times more sensitive than those recently been reported using lanthanide metals.[104] This superior sensitivity of Eu-GQD can be explained by the large surface area of the GQDs and integration of macromolecules to provide active sites for the DPA to bind to. Figure 48b-48b shows a linear relationship between the emission intensity at 616 nm and the concentration of DPA. Compared with conventional fluorescence-based sensors, the Eu-GQD system has excellent sensing properties because the reference fluorescence plays a crucial role in calibration and correction of the concentration.

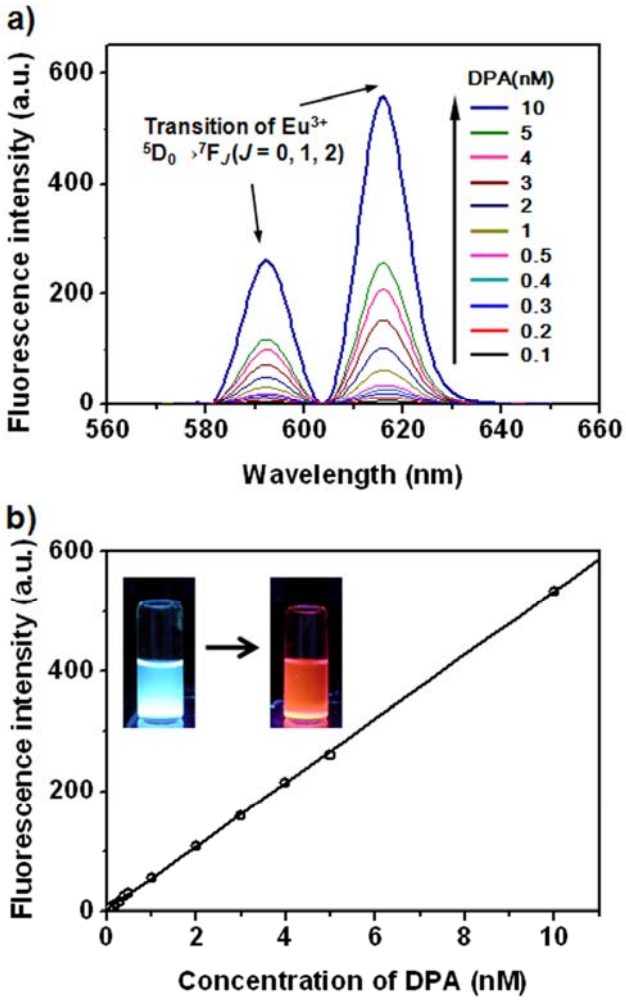

Figure 48. (a) Fluorescence spectra of 3-nm Eu-GQDs for various concentrations of DPA. (b) Fluorescence intensity of 3-nm Eu-GQDs at 616 nm as a function of the DPA concentration. The adjusted coefficient of determination was R^2 = 0.996 for the 3-nm Eu-GQDs. (inset: photo of 3-nm Eu-GQD and 3-nm Eu-GQD in the presence of 1 μM DPA under 364 nm UV irradiation)

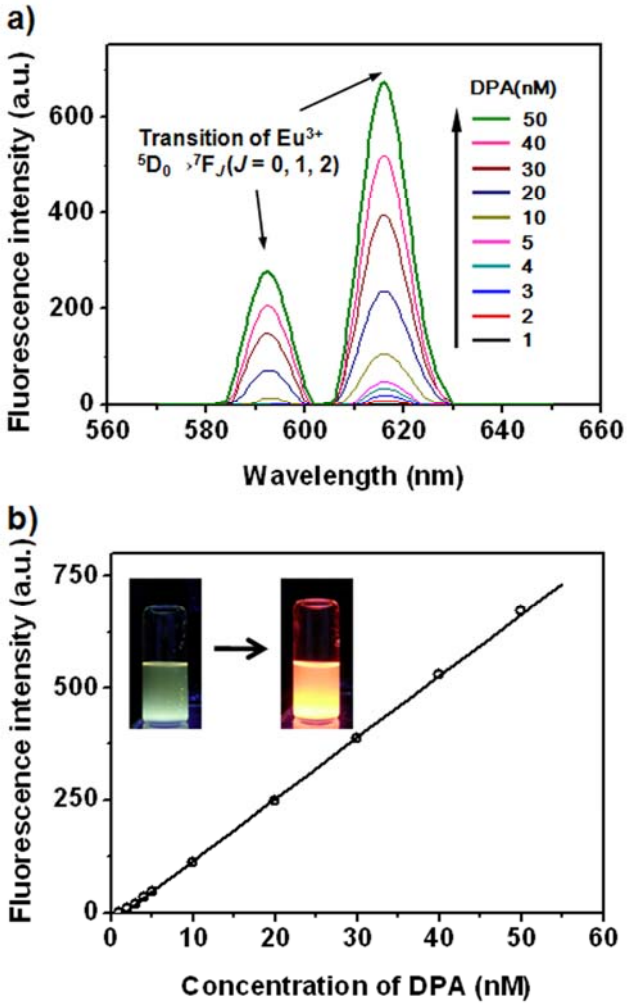

Figure 49. (a) Fluorescence spectra of 10-nm Eu-GQDs for various concentrations of DPA. (b) Fluorescence intensity of 10-nm Eu-GQDs at 616 nm as a function of the DPA concentration. The adjusted coefficient of determination was $R^2 = 0.994$ the 10-nm Eu-GQDs. (inset: photo of 10-nm Eu-GQD and 10-nm Eu-GQD in the presence of 1 μM DPA under 364 nm UV irradiation)

Moreover, the Eu^{III}-macrocycle complex system enables specific DPA binding in an aqueous solution because the EDTA binding maintains three available adjacent coordination sites and does not inhibit DPA binding. To determine the specificity of the Eu-based anthrax detector, the detectors were exposed to six aromatic ligands, such as benzoic acid, terephtalic acid, nicotinic acid, isophthalic acid, and picolinic acid, each at 1 μM concentration, as listed in Table 4. Although only very weak fluorescence changes were observed for aromatic ligands at the high concentration, DPA showed outstanding fluorescence enhancement of both Eu-GQD 3 and Eu-GQD 10 nm, respectively. (*ca.* 103- and 43-fold higher than other aromatic compounds, respectively) The higher selectivity of smaller Eu-GQD sensor was ascribed to the increase in surface area-to-volume-ratio. These results show that the Eu-GQD based sensors for anthrax detection can amplify the specific [Eu(EDTA)–(DPA)] interaction, thus enabling high sensitive and selective detection for practical applications.

Table 4. Normalized fluorescence intensity, I/I_0, in response to the addition of DPA and different aromatic ligands.

Ligands[a]	Eu-GQD, 3nm (I/I_0)	Eu-GQD, 10nm (I/I_0)
Dipicolinic acid	185.53	71.21
Benzoic acid	1.18	0.87
Terephthalic acid	1.46	1.21
Nicotinic acid	1.22	1.05
Isophthalic acid	1.40	1.13
Picolinic acid	1.85	1.67

[a] The concentration was 1μM for each ligand.

3.3.3. Photoinduced electron transfer based sensor probes for intracellular hydrogen peroxide.

A boronate and folic acid dual-modified fluorescent GQD was fabricated for use as a selective H_2O_2 probe and targeting of cancer cell, respectively. Figure 50 illustrates the schematic process of fluorescent boronate-modified graphene quantum dot (B-GQD) sensor and selective sensing of H_2O_2 into the target cancer cell. Initially, pristine blue photoluminescent GQDs (P-GQDs) were fabricated *via* an excessive oxidation and size-selective precipitation procedure as described in previously described.[21] By the reaction with ethylene dichloride (EDC), a carboxylic acid group on the surface of P-GQDs was converted to an active intermediate which reacts with N-Hydroxysuccinimide (NHS) to give relatively stable amine-reactive NHS-ester.[112] Then, the amine group of folic acid (FA) nucleophilically attacked the NHS-ester to form an amide bond, leading to covalent linkage to P-GQDs (folic acid-modified graphene quantum dot, F-GQD). Among various targeting system, the FA was selected as model targeting agent for enhancing internalization and selectivity of cancer cells. According to the target cell type, the FA can be easily substituted by other antibody. To graft the sensing moiety of H_2O_2 onto the F-GQDs, boronic acid pinacol ester was covalently bonded onto the F-GQDs *via* amid bond (B-GQDs). The as-synthesized B-GQDs were

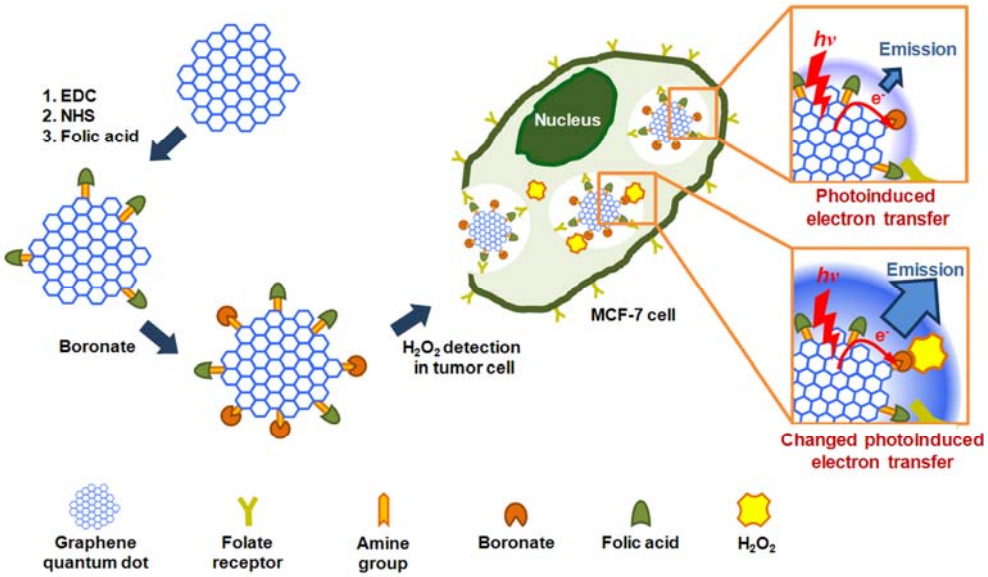

Figure 50. Schematic diagram of fabrication procedure of Boronate modified GQD and their sensing process with H_2O_2.

internalized in the MCF-7 cell (folate receptor overexpressed cells) *via* the FA-mediated targeting. Reaction with intracellular H_2O_2 made boronate groups of the B-GQD into pyridine groups, which induced efficient electronic communication between the B-GQDs and H_2O_2.[113] To the best of our knowledge, this is the first attempt to apply GQD as photoinduced electron transfer (PET) based sensor probes for intracellular hydrogen peroxide using their upconversion property.

To confirm the formation of GQDs (P-GQD, F-GQD and B-GQD), high-resolution transmission electron microscopy (HR-TEM) analysis and size-distribution analysis was conducted in Figure 51. As displayed in Figure 51a, the P-GQDs were uniform and monodispersed with average diameter of ~3 nm. After the functionalization of P-GQD with FA, the F-GQD exhibited higher atomic density compared to P-GQD, and the average diameter increased to ~4.8 nm (Figure 51b). Following grafting boronic acid pinacol ester onto the F-GQD, B-GQD exhibited average diameter further increased to ~5.8 nm, indicating successful functionalization of B-GQD (Figure 51c).

The formation of GQDs was confirmed using both fourier-transform infrared (FT-IR) spectroscopy and X-ray photoelectron spectroscopy (XPS). In Figure 52, the FT-IR spectrum of the P-GQD shows characteristic C–H deformation peaks at 835 cm^{-1}, C–O–C stretching peaks 1236 cm^{-1}, C–O

stretching peaks at 1360 cm^{-1}, and C=C aromatic stretching peaks at 1591 cm^{-1}, indicating the successful synthesis of P-GQD. In case of F-GQD, the peaks related to amines increased in intensity, including the N–H bending mode at 655 cm^{-1} and 1530 cm^{-1} and C–N stretching modes at 1179 cm^{-1} and C=N stretching at 1690 cm^{-1}. The B–GQD exhibited new peaks related to the boronate, including B–C stretching at 1049 and 1087 cm^{-1} and B–OH stretching at 3306 cm^{-1}. On the basis of these data, FA and boronic acid pinacol ester successfully modified the B-GQD surfaces.

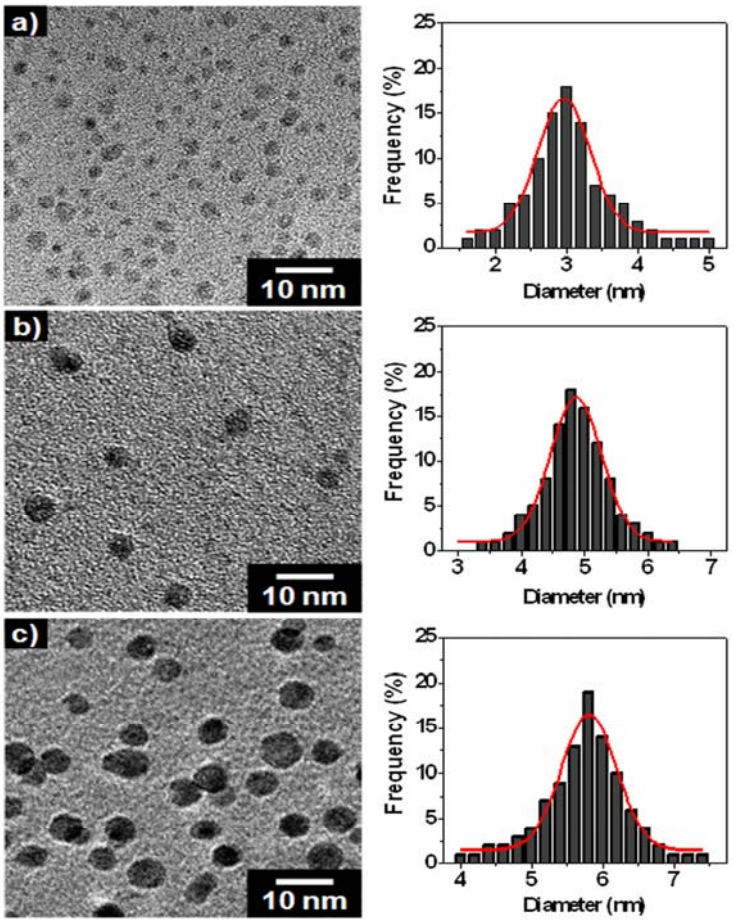

Figure 51. HR-TEM images and size-distribution analysis of (a) P-GQD, (b) F-GQD, and (c) B-GQD

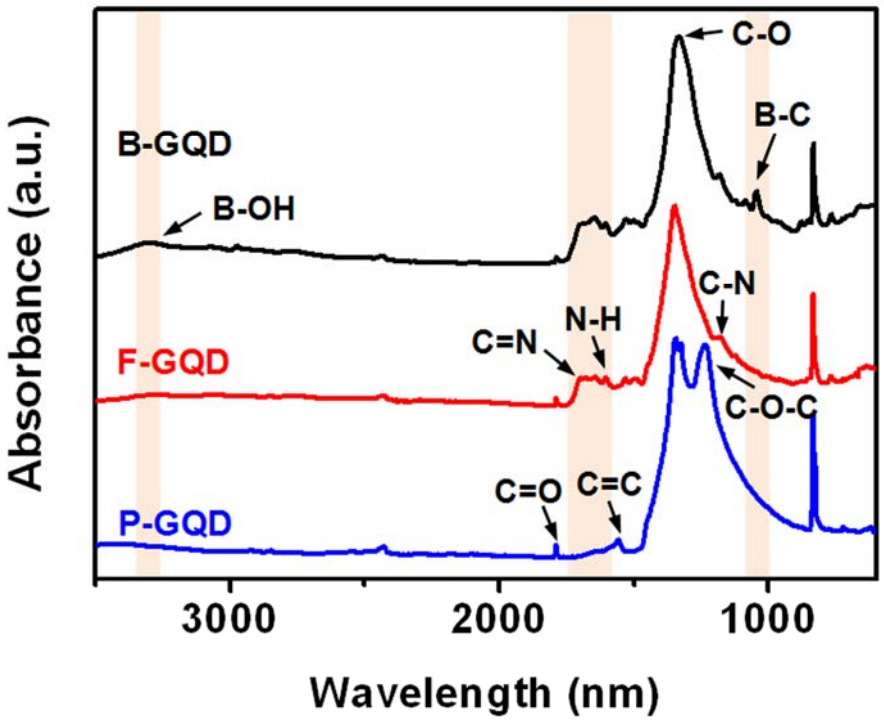

Figure 52. FT-IR spectra of P-GQD (black line), F-GQD (red line), and B-GQD (blue line).

Figure 53 shows XPS characterization of P-GQD, including surface-modified F-GQD and B-GQD. The atomic concentrations of C, N, and O in the GQDs were determined to be 54.78%, 0.12%, and 45.10%, respectively. In the F-GQD, the atomic concentrations were 48.17% (C), 4.64% (N), and 47.19% (O), which indicates that the N 1s region was enlarged. Additionally, the B 1s (3.54%) region appeared in the B-GQD, which is attributed to the boronate group. The deconvoluted C1s XPS spectrums of P-GQD, F-GQD, and B-GQD are presented in Figure 53b-d. The main peaks of GQD at 284.6 eV (peak I) corresponds to the graphite-like sp^2 carbon, indicating most of the carbon atoms are arranged in honeycomb lattice.[21] In addition, the small peaks of P-GQD can be attributed to C−O (peak II, 286.0 eV), −COOR (peak III, 287.8 eV), and CO_3^{2-} (peak IV, 290.1 eV), respectively. After the FA treatment, the peak intensity related to C−N bonding (peak II and III) significantly increased in F-GQD, which can be attributed to the functionalization of P-GQD by conjugation with FA. In the case of B-GQD, the peaks related to ether and amine group (peak II and III) increased indicating the formation of amide bonding with boronate. As the above results, XPS spectra and enlarged C1s spectra confirmed the successful fabrication of F-GQD and B-GQD.

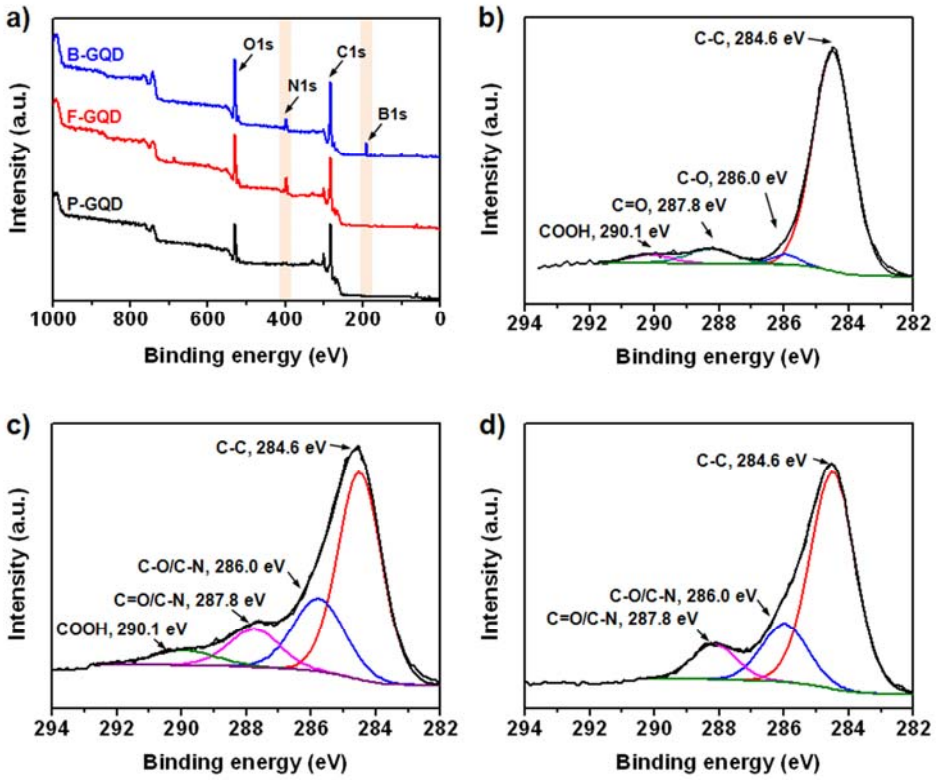

Figure 53. (a) XPS spectra of P-GQD (black line), F-GQD (red line), and B-GQD (blue line). Enlarged C1s spectra of (b) P-GQD, (c) F-GQD, and (d) B-GQD.

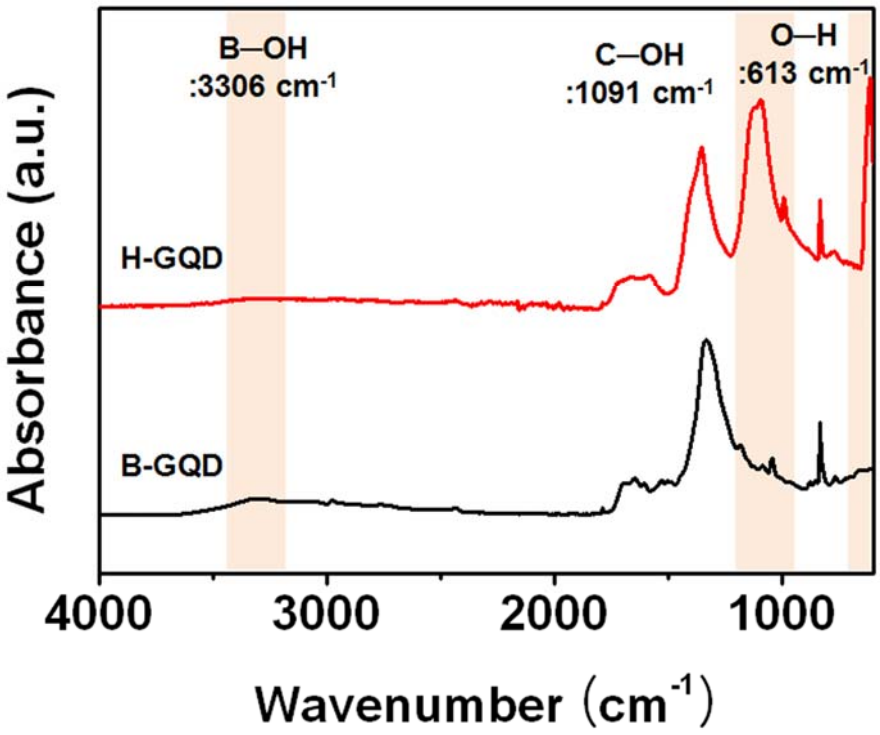

Figure 54. FT-IR spectra of B-GQD (red line) and H-GQD (black line).

Figure 55a displays representative absorbance spectra of F-GQD and B-GQD. UV-vis spectra showed a new shoulder peak at 265 nm in B-GQD due to surface modification of F-GQD with pyridine-3-boronic acid pinacol ester though amide bond. Figure 55c and d shows that F-GQD had optimal excitation and emission wavelengths at 280 nm and 410 nm, while excitation and emission wavelengths of B-GQD were changed into 300 nm and 360 nm. These peak shifts were originated from efficient electronic communication between the F-GQD and pyridine-3-boronic acid pinacol ester group; such as the construction of the π-conjugation and PET.[114] The fluorescence quantum yield of the F-GQD was calculated as *ca.* 0.02 (blue) using the standard reference, 7-amino-4-methylcoumarin. After surface modification, the fluorescence quantum yield of B-GQD (red) was *ca.* 0.52, which is 26 time higher than that of the F-GQD (Figure 55b).[115] In the previous research, the fluorescence quantum yield of boronate-modified polyacrylonitrile nanoparticles is only *ca.* 0.10.[114] Notably, F-GQD and B-GQD also exhibited upconversion excitation-dependent PL behaviors (Figure 55e and 55f). The emission wavelengths of F-GQD and B-GQD were red-shifted when changing excitation wavelengths from 560 nm to 640 nm and 470 nm and 540 nm, respectively. These upconversion excitation-dependent PL property is possibly attributed to the two or multiphoton active process.[116] The highest

fluorescence intensity was measured at 433 nm in F-GQD (λ_{ex}=580 nm), while that of B-GQD was shown at 351 nm (λ_{ex}=490 nm). Similar to down-conversion properties, the optimized excitation and emission wavelength of B-GQD was blue shifted compared to those of F-GQD. Upconversion PL properties can provide relatively reduced background signal and enhanced sensitivity owing to the absence of autofluorescence.[117] Additionally, because of longer penetration depth, nanomaterials that have higher excitation wavelength are preferred for fluorescence applications in biomedical science such as bioimaging agent and fluorescent sensor.[118] Collectively, upconversion PL properties of B-GQD may provide a possibility for the use of intracellular fluorescence sensor with high sensitivity.

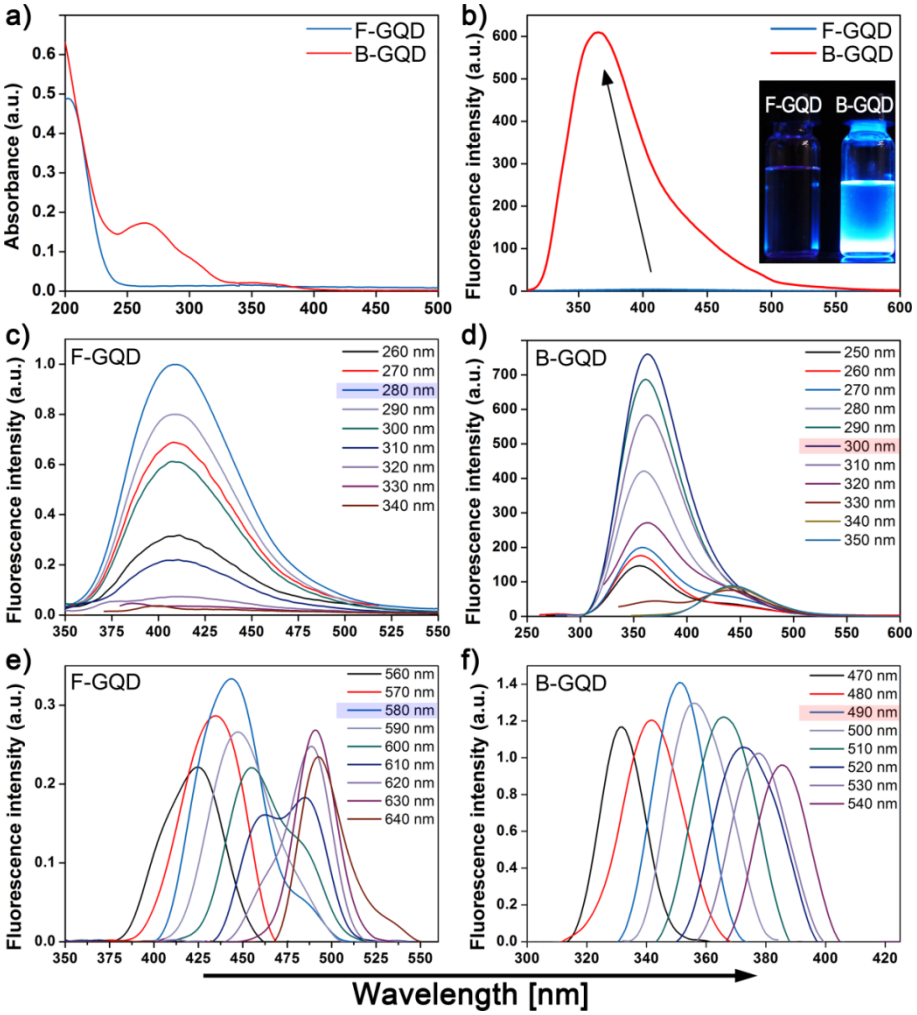

Figure 55. (a) UV-vis absorption spectra and (b) the representative fluorescence spectra of the F-GQD (blue line) and the B-GQD (red line). Inset: Photograph taken with UV lamp irradiation (254 nm). (c-d) Fluorescence spectra and (e-f) upconversion spectra of the F-GQD and B-GQD at different excitation wavelength in 0.1 M HEPES buffer.

We then explored the capability of the B-GQD as a fluorescence sensor for hydrogen peroxide (Figure 56a). The added H_2O_2 induced a marked increase in fluorescence intensity of the B-GQD and the peak was red-shifted from 350 to 360 nm when the excitation wavelength was 490 nm. Figure 56b exhibits that B-GQD detects H_2O_2 in a ratiometric manner. The limit of detection value of B-GQD for H_2O_2 was 20 pM, which is 5 times higher sensitivity compared to previous boronated polyacrylonitrile nanoparticles.[114] Furthermore, the rate of conversion of B-GQD to H_2O_2-treated B-GQD (H-GQD) was calculated as 2.02 M^{-1} s^{-1} by measuring the change in absorption using pseudo-first-order reaction conditions with an excess of H_2O_2. These data provide further evidence that H_2O_2-triggered conversion of 3-pyrdineboronic acid pinacol ester is a robust and versatile methodology for reaction-based H_2O_2 detection.

Figure 57 presents a remarkable selectivity of B-GQD for H_2O_2 over other variety of biologically relevant ROS, including hypochlorite (OCl^-), hydroxyl radical (·OH), and *tert*-butoxy radicals (·OtBu). H_2O_2 induced increase of the fluorescence intensity at an excitation wavelength of 490 nm, and the fluorescence change was ratiometric. Hypochlorite, however, showed a decreased fluorescent intensity and the intensity barely changed with other ROS. Based on these data, we proposed the mechanism of the PET process between H_2O_2 and B-GQD (Figure 56c). B-GQD consists of two parts; GQD

which exhibited fluorescence and boronic acid pinacol ester group which reacted with H_2O_2. Boron atom of the boronic acid pinacol ester group was in the sp^2 state, which means they can act as an electron acceptor from the excited-state GQD donor.[119] The UV and PL data suggested that when GQD is excited (490 nm; $h\nu_1$), a PET occurred from the GQD donor to the boron atom acceptor, which leads to quench the fluorescence (350 nm; $h\nu_2$). After addition of H_2O_2, the boronic acid pinacol ester was transformed into hydroxyl group (Figure 54).[113, 114] There is no PET process because of absence of electron acceptor; the fluorescence intensity is enhanced consequently. In case of hypochlorite, like H_2O_2, they were reacted with boronic acid pinacol ester group and produced hydroxyl group.[120] Higher hypochlorite concentration, however, caused a rapid decrease in the levels of phenolic product, and they formed chlorinated phenol.[120] The chlorine group, acted as an electron withdrawing group, induced PET process again. Fluorescence intensity of B-GQD gradually decreased as hypochlorite inserted. These chemospecific boronate switch and PET properties make B-GQD as good selective sensor probe for H_2O_2 over a variety of biologically relevant ROS.

In order to confirm the interference from metabolites, fluorescence intensity changes of B-GQD was measured in the presence of various metabolites (Ca^{2+} as an ion, L-glutamine as an amino acid, L-ascorbic acid as a

vitamin; 1 mM) at 350 nm excitation. Figure 57b shows H_2O_2 measurement was not interfered no matter what metabolites were inserted in the solution. The concentration of metabolites in this experiment is 1 mM, which is much higher than average metabolite concentration in body. Considering these data, our B-GQD can be applied as selective sensor probe for H_2O_2 in biological system.

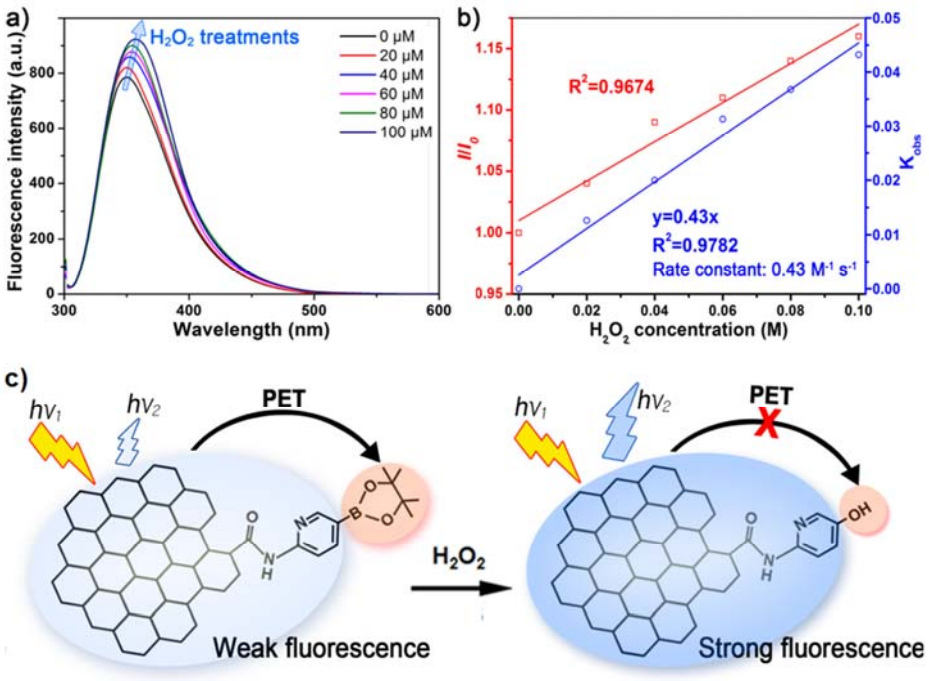

Figure 56. (a) Fluorescence spectra of B-GQD in the presence of H_2O_2. (b) The linear correlation between the emission intensity at 350 nm and H_2O_2 concentration (red line), and plot of K_{obs} against H_2O_2 concentration to determine the rate constant for B-GQD and H_2O_2 (blue line). c) An illustration of the PET mechanism of H_2O_2 sensing by B-GQD.

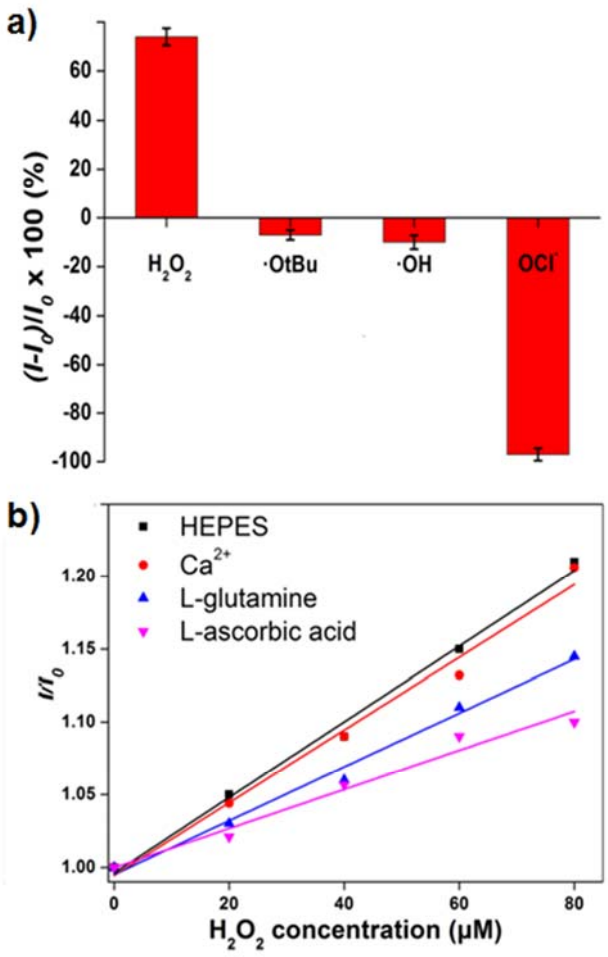

Figure 57. (a) Fluorescence change of B-GQD after addition of H_2O_2 or other ROS (200 μM) excited at 490 nm. (b) Fluorescence response of B-GQD versus the concentration of H_2O_2 in the presence of various metabolites (1 mM).

On the basis of these data, the sensing capability of the B-GQD was systematically investigated *in vitro* (Figure 58). In our experiments, two cell lines were used: MCF-7 (folate receptor overexpressed cell; target; FR+) and SK-BR-3(absence of folate receptor; control; FR-).[121] Figure 58a illustrates phorbol-12-myristate-13-acetate (PMA; stimulator for the generation of intracellular H_2O_2) concentration-dependent fluorescence changes of B-GQD in MCF-7 cells (7.5 μg mL^{-1}). The increase of PMA concentration induced intracellular hydrogen peroxide generation, resulting in the fluorescence increment of B-GQD. Figure 58b shows linear correlation between the B-GQD dose and fluorescence intensity in the presence of PMA (4 μg mL^{-1}). As the B-GQD concentration increases, more intracellular hydrogen peroxide is captured by B-GQD. In case of SK-BR-3 cells, no PMA and B-GQD concentration-dependent fluorescence changes were observed due to absence of folate receptor.

Individual intracellular fluorescence intensities were also evaluated using flow cytometry analysis for quantifying internalized B-GQD in the presence or absence of folate receptor on the cells (Figure 59). Because of the restriction of the flow cytometry laser wavelength, fluorescein isothiocyanate-modified B-GQD were used for this experiment.[114] Both cells were incubated with 10 μg mL^{-1} B-GQD for 24 h, and then individual intracellular fluorescence

intensities were measured. The B-GQD-internalized MCF-7 and SK-BR-3 cells were calculated as 27.1% and 5.7%, respectively. Based on these data, it can be concluded that B-GQD is selectively internalized in folate positive cells and detect hydrogen peroxide ratiometrically.

The upconversion fluorescence image of B-GQD treated cells and their mean fluorescence intensity values are shown in Figure 55d and 55e, respectively. B-GQD was successfully internalized into MCF-7 cells and they exhibited more uniform and higher fluorescence than B-GQD in SK-BR-3 cells, indicating targeting ability of B-GQD for folate receptor positive cells. After 5 μg mL^{-1} PMA treatment, the fluorescence of B-GQD were increased 1.7 times in MCF-7 cells, while there is no fluorescence change in F-GQD inserted cells owing to absence of boronic acid pinacol ester group (Figure 54). These data provided upconverted B-GQD were capable of visualizing generated H_2O_2 in MCF-7 cells owing to efficient PET process after reaction with H_2O_2. These results are in accordance with the previous reports that mono-boronate group can detect H_2O_2 in PMA-treated cells.

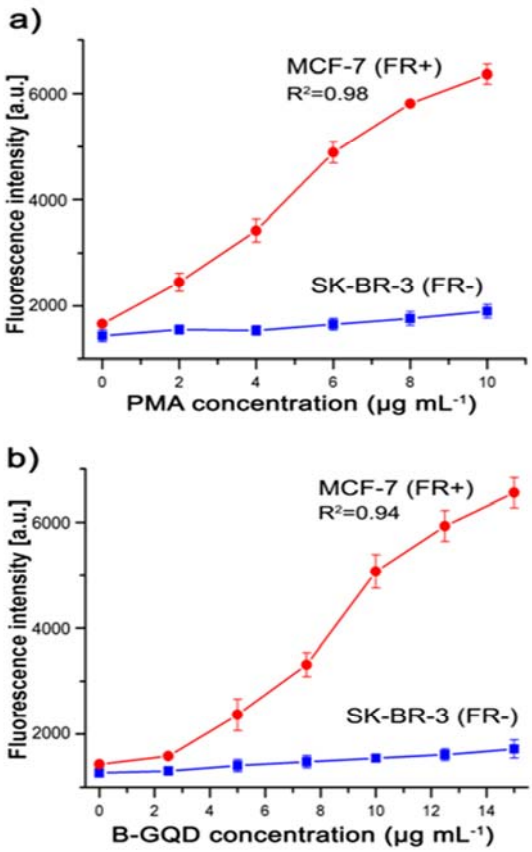

Figure 58. (a-b) Titration curves as a function of PMA and B-GQD concentration in the cells. The concentration of B-GQD and PMA were fixed as 7.5 μg mL^{-1} and 4 μg mL^{-1}, respectively.

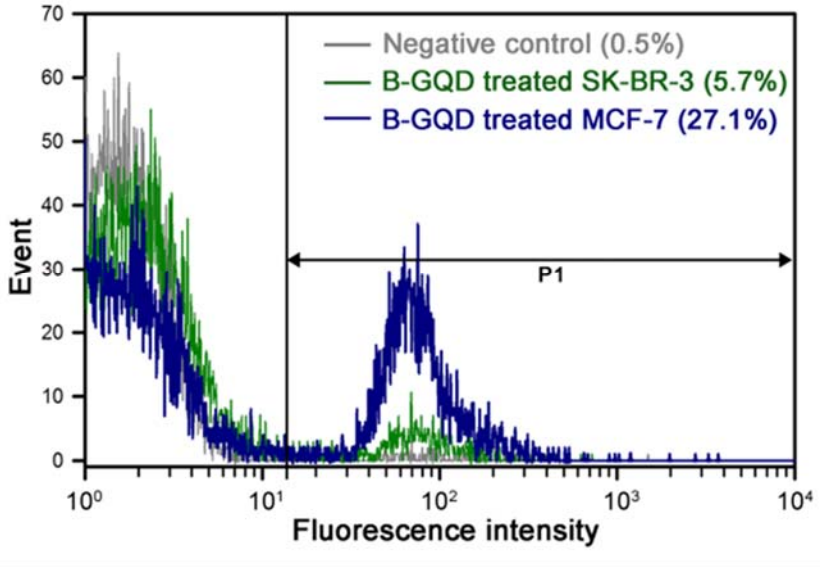

Figure 59. Quantification of F-GQD and B-GQD (10 μg mL^{-1}) treated MCF and SK-BR-3 cells.

According to the fluorescence images, B-GQD had no considerable change in cell shape. The viabilities of B-GQD- and F-GQD-treated MCF-7 cells were checked *in vitro* (Figure 60a). The level of ATP production in F-GQD and B-GQD-treated cells exhibited no significant decrease compared to negative control. The lowest viability was about 85% even at a high concentration of B-GQD (250 μg mL^{-1}). Previous researches reported that the viability of fluorescent polymer nanoparticle-treated cells was about 82% at same concentration.[114] In general, fluorescent polymer nanoparticles are known as low toxic materials. Based on these data, B-GQD can be considered as low toxic materials and are suitable for bio-applications. We further test their ROS generating ability because generating ROS can affect not only toxicity but also accuracy of the fluorescence sensing result of B-GQD. As shown in Figure 61, the ROS values showed no significant change compared to negative control, like cell viability results. Therefore, the B-GQD is an effective intracellular H_2O_2 detector without significant ROS production. Judging from these data, B-GQD provides ratiometric and selective H_2O_2 detection with low toxicity in only folate positive cells.

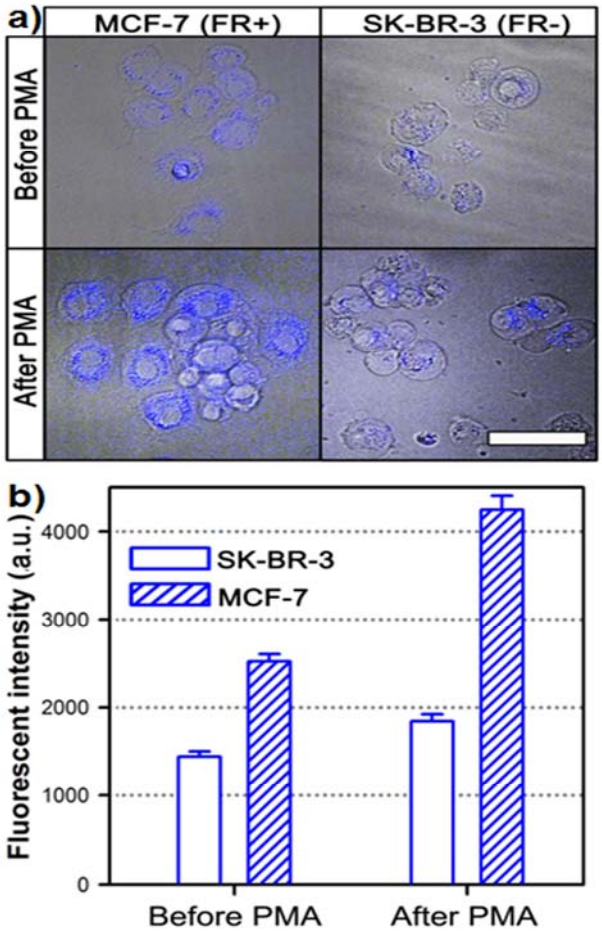

Figure 60. (a) Live cell differential interference images of the cells and (b) their relative fluorescence intensity. Both cells were treated with 10 μg mL^{-1} of B-GQD for 24 h, and 5 μg mL^{-1} PMA was additionally inserted for intracellular H_2O_2 generation (scale bar: 90 μm).

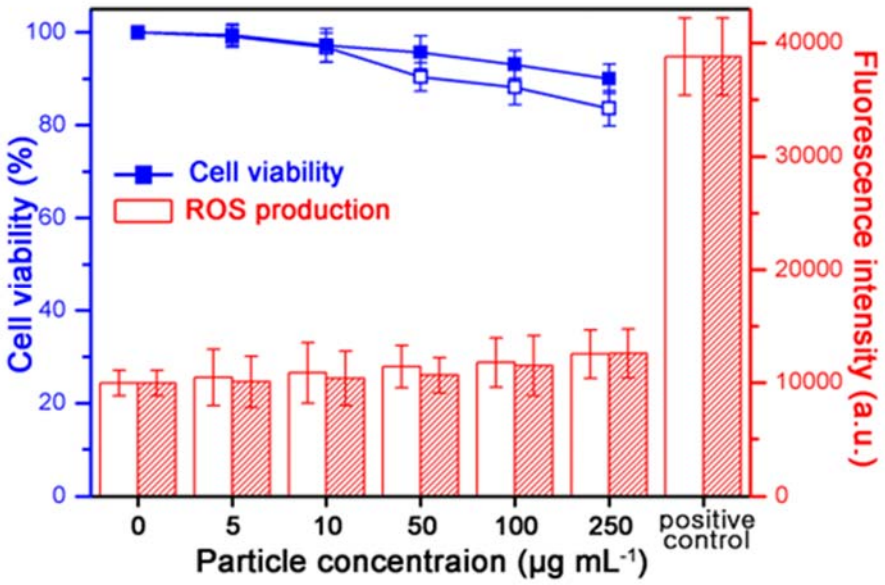

Figure 61. Viability of MCF-7 cells incubated with F-GQD (solid squares) and B-GQD (open circles) for 24 h. ROS production by MCF-7 cells after being incubated with F-GQD (shaded bars) and B-GQD (open bars). H_2O_2 (0.02%) was used as a positive control.

4. CONCLUSIONS

1. The GQDs with well-defined and low size distribution are successfully fabricated using a simple oxidation of carbon nanomaterials and size-selective precipitation. To control the size and luminesecence wavelength of graphene quantum dots, different types of CNs and various oxidation conditions are studied. Interestingly, the diameter and luminescence wavelength of graphene quantum dots can be controlled by selectively designing the morphology of starting materials and optimizing the oxidation condition.
2. A carbonization approach of organic precursor with doping sources was proposed in order to fabrciate heteroatoms-doped graphene quantum dots. Under the catalytic reaction conditions of H_2SO_4, citric acid can be transformed to GQD due to the dehydration forming a graphitic hexagonal matrix. To enhance the PL efficiency of GQDs, various types of doping sources and carbonization degree was studied. This simple and novel strategy offers great possibility for fabricating heteroatom(S or N)-doped GQDs with precise control of carbonization degree, a gram-scale production, and high-PLQY (*ca.* 61%).
3. The high FLQY-GQDs could be used as light-harvesting antennae in FRET-based photovoltaic devices. The GQDs were doposited onto the top

of a TiO_2 working electrode of DSSCs *via* spincoating forming GQD-modified layer. The GQD-layer modified DSSCs was implemented for simultaneous utilize the wide solar spectrum, thereby resulting in high conversion efficiency (7.95%) over a wide wavelength range. Furthermore, the synthexsized GQDs exhibited excellent upconversion properties, and proved to be a feasible candidate for a phosphor in photovoltaic devices to enhance the light-harvesting ability in the long-wavelength range.

4. A novel and facile strategy based on the hybridization of GQDs into a europium (Eu)-macromolecule complex was demonstrated for detecting of *B. anthracis* spores. This novel approach involves anchoring Eu onto GQDs of two different diameters, which provides a change in the fluorescence intensity that varies with the concentration of *B. anthracis*. Most importantly, the Eu-modified GQDs reported here exhibit an excellent limit of detection (LOD) of 10 pM towards *B. anthracis* due to larger surface to volume ratio originated from the nanometer-sized GQDs. The insight into the size-dependence of detection properties of GQds and binding with europium complex offer an opportunity for the further investigation of biological & medical applications, and can be generalized to the fabrication for highly efficient detection probes using the concept of GQD based platform.

5. A novel approach to fabricate GQD based-upconversion fluorescence sensor probe for intracellular H_2O_2 was demonstrated. B-GQD can internalize into folate positive cells (MCF-7 cells) selectively due to folic acid, and then reacted with intracellular H_2O_2 over other competing ROS. After detection, fluorescence peak of B-GQD increased and shifted, which allows ratiometric and selective H_2O_2 detection at concentration as low as 20 pM. To the best of our knowledge, this is the first attempt to apply GQD as PET based sensor probes for intracellular H_2O_2 using their upconversion property. Considering these findings, the B-GQD offers a new system to selectively recognize H_2O_2 in specific cells and may lead to biomedical applications as an intracellular H_2O_2 sensor.

In summary, two different ways in the synthetic methodology of size-and PL-controlled GQDs were demonstrated in the viewpoint of top-down approach and bottom-up approach. As a ‘top-down approach’, the GQDs with well-defined and low size distribution were successfully fabricated using a simple oxidation of carbon nanomaterials and size-selective precipitation. Interestingly, the diameter and luminescence wavelength of graphene quantum dots can be controlled by selectively designing the morphology of starting materials and optimizing the oxidation condition. As a ‘bottom-up approach’,

heteroatoms-doped GQDs were formed using simple carbonization approach of organic precursor with two different doping sources. The well-defined S, N-doped GQDs were obtained with the assistance of acidic dopant and quenching solvent at a mild carbonization condition. This novel strategy does not require a high carbonization temperature and pressure, and the simple strategy offers great possibility for fabricating heteroatom(S or N)-doped GQDs with precise control of carbonization degree, a gram-scale production, and high-PLQY (*ca.* 61%). The size-controlled GQDs have been successfully applied in a wide variety of applications, suggesting that these nanomaterials may be potentially very useful in many new types of applications related to electronic/ optoelectronic devices, fluorescent probe, bioimaging system, and energy conversion systems.

REFERENCES

[1] M. S. Dresselhaus, G. Dresselhaus, R. Saito, A. Jorio, *Physics Reports* **2005**, *409*, 47.

[2] D. V. Kosynkin, A. L. Higginbotham, A. Sinitskii, J. R. Lomeda, A. Dimiev, B. K. Price, J. M. Tour, *Nat.* **2009**, *458*, 872.

[3] L. Li, G. Wu, G. Yang, J. Peng, J. Zhao, J.-J. Zhu, *Nanoscale* **2013**, *5*, 4015.

[4] A. K. Geim, K. S. Novoselov, *Nat. Mater.* **2007**, *6*, 183.

[5] J. Y. Hong, J. Jang, *J. Mater. Chem.* **2012**, *22*, 8179.

[6] Y. Hernandez, V. Nicolosi, M. Lotya, F. M. Blighe, Z. Sun, S. De, I. T. McGovern, B. Holland, M. Byrne, Y. K. Gun'ko, J. J. Boland, P. Niraj, G. Duesberg, S. Krishnamurthy, R. Goodhue, J. Hutchison, V. Scardaci, A. C. Ferrari, J. N. Coleman, *Nature Nanotechnology* **2008**, *3*, 563.

[7] R. M. Westervelt, *Science* **2008**, *320*, 324.

[8] G. Konstantatos, M. Badioli, L. Gaudreau, J. Osmond, M. Bernechea, F. P. G. De Arquer, F. Gatti, F. H. L. Koppens, *Nature Nanotechnology* **2012**, *7*, 363.

[9] V. Gupta, N. Chaudhary, R. Srivastava, G. D. Sharma, R. Bhardwaj, S. Chand, *J. Am. Chem. Soc.* **2011**, *133*, 9960.

[10] H. Cheng, Y. Zhao, Y. Fan, X. Xie, L. Qu, G. Shi, *ACS Nano* **2012**, *6*,

2237.

[11] L. A. Ponomarenko, F. Schedin, M. I. Katsnelson, R. Yang, E. W. Hill, K. S. Novoselov, A. K. Geim, *Science* **2008**, *320*, 356.

[12] J. Lee, K. Kim, W. I. Park, B. H. Kim, J. H. Park, T. H. Kim, S. Bong, C. H. Kim, G. Chae, M. Jun, Y. Hwang, Y. S. Jung, S. Jeon, *Nano Lett.* **2012**, *12*, 6078.

[13] S. Kim, S. W. Hwang, M. K. Kim, D. Y. Shin, D. H. Shin, C. O. Kim, S. B. Yang, J. H. Park, E. Hwang, S. H. Choi, G. Ko, S. Sim, C. Sone, H. J. Choi, S. Bae, B. H. Hong, *ACS Nano* **2012**, *6*, 8203.

[14] G. Eda, Y. Y. Lin, C. Mattevi, H. Yamaguchi, H. A. Chen, I. S. Chen, C. W. Chen, M. Chhowalla, *Adv. Mater.* **2010**, *22*, 505.

[15] J. Shen, Y. Zhu, X. Yang, C. Li, *Chem. Commun.* **2012**, *48*, 3686.

[16] S. Zhu, J. Zhang, C. Qiao, S. Tang, Y. Li, W. Yuan, B. Li, L. Tian, F. Liu, R. Hu, H. Gao, H. Wei, H. Zhang, H. Sun, B. Yang, *Chem. Commun.* **2011**, *47*, 6858.

[17] L. Cao, M. J. Meziani, S. Sahu, Y. P. Sun, *Acc. Chem. Res.* **2013**, *46*, 171.

[18] S. N. Baker, G. A. Baker, *Angew. Chem., Int. Ed.* **2010**, *49*, 6726.

[19] S. Song, Y. Qin, Y. He, Q. Huang, C. Fan, H. Y. Chen, *Chem. Soc. Rev.* **2010**, *39*, 4234.

[20] S. Zhuo, M. Shao, S. T. Lee, *ACS Nano* **2012**, *6*, 1059.

[21] E. Lee, J. Ryu, J. Jang, *Chem. Commun.* **2013**, *49*, 9995.

[22] I. L. Medintz, H. T. Uyeda, E. R. Goldman, H. Mattoussi, *Nat. Mater.* **2005**, *4*, 435.

[23] X. Michalet, F. F. Pinaud, L. A. Bentolila, J. M. Tsay, S. Doose, J. J. Li, G. Sundaresan, A. M. Wu, S. S. Gambhir, S. Weiss, *Science* **2005**, *307*, 538.

[24] D. S. L. Abergel, V. Apalkov, J. Berashevich, K. Ziegler, T. Chakraborty, *Advances in Physics* **2010**, *59*, 261.

[25] X. Yan, X. Cui, B. Li, L. S. Li, *Nano Lett.* **2010**, *10*, 1869.

[26] Y. Li, Y. Zhao, H. Cheng, Y. Hu, G. Shi, L. Dai, L. Qu, *J. Am. Chem. Soc.* **2012**, *134*, 15.

[27] E. Morales-Narváez, A. Merkoçi, *Adv. Mater.* **2012**, *24*, 3298.

[28] J. Cai, P. Ruffieux, R. Jaafar, M. Bieri, T. Braun, S. Blankenburg, M. Muoth, A. P. Seitsonen, M. Saleh, X. Feng, K. Müllen, R. Fasel, *Nat.* **2010**, *466*, 470.

[29] D. R. Dreyer, S. Park, C. W. Bielawski, R. S. Ruoff, *Chem. Soc. Rev.* **2010**, *39*, 228.

[30] S. Stankovich, D. A. Dikin, G. H. B. Dommett, K. M. Kohlhaas, E. J. Zimney, E. A. Stach, R. D. Piner, S. T. Nguyen, R. S. Ruoff, *Nat.* **2006**,

442, 282.

[31] K. S. Kim, Y. Zhao, H. Jang, S. Y. Lee, J. M. Kim, J. H. Ahn, P. Kim, J. Y. Choi, B. H. Hong, *Nat.* **2009**, *457*, 706.

[32] X. Li, W. Cai, J. An, S. Kim, J. Nah, D. Yang, R. Piner, A. Velamakanni, I. Jung, E. Tutuc, S. K. Banerjee, L. Colombo, R. S. Ruoff, *Science* **2009**, *324*, 1312.

[33] T. Ohta, A. Bostwick, T. Seyller, K. Horn, E. Rotenberg, *Science* **2006**, *313*, 951.

[34] D. Yu, Q. Zhang, L. Dai, *J. Am. Chem. Soc.* **2010**, *132*, 15127.

[35] R. Ye, C. Xiang, J. Lin, Z. Peng, K. Huang, Z. Yan, N. P. Cook, E. L. G. Samuel, C.-C. Hwang, G. Ruan, G. Ceriotti, A.-R. O. Raji, A. A. Martí, J. M. Tour, *Nat Commun* **2013**, *4*.

[36] S. Stankovich, D. A. Dikin, R. D. Piner, K. A. Kohlhaas, A. Kleinhammes, Y. Jia, Y. Wu, S. T. Nguyen, R. S. Ruoff, *Carbon* **2007**, *45*, 1558.

[37] Z. Li, W. Zhang, Y. Luo, J. Yang, J. G. Hou, *J. Am. Chem. Soc.* **2009**, *131*, 6320.

[38] Y. Li, W. Zhou, H. Wang, L. Xie, Y. Liang, F. Wei, J. C. Idrobo, S. J. Pennycook, H. Dai, *Nature Nanotechnology* **2012**, *7*, 394.

[39] J. Peng, W. Gao, B. K. Gupta, Z. Liu, R. Romero-Aburto, L. Ge, L.

Song, L. B. Alemany, X. Zhan, G. Gao, S. A. Vithayathil, B. A. Kaipparettu, A. A. Marti, T. Hayashi, J. J. Zhu, P. M. Ajayan, *Nano Lett.* **2012**, *12*, 844.

[40] K. Parvez, S. Yang, Y. Hernandez, A. Winter, A. Turchanin, X. Feng, K. Müllen, *ACS Nano* **2012**, *6*, 9541.

[41] C. Burda, X. Chen, R. Narayanan, M. A. El-Sayed, *Chem. Rev.* **2005**, *105*, 1025.

[42] A. H. Lu, E. L. Salabas, F. Schüth, *Angew. Chem., Int. Ed.* **2007**, *46*, 1222.

[43] B. L. Cushing, V. L. Kolesnichenko, C. J. O'Connor, *Chem. Rev.* **2004**, *104*, 3893.

[44] D. Pan, J. Zhang, Z. Li, M. Wu, *Adv. Mater.* **2010**, *22*, 734.

[45] B. Liu, E. S. Aydil, *J. Am. Chem. Soc.* **2009**, *131*, 3985.

[46] F. Yang, M. Zhao, B. Zheng, D. Xiao, L. Wu, Y. Guo, *J. Mater. Chem.* **2012**, *22*, 25471.

[47] M. J. McAllister, J. L. Li, D. H. Adamson, H. C. Schniepp, A. A. Abdala, J. Liu, M. Herrera-Alonso, D. L. Milius, R. Car, R. K. Prud'homme, I. A. Aksay, *Chem. Mater.* **2007**, *19*, 4396.

[48] J. I. Parades, S. Villar-Rodil, A. Martínez-Alonso, J. M. D. Tascón, *Langmuir* **2008**, *24*, 10560.

[49] L.-L. Li, J. Ji, R. Fei, C.-Z. Wang, Q. Lu, J.-R. Zhang, L.-P. Jiang, J.-J. Zhu, *Adv. Funct. Mater.* **2012**, *22*, 2971.

[50] J. Lu, J.-x. Yang, J. Wang, A. Lim, S. Wang, K. P. Loh, *ACS Nano* **2009**, *3*, 2367.

[51] L. Tang, Y. Wang, Y. Li, H. Feng, J. Lu, J. Li, *Adv. Funct. Mater.* **2009**, *19*, 2782.

[52] Y. Li, Y. Hu, Y. Zhao, G. Shi, L. Deng, Y. Hou, L. Qu, *Adv. Mater.* **2011**, *23*, 776.

[53] X. Yan, X. Cui, L.-s. Li, *J. Am. Chem. Soc.* **2010**, *132*, 5944.

[54] K. A. Ritter, J. W. Lyding, *Nat. Mater.* **2009**, *8*, 235.

[55] B. Trauzettel, D. V. Bulaev, D. Loss, G. Burkard, *Nature Physics* **2007**, *3*, 192.

[56] X. Li, S. P. Lau, L. Tang, R. Ji, P. Yang, *Journal of Materials Chemistry C* **2013**, *1*, 7308.

[57] Q. Liu, B. Guo, Z. Rao, B. Zhang, J. R. Gong, *Nano Lett.* **2013**, *13*, 2436.

[58] J. Peng, W. Gao, B. K. Gupta, Z. Liu, R. Romero-Aburto, L. Ge, L. Song, L. B. Alemany, X. Zhan, G. Gao, S. A. Vithayathil, B. A. Kaipparettu, A. A. Marti, T. Hayashi, J.-J. Zhu, P. M. Ajayan, *Nano Lett.* **2012**, *12*, 844.

[59] J. Kim, Y. Piao, T. Hyeon, *Chem. Soc. Rev.* **2009**, *38*, 372.

[60] P. Sharma, S. Brown, G. Walter, S. Santra, B. Moudgil, *Adv. Colloid Interface Sci.* **2006**, *123-126*, 471.

[61] J. Zhou, Z. Liu, F. Li, *Chem. Soc. Rev.* **2012**, *41*, 1323.

[62] J. Rocha, L. D. Carlos, F. A. A. Paz, D. Ananias, *Chem. Soc. Rev.* **2011**, *40*, 926.

[63] D. Wang, L. Wang, X. Dong, Z. Shi, J. Jin, *Carbon* **2012**, *50*, 2147.

[64] L. D. Carlos, R. A. S. Ferreira, V. De Zea Bermudez, S. J. L. Ribeiro, *Adv. Mater.* **2009**, *21*, 509.

[65] I. L. Medintz, A. R. Clapp, H. Mattoussi, E. R. Goldman, B. Fisher, J. M. Mauro, *Nat. Mater.* **2003**, *2*, 630.

[66] S. Zhuo, M. Shao, S.-T. Lee, *ACS Nano* **2012**, *6*, 1059.

[67] D. Qu, M. Zheng, P. Du, Y. Zhou, L. Zhang, D. Li, H. Tan, Z. Zhao, Z. Xie, Z. Sun, *Nanoscale* **2013**, *5*, 12272.

[68] R. Long, *ChemPhysChem* **2013**, *14*, 579.

[69] A. Facchetti, *Chem. Mater.* **2011**, *23*, 733.

[70] M. Grätzel, *Acc. Chem. Res.* **2009**, *42*, 1788.

[71] C. J. Brabec, S. Gowrisanker, J. J. M. Halls, D. Laird, S. Jia, S. P. Williams, *Adv. Mater.* **2010**, *22*, 3839.

[72] S. S. Li, K. H. Tu, C. C. Lin, C. W. Chen, M. Chhowalla, *ACS Nano*

2010, *4*, 3169.

[73] R. Steim, F. R. Kogler, C. J. Brabec, *J. Mater. Chem.* **2010**, *20*, 2499.

[74] R. Leary, A. Westwood, *Carbon* **2011**, *49*, 741.

[75] L. Dai, D. W. Chang, J. B. Baek, W. Lu, *Small* **2012**, *8*, 1130.

[76] S. Guo, S. Dong, *Chem. Soc. Rev.* **2011**, *40*, 2644.

[77] Y. Dong, J. Shao, C. Chen, H. Li, R. Wang, Y. Chi, X. Lin, G. Chen, *Carbon* **2012**, *50*, 4738.

[78] Y. Dai, H. Long, X. Wang, Y. Wang, Q. Gu, W. Jiang, C. Li, T. H. Zeng, Y. Sun, J. Zeng, *Part. Part. Syst. Char.* **2013**.

[79] J. Y. Hong, J. Jang, *Soft Matter* **2012**, *8*, 7348.

[80] H. Cölfen, *Polymer News* **2004**, *29*, 101.

[81] Y. Watanabe, A. Kawamoto, K. Matsuda, *Compos. Sci. Technol.* **2002**, *62*, 881.

[82] H. W. Liang, W. J. Zhang, Y. N. Ma, X. Cao, Q. F. Guan, W. P. Xu, S. H. Yu, *ACS Nano* **2011**, *5*, 8148.

[83] K. Matsui, L. J. Lanticse, Y. Tanabe, E. Yasuda, M. Endo, *Carbon* **2005**, *43*, 1577.

[84] J. Huang, D. Wang, H. Hou, T. You, *Adv. Funct. Mater.* **2008**, *18*, 441.

[85] P. Li, T. J. Zhao, J. H. Zhou, Z. J. Sui, Y. C. Dai, W. K. Yuan, *Carbon* **2005**, *43*, 2701.

[86] A. C. Ferrari, J. C. Meyer, V. Scardaci, C. Casiraghi, M. Lazzeri, F. Mauri, S. Piscanec, D. Jiang, K. S. Novoselov, S. Roth, A. K. Geim, *Phys. Rev. Lett.* **2006**, *97*.

[87] Y. Dong, H. Pang, H. B. Yang, C. Guo, J. Shao, Y. Chi, C. M. Li, T. Yu, *Angew. Chem., Int. Ed.* **2013**, *52*, 7800.

[88] C. Lee, X. Wei, J. W. Kysar, J. Hone, *Science* **2008**, *321*, 385.

[89] A. K. Geim, *Science* **2009**, *324*, 1530.

[90] D. C. Coffey, A. J. Ferguson, N. Kopidakis, G. Rumbles, *ACS Nano* **2010**, *4*, 5437.

[91] E. Lee, C. Kim, J. Jang, *Chem. Eur. J.* **2013**, *19*, 10280.

[92] S. Buhbut, S. Itzhakov, E. Tauber, M. Shalom, I. Hod, T. Geiger, Y. Garini, D. Oron, A. Zaban, *ACS Nano* **2010**, *4*, 1293.

[93] C. Yuan, G. Chen, P. N. Prasad, T. Y. Ohulchanskyy, Z. Ning, H. Tian, L. Sun, H. Agren, *J. Mater. Chem.* **2012**, *22*, 16709.

[94] G. B. Shan, G. P. Demopoulos, *Adv. Mater.* **2010**, *22*, 4373.

[95] J. Wu, J. Wang, J. Lin, Z. Lan, Q. Tang, M. Huang, Y. Huang, L. Fan, Q. Li, Z. Tang, *Advanced Energy Materials* **2012**, *2*, 78.

[96] J. Shen, Y. Zhu, X. Yang, J. Zong, J. Zhang, C. Li, *New J. Chem.* **2012**, *36*, 97.

[97] J. H. Yum, B. E. Hardin, S. J. Moon, E. Baranoff, F. Nüesch, M. D.

McGehee, M. Grätzel, M. K. Nazeeruddin, *Angew. Chem., Int. Ed.* **2009**, *48*, 9277.

[98] G. K. Mor, J. Basham, M. Paulose, S. Kim, O. K. Varghese, A. Vaish, S. Yoriya, C. A. Grimes, *Nano Lett.* **2010**, *10*, 2387.

[99] J. H. Yum, B. E. Hardin, E. T. Hoke, E. Baranoff, S. M. Zakeeruddin, M. K. Nazeeruddin, T. Torres, M. D. McGehee, M. Grätzel, *ChemPhysChem* **2011**, *12*, 657.

[100] J. I. Basham, G. K. Mor, C. A. Grimes, *ACS Nano* **2010**, *4*, 1253.

[101] G. Wang, Q. Peng, Y. Li, *Acc. Chem. Res.* **2011**, *44*, 322.

[102] R. F. Fink, J. Pfister, H. M. Zhao, B. Engels, *Chem. Phys.* **2008**, *346*, 275.

[103] C. Siegers, J. Hohl-Ebinger, B. Zimmermann, U. Würfel, R. Mülhaupt, A. Hinsch, R. Haag, *ChemPhysChem* **2007**, *8*, 1548.

[104] K. Ai, B. Zhang, L. Lu, *Angew. Chem., Int. Ed.* **2009**, *48*, 304.

[105] W. K. Oh, Y. S. Jeong, J. Song, J. Jang, *Biosens. Bioelectron.* **2011**, *29*, 172.

[106] S. J. Park, O. S. Kwon, S. H. Lee, H. S. Song, T. H. Park, J. Jang, *Nano Lett.* **2012**, *12*, 5082.

[107] J. P. Kirby, M. L. Cable, D. J. Levine, H. B. Gray, A. Ponce, *Anal. Chem.* **2008**, *80*, 5750.

[108] M. D. Yilmaz, S.-H. Hsu, D. N. Reinhoudt, A. H. Velders, J. Huskens, *Angew. Chem. Int. Ed.* **2010**, *49*, 5938.

[109] I. Lee, W. K. Oh, J. Jang, *J. Hazard. Mater.* **2013**, *252-253*, 186.

[110] B. Farrow, S. A. Hong, E. C. Romero, B. Lai, M. B. Coppock, K. M. Deyle, A. S. Finch, D. N. Stratis-Cullum, H. D. Agnew, S. Yang, J. R. Heath, *ACS Nano* **2013**, *7*, 9452.

[111] M. L. Cable, J. P. Kirby, K. Sorasaenee, H. B. Gray, A. Ponce, *J. Am. Chem. Soc.* **2007**, *129*, 1474.

[112] C. Kim, S. Kim, W. K. Oh, M. Choi, J. Jang, *Chem. Eur. J.* **2012**, *18*, 4902.

[113] Z. Guo, I. Shin, J. Yoon, *Chem. Commun.* **2012**, *48*, 5956.

[114] W.-K. Oh, Y. S. Jeong, S. Kim, J. Jang, *ACS Nano* **2012**, *6*, 8516.

[115] Q. He, H. G. Sudibya, Z. Yin, S. Wu, H. Li, F. Boey, W. Huang, P. Chen, H. Zhang, *ACS Nano* **2010**, *4*, 3201.

[116] S. Zhu, J. Zhang, S. Tang, C. Qiao, L. Wang, H. Wang, X. Liu, B. Li, Y. Li, W. Yu, X. Wang, H. Sun, B. Yang, *Adv. Funct. Mater.* **2012**, *22*, 4732.

[117] K. J. Lee, W.-K. Oh, J. Song, S. Kim, J. Lee, J. Jang, *Chem. Commun.* **2010**, *46*, 5229.

[118] T. Gunnlaugsson, M. Glynn, G. M. Tocci, P. E. Kruger, F. M. Pfeffer,

Coord. Chem. Rev. **2006**, *250*, 3094.

[119] V. Tharmaraj, K. Pitchumani, *RSC Advances* **2013**, *3*, 11566.

[120] A. Sikora, J. Zielonka, M. Lopez, J. Joseph, B. Kalyanaraman, *Free Radical Biology and Medicine* **2009**, *47*, 1401.

[121] Y. Tao, Y. Lin, Z. Huang, J. Ren, X. Qu, *Adv. Mater.* **2013**, *25*, 2594.

국문초록

지난 수년 동안 집중적인 연구적 관심을 불러 일으키고 있는 그래핀양자점은 측면지름이 약 100 nm 이하이고, 단일-, 이중-, 몇 층의(3 내지 10 개의) 층으로 이루어진 그래핀 시트이다. 그래핀양자점은 밴드갭의 존재, 넓은 표면적, 용이한 표면결합, 다양한 표면기와 같은 고유의 특성뿐만 아니라, 우수한 형광 특성 및 업컨벌젼 형광성질과 같은 광학적 특성을 바탕으로 광전자공학, 형광센서, 바이오 응용, 촉매반응, 에너지 저장 및 변환 등의 다양한 분야에 적용되고 있다.

본 연구에서는 하향식/상향식 접근방법을 이용하여 크기와 형광특성이 조절된 그래핀양자점을 제조하였으며, 이들의 형성 메커니즘을 체계적으로 고찰하였고, 아울러 광전변환소자, 형광 센서, 바이오 이미징으로의 응용에 대해 살펴보았다. 하향식 접근방법으로, 그래핀양자점은 탄소나노물질의 산화방법과 크기선택적 분리방법을 이용해 제조할 수 있었다. 흥미롭게도, 그래핀양자점의 지름과 형광파장은 시작물질의 형태 디자인과 산화조건의 최적화를 통하여 조절할 수 있었다. 뿐만 아니라, 그래핀 양자점의 균일한 발광특성을 활용하기 위해서, 크기선택적 침전방법을 이용한 분리방법을 제한하였다. 그래핀 양자점을 크기선택적 침전방법을 통해서 추가적인 특석방법 없이 성공적으로 균일한 크기의 그래핀 양자점을 얻을 수 있었다. 상향식 접근방법으로, 여러 도핑물질과 함께 유기전구체의 탄화공정을 이용하여 헤테로원자가 도핑된 그래핀양자점을 제조할 수 있었다. 황산의

촉매조건에서 시트르산은 탈수공정을 통하여 흑연의 정육면체 구조를 형성하며 그래핀 양자점으로 변하였다. 또한 황산과 디메틸포름아미드가 각각 황과 질산 도핑 물질로서 사용되어, 탄화정도가 조절되고, 그람 스케일의, 그리고 높은 형광양자효율(약 61%)을 가진 황과 질소가 도핑된 그래핀양자점을 제조하였다. 본 연구에서 새롭게 개발한 하향식/상향식 접근방법은 제어된 크기 및 모양을 지닌 다양한 종류의 그래핀양자점 제조에 적용될 수 있으며, 이를 통해 전자/광전자 장치, 형광프로브, 바이오이미징, 에너지변환장치를 포함한 여러가지 응용분야에 폭넓게 활용될 수 있을 것으로 사료된다.

주요어: 탄소나노물질, 그래핀양자점, 제조방법, 하향식, 상향식, 염료감응태양전지, 형광센서, 바이오 이미징

학번: 2009-23955